Quantitative Assessments of Various Plastic Flow Mechanisms by In Situ Neutron Diffractions for Advanced High Entropy Alloys

A Dissertation Presented for the

Doctor of Philosophy

Degree

The University of Tennessee, Knoxville

Lia Amalia

August 2026

Copyright © 2026 by Lia Amalia

All rights reserved.

DEDICATION

To my mother, father, and my fearless leader of a sister, I would not have the tenacity and resourcefulness to go on to a whole foreign country by myself to get this experience.

ACKNOWLEDGEMENTS

I would like to thank my graduate advisors, Prof. Peter K. Liaw and Prof. Yanfei Gao who took a chance on me in the middle of a pandemic and offered me insurmountable support during my graduate studies. I would like to thank Dr. Ke An for his mentorship and alleviating my anxiety during the last two years of my graduate studies. I would like to thank Prof. Eric A. Lass for his guidance and presenting refractory high entropy alloys into my consciousness. I would also like to thank Dr. Ying Yang the chance to keep working together. Special thanks to my incredible lab mates, Dr. Zongyang Lyu and Dr. Xuesong Fan who taught me many intricate things in the lab, and Nathan Grain who is always ready to help me and bounce ideas with. I really appreciate the help of everyone in VULCAN beamline, Dr. Dunji Yu and Dr. Yan Chen for teaching me how to analyze the data. I thank everyone who has helped me throughout this journey.

ABSTRACT

Understanding the deformation behavior of high-entropy alloys (HEAs) is critical for advancing their application in structural environments, especially where strength, ductility, and thermal stability are required. Previous work on HEAs system has successfully uncovered some alloy systems that break the strength-ductility tradeoffs. However, many of the studies were done in postmortem, missing the real-time strengthening mechanism. Moreover, quantification of hardening contribution of constituents involved during real-time deformation is still lacking. This unique work applies a unified experimental approach using in situ neutron diffraction to investigate lattice strain, peak intensity, and peak broadening evolution under mechanical loading across three distinct alloy systems. Beyond the existing advanced quantitative analyses based on in situ neutron diffraction study such as stacking fault energy calculation, dislocation density calculation, and dislocation character analyses, this work provides novel mechanistic-based method to quantify hardening contributions of each constituent in the alloy system in real time. The three different systems of interest include nanoprecipitate-strengthened (FeCoNi)86Al7Ti7 HEA to examine and quantify the hardening contribution of the secondary phase, CoCrFeNi-based alloys with Cu additions to study solute effects on mechanical behavior in real time within the same alloy system, and refractory HfTiZrNbTa systems to explore slip systems contribution to strength and ductility and study the tension-compression asymmetry. By integrating these insights with electron microscopy and atom probe tomography, this work aims to develop a mechanistic,

multiscale understanding of plasticity in complex alloys and contribute to the design of next-generation high-performance materials.

TABLE OF CONTENTS

CHAPTER I 1

INTRODUCTION 1

Motivation 1

Objectives 1

Framework 2

Literature Review 3

High Entropy Alloys *3*

Deformation behavior of face-centered cubic (FCC) HEAs 4

Deformation behavior of body-centered cubic (BCC) HEAs 7

Precipitation strengthening in FeCoNi-HEAs 10

Effect of alloying element on CoCrFeNi-HEAs 12

Compositional effect on HfNbTaTiZr 14

References 18

CHAPTER II Copper effects on the microstructures and deformation mechanisms of cocrfeni high entropy alloys 28

Abstract 30

Introduction 30

Methods 33

Results and Discussion 38

Conclusion 48

References 50

CHAPTER III Tangent moduli and successive hardening mechanisms: quantification from in situ neutron diffraction and ductility improvement of nanoprecipitation-strengthened HEAs 55
Abstract 57
Introduction 58
Experimental Procedures 61
Experimental Results 63
The Mechanics Model for Tangent Moduli 71
Discussions 77
Conclusions 89
References 90
CHAPTER IV Tension-compression asymmetry in Hf-Ti-Zr-Nb-Ta refractory high entropy alloys studied with in situ neutron diffraction 98
Abstract 100
Introduction 100
Methods 104
Calphad calculation and sample fabrication 104
Mechanical test and neutron diffraction measurement 105
Dislocation density calculations 105
Local strain resistance 107
Non-Schmid effect calculation 108
Experimental Results 109

Compositional selection using BCC/HCP stability descriptor 109

Macroscopic mechanical response and diffraction derived elastic constants 113

Lattice strain evolution 118

Discussion 120

Non-Schmid effect 120

Defect evolution 125

Conclusions 134

References 136

Chapter V 145

SUMMARY AND FUTURE SUGGESTIONS 145

Summary 145

Future Suggestions 145

VITA 146

LIST OF TABLES

Table 1. Calculated elastic constants..... 42

Table 2. Calculated elastic moduli with respect to specific grain orientations. 42

Table 3. Slopes of the linear regression from the modified Williamson-Hall plot and dislocation densities of CoCrFeNi-1Cu and CoCrFeNi-3Cu at several strain levels, obtained from the modified Williamson-Hall peak broadening analysis. 47

Table 4. Calculated stiffness and compliance constants for the two phases. 78

Table 5. Elastic constants, derived elastic properties, and mechanical properties. (Elastic constants, $C11$, $C11$, $C11$; Zener anisotropy constant, A; bulk modulus, B; Tetragonal shear moduli G'; Hull shear modulus, GH; Poisson's ratio, v; Pugh's ratio, P)..... 117

Table 6. Summary of phase stability, deformation features, and tension–compression asymmetry in Hf–Nb–Ta–Ti–Zr RHEAs..... 132

LIST OF FIGURES

Figure 1 High entropy alloying concept. [3] 5

Figure 2 Schematic illustration of (from left to right) body-centered cubic, face-centered cubic, and hexagonal close-packed crystalline structures composed of multi-principal elements. [5] 5

Figure 3 Comparison of the temperature dependence of yield strengths. Yield strengths of the NbTaTiV alloy and two reported refractory HEAs (MoNbTaW and MoNbTaVW), conventional HEA (Al2.0CoCrCuFeNi), Al-based alloy (6061 Al alloy), Ti-based alloy (Ti-6Al-4V alloy), and Ni-based superalloys (Inconel 718 and Haynes 230) as a function of temperature [62-64]. [6]. 6

Figure 4 Simulated (a) local slip resistance for screw and edge dislocations on {110}, {112}, and {123} planes in MoNbTi. The schematic of simulated dislocation moving on a plane is illustrated in (b), where the thick blue line was moved to create shear in either direction to assess the slip sense asymmetry. The cumulative distribution of local slip resistance is shown in (c), with the experimentally determined resolved shear stress on the active slip system 1⁄2 [1-11](-213) is shown in thick yellow horizontal line. [23] 9

Figure 5 (a) Types of nanoprecipitates and their contribution to strength and (b) the **f**requency of elements used in nanoprecipitation-strengthened HEAs. [33] 11

Figure 6 (a) Work-hardening rate and (b) work hardening exponent of $(FeCoNi)_{86}Al_7Ti_7$ and $(FeCoNi)_{86}Al_8Ti_6$. (c) evolution of deformation substructures of

$(FeCoNi)_{86}Al_7Ti_7$ with increasing tensile loading, taken with transmission electron microscope. 13

Figure 7 Simulated dislocation density as a function of indentation depth. (a) total dislocation; (b) Hirth dislocation; (c) stair-rod dislocation; (d) Shockley partial dislocation [55] 15

Figure 8. Scanning electron microscope (SEM) images of the (a) CoCrFeNi-1Cu, (b) CoCrFeNi-3Cu, and (c) CoCrFeNi-5Cu microstructures showing similar grain sizes (around 70μm) and EDS element map images of (d) CoCrFeNi-1Cu showing smaller sized clusterings of Cu, and (e) of CoCrFeNi-5Cu showing larger sized Cu clusters. 34

Figure 9. (a) Schematic drawing of the experimental setup at Vulcan beamline, SNS, ORNL. (b) True stress versus true strain overlapping with the work hardening rate ($d\sigma/d\varepsilon$) of CoCrFeNi-1Cu, CoCrFeNi-3Cu, and CoCrFeNi-5Cu, showing three different regions of deformation behavior. 36

Figure 10. The measured diffraction patterns upon tensile loading, collected at bank 1 (corresponding to loading direction) for (a) CoCrFeNi-1Cu and (b) CoCrFeNi-3Cu. The evolution of lattice strains in loading (bank 1) and transversal direction (bank 2) of (c) CoCrFeNi-1Cu and (d) CoCrFeNi-3Cu. (e) showed the lattice strain difference between {111} and {222} in CoCrFeNi-1Cu and CoCrFeNi-3Cu, indicating stacking fault formation. Higher (f) work hardening rate and (g) stacking fault probability, with lower (h) stacking fault interspacing and (i) stacking fault energy of CoCrFeNi-1Cu starting from 25% of strain as compared to CoCrFeNi-3Cu. 40

Figure 11. (a) Dislocation density of CoCrFeNi-1Cu and CoCrFeNi-3Cu, with TEM images of (b) CoCrFeNi-1Cu showing twinnings and (c) CoCrFeNi-5Cu showing dislocation forests. Both images were taken near the end of the stress-strain curves in Figure 9. 46

Figure 12. Microstructural characterization of the undeformed Al_7Ti_7-this-work by (a) neutron diffraction and (b) bright-field transmission electron microscopy (TEM) along the {001} zone axis. Note that the FCC peaks overlap with the $L1_2$ peaks in (a). 64

Figure 13. Atom Probe Tomography (APT) reconstruction of needle samples, showing the isoconcentration surface of the samples taken from (a) undeformed state and (b) deformed state (after the tensile fracture). (c) The proxigrams show clear distinction between the FCC matrix and the $L1_2$ precipitates. 66

Figure 14. (a) Engineering stress-strain curves of three materials, including Al7Ti7-this-work obtained from ex situ tensile test, Al8Ti6-Yang, and Al7Ti7-Yang (the latter two obtained from [15]), and (b) the work hardening behavior of the Al7Ti7-this-work under uniaxial tension. 68

Figure 15. (a) Lattice strain evolutions of different grain families in Al_7Ti_7-this-work along loading direction. (b) and (c) Representative TEM images of the undeformed and fractured Al_7Ti_7-this-work. 70

Figure 16. Schematic illustration of how the yielding sequence governs the lattice strain splitting. (a) The stress-strain curves showing the initial yield takes place for the material with low yield strain. (b) The Taylor iso-strain composite model. (c) The

corresponding stress vs. elastic strain curves for the two constituents. (d) The corresponding evolution of material tangent. 72

Figure 17. Schematic illustration of how different hardening rates govern the lattice strain splitting. (a) The stress-strain curves of each material and the composite. (b) The Taylor iso-strain composite model. (c) The corresponding stress vs. elastic strain curves for the two constituents. (d) The corresponding evolution of material tangent. 74

Figure 18. Illustration of data processing from (a) true stress versus true strain and (b) true stress versus lattice strain to obtain the tangent modulus. 76

Figure 19. Tangent modulus evolution of three representative grain families of FCC phase and three representative grain families of $L1_2$ phase. The table below shows the schematic trends in the three deformation stages. 78

Figure 20. (a) Phase strain evolution of FCC and $L1_2$ phase versus true stress; (b) phase stresses of FCC and $L1_2$ phase with the calculated average stress compared to the measured bulk stress tested in situ during neutron diffraction data acquisition. 80

Figure 21. Evolution of normalized intensity of FCC phase in (a) loading direction and (c) transversal direction, and $L1_2$ precipitates in (b) loading direction and (d) transversal direction. 82

Figure 22. Evolution of normalized peak width divided with d-spacing of FCC phase in (e) loading direction and (g) transversal direction, and $L1_2$ precipitates in (f) loading direction and (h) transversal direction. 83

Figure 23. The evolution of deformation mechanisms in the three stages, including the initial elastic-plastic Stage I, the more pronounced hardening-rate in $L1_2$ than FCC phases in Stage II, and comparable dislocation densities in both phases in Stage III. As a comparison, the last stage in Yang et al. [15] has multiple micro-bands that extend over several precipitates, which are not seen in this work 87

Figure 24. Experimental setup at VULCAN beamline, Spallation Neutron Source, Oak Ridge National Laboratory, illustrating mechanical test in (a) tension and in (b) compression. 106

Figure 25. (a) Gibbs free energy of transformation from BCC to HCP versus tensile elongation, indicating compositions with transformation induced plasticity (TRIP) effect [12, 21, 30], ductile [11, 13, 32, 35], and brittle [10] during tensile loading. (b) Bond order (Bo) versus d-orbital energy (Md) level [33, 34]. (c) Yield strength versus tensile elongation. 112

Figure 26. True stress versus true strain, overlapping with the corresponding work hardening rate, of (a) in situ tension tests, (b) in situ compression tests, and (c) ex situ compression tests. (d) True stress versus strain curves of in situ tension tests overlayed with in situ compression tests. 114

Figure 27. Lattice strain versus true strain of $HfNb_{0.5}Ta_{0.5}TiZr$, $HfNbTa_{0.5}TiZr$, and $Hf_{0.5}NbTa_{0.5}TiZr$ from in situ tension and compression neutron diffraction measurements. The negative values from the compression tests have been converted into positive values. 119

Figure 28. (a-c) Calculated Schmid effect and (d-f) calculated non-Schmid effect evaluation on the (g-i) hkl-specific yield strain sequence during compression loading for $HfNb_{0.5}Ta_{0.5}TiZr$, $HfNbTa_{0.5}TiZr$, and $Hf_{0.5}NbTa_{0.5}TiZr$. 121

Figure 29. (a-c) Calculated Schmid effect and (d-f) calculated non-Schmid effect evaluation on the (g-i) hkl-specific yield strain sequence during tension loading for $HfNb_{0.5}Ta_{0.5}TiZr$, $HfNbTa_{0.5}TiZr$, and $Hf_{0.5}NbTa_{0.5}TiZr$. 122

Figure 30. Diffraction patterns evolution of $HfNb_{0.5}Ta_{0.5}TiZr$, $HfNbTa_{0.5}TiZr$, and $Hf_{0.5}NbTa_{0.5}TiZr$ during tension and compression load, obtained from loading direction. 126

Figure 31. Normalized FWHM/d of $HfNb_{0.5}Ta_{0.5}TiZr$, $HfNbTa_{0.5}TiZr$, and $Hf_{0.5}NbTa_{0.5}TiZr$ during tensile loading 127

Figure 32. Normalized FWHM/d of $HfNb_{0.5}Ta_{0.5}TiZr$, $HfNbTa_{0.5}TiZr$, and $Hf_{0.5}NbTa_{0.5}TiZr$ during compression loading..... 128

Figure 33. Dislocation density evolution of Edge$\langle 111\rangle\{110\}$-, Edge$\langle 111\rangle\{211\}$-, and Screw $\langle 111\rangle$-type dislocations during in situ tension and compression measurements of $HfNb_{0.5}Ta_{0.5}TiZr$, $HfNbTa_{0.5}TiZr$, and $Hf_{0.5}NbTa_{0.5}TiZr$ extracted from B1, B2, and B4 and calculated using Modified Williamson-Hall model. 129

Figure 34. Modified Williamson-Hall plot's goodness of fit..... 131

CHAPTER I

INTRODUCTION

Motivation

High-entropy alloys (HEAs) have been reported to show impressive mechanical properties. However, the underlying mechanism of how they deform, especially how dislocations, twinning, and hardening evolve during loading are still not well understood. Moreover, the strength-ductility trade-off is still a challenge yet to be solved. Previous work on the deformation behavior of HEAs utilizes the post-mortem study on highly localized region of the material, such as using scanning electron microscope (SEM) and transmission electron microscope (TEM), missing the bulk information and also missing the process the material underwent to reach the final deformation stage. There are three tasks in this study, exploring different alloy systems. However, the underlying motivation of studying different systems is to use in situ neutron diffraction to track and quantify how materials respond under stress in real time. This technique gives us access to lattice strain, intensity, and peak broadening evolution as deformation happens, allowing us to investigate the evolution of deformation behavior at the grain level. By building around this shared method, the project aims to deepen our understanding of deformation across a range of HEAs, even when the systems themselves are quite different.

Objectives

This proposed work aims to understand and quantify deformation behavior in various high-entropy alloy systems using in situ neutron diffraction, supported by atomic-scale composition mapping and ex-situ microscopy. Although the systems differ across

tasks, each objective leverages lattice strain and peak broadening analysis to uncover mechanisms governing strength and ductility.

- Task 1: Quantify tangent moduli, hardening behavior, and ductility in nanoprecipitation-strengthened (FeCoNi)86Al7Ti7 by analyzing lattice strain evolution and dislocation activity during uniaxial loading.
- Task 2: Investigate how copper additions influence microstructure and defect evolution in CoCrFeNi alloys, using in situ diffraction to track changes in peak broadening and strain partitioning to reveal deformation behavior.
- Task 3: Use in situ neutron diffraction to examine the plasticity and ductility mechanisms of HfTiZrNbTa alloys, with a focus on identifying active slip systems across different loading paths.

Insights from these experiments will inform micromechanical models and help establish structure–property relationships across compositionally complex alloys.

Framework

There are three tasks that are proposed to utilize in situ neutron diffraction in three different systems. The first task is to demonstrate the successive yielding and hardening sequence of different grain orientations from different phases, extracted from in situ neutron diffraction experiment, using (FeCoNi)86Al7Ti7 system as the example. The second task is to demonstrate the deformation mechanism changes using in situ neutron diffraction experiment, in CoCrFeNi system, by tweaking the alloying element composition. The third task is to utilize in situ neutron diffraction to study the ductility and plasticity of novel refractory high entropy alloys by extracting the dislocation types and

the dislocation density. Both tension and compression tests were conducted for the novel refractory high entropy alloys to study the ductility and plasticity for the third task. The lattice strain and peak broadening evolution from the in situ neutron diffraction experiments were analyzed using single peak method and full profile (Rietveld) method to discern if the material deforms by phase transformation, twinning formation, or dislocation formation. Atomic-scale composition mapping using atom probe tomography was also conducted to resolve the atomic composition of the precipitates in (FeCoNi)86Al7Ti7 system. Ex-situ characterizations such as scanning electron microscopy (SEM) and transmission electron microscopy (TEM) were also conducted to support the findings from in situ neutron diffraction analyses.

Literature Review

High Entropy Alloys

The high entropy alloy concept was independently uncovered by Yeh [1] and Cantor [2] in 2004, and has since expanded the conventional alloy design space, as shown in Figure 1 [3]. High entropy alloys represent a new class of alloys that is consisted of five or more principal elements with each elements having 5% to 35% of mole fraction [4]. The high configurational entropy promotes the simple solid solution phase formation, as illustrated in Figure 2 [5] instead of intermetallic compounds despite the complex alloy system. High entropy alloys possess distinct characteristics compared to conventional alloys such as the high entropy effect, high lattice distortion due to atomic size mismatch, sluggish diffusion, and cocktail effect where the synergistic interactions produce unique properties which are different from the properties of the elements alone. These distinct properties lead to high

tunability of high entropy alloys, making HEAs possess unique features and properties such as chemical short-range ordering (CSRO), twinning-induced plasticity (TWIP), transformation-induced plasticity (TRIP), strong and dense precipitates, and compositional waves.

Another subset of HEAs are the refractory HEAs (RHEAs), which are primarily composed of refractory elements such as Hf, Nb, Ta, Ti, Zr, and Mo. RHEAs have been studied to possess excellent high-temperature strength as shown in Figure 3 [6], making them strong candidates for elevated-temperature applications such as in aerospace and power generation. However, the hinderance to apply RHEAs comes from its brittleness at room temperature and tension-compression asymmetry.

Due to these unique features and properties, HEAs are promising alloy systems for many applications such as load-bearing applications, cryogenic applications [7], high-temperature applications [8], and corrosive environments [9]. The unique behavior of HEAs have been reviewed and compared as shown in Figures 1 to 3 presenting the comparison of strength versus ductility of HEAs with low stacking fault energy, the role of precipitation strengthening, and the comparison of Refractory HEAs high-temperature yield strength, respectively.

Deformation behavior of face-centered cubic (FCC) HEAs

Face-centered cubic (FCC) high entropy alloys such as the well-known system, CoCrFeMnNi, and its derivatives possess excellent ductility and work hardening rates due to the close-packed structure and tunable stacking fault energy [10]. The plastic deformation in FCC HEAs is primarily governed by edge dislocation which moves more

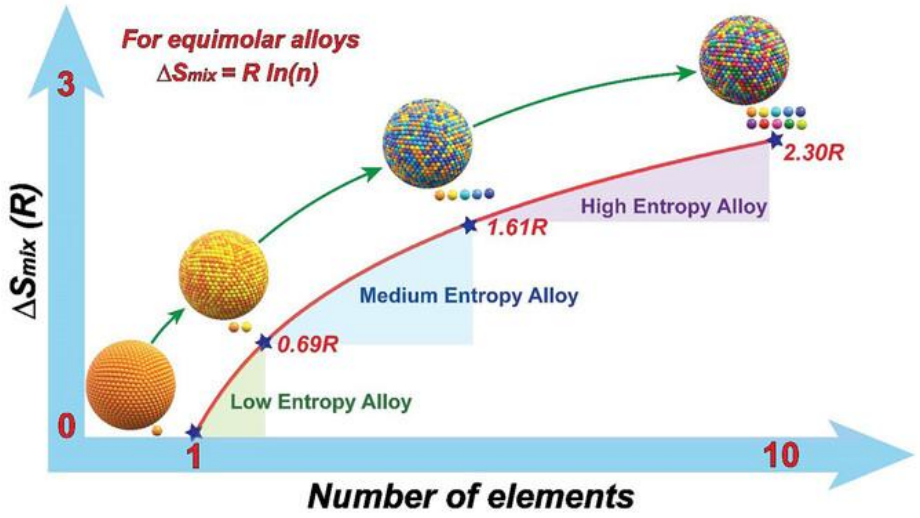


Figure 1 High entropy alloying concept. [3]

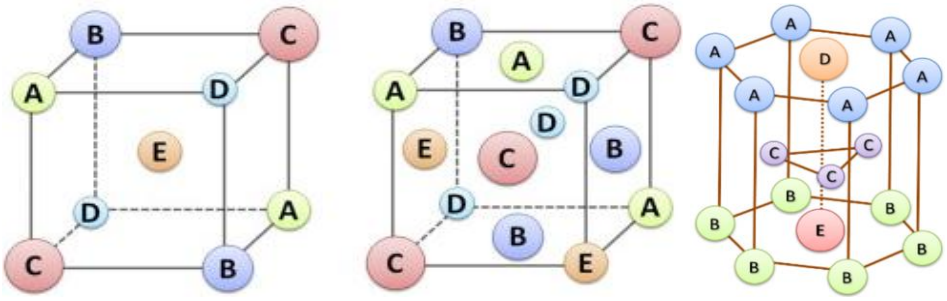


Figure 2 Schematic illustration of (from left to right) body-centered cubic, face-centered cubic, and hexagonal close-packed crystalline structures composed of multi-principal elements. [5]

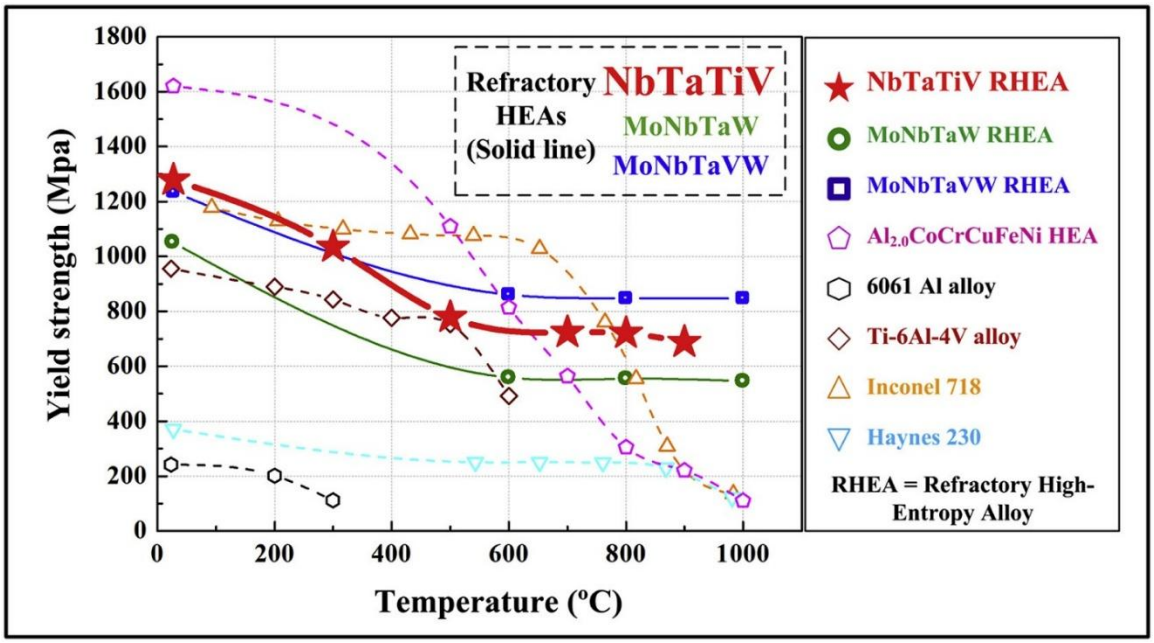


Figure 3 Comparison of the temperature dependence of yield strengths. Yield strengths of the NbTaTiV alloy and two reported refractory HEAs (MoNbTaW and MoNbTaVW), conventional HEA (Al2.0CoCrCuFeNi), Al-based alloy (6061 Al alloy), Ti-based alloy (Ti-6Al-4V alloy), and Ni-based superalloys (Inconel 718 and Haynes 230) as a function of temperature [62-64]. [6].

easily along the {111} slip planes [11]. In the deformation behavior study of CoCrFeMnNi, the early stages of dislocation were dominated by planar dislocation glide on 1⁄2 ⟨110⟩{111}. Stacking faults were also observed which suggest the dislocations split into partial dislocations of 1⁄6 ⟨112⟩. After some level of strain, depending on the testing temperature [11, 12], twinning occurs which provides the dynamic Hall-Petch effect [11], delaying necking based on Considère criterion [13]. For some compositions with stacking fault energy between 20 to 45 mJ/m2 or at a cryogenic temperature, twinning may occur. Meanwhile, for other FCC HEAs having stacking fault energy of less than 20 mJ/m2, phase transformation may occur [14, 15]. The interplay of these deformation modes is how some FCC HEAs possess the strength-ductility synergy to delay necking [11].

Deformation behavior of body-centered cubic (BCC) HEAs

Body-centered cubic (BCC) HEAs, particularly the RHEAs such as the well-known HfNbTaTiZr system exhibit an outstanding high-temperature strength [16, 17], however they tend to be brittle in room temperature [18] and asymmetry in tension and compression [19]. Asymmetry in tension and compression in body-centered cubic (BCC) metals and alloys is a complex mechanical phenomenon, especially at room temperature where the dislocation mobility is sensitive to the direction of applied stress [20]. In BCC systems, plasticity is predominantly controlled by thermally activated motion of 1⁄2 ⟨111⟩ screw dislocations with non-planar cores. The 1⁄2 ⟨111⟩ screw dislocations with non-planar cores experience high lattice friction even at ambient temperatures. The high lattice friction leads to a strong deviation from Schmid's law and the direction-dependent yielding and plastic flow, which collectively result in tension-compression asymmetry [20].

At room temperature, screw dislocations in BCC systems are sluggish or move with difficulty and require stress states that promote kink-pair formation. Furthermore, the dislocation motion is complicated by non-Schmid effects where mobility of dislocation depends on shear stresses not aligned with the glide plane. This means that under tensile loading certain dislocation core configurations are less stable compared to when the system is loaded in compression, leading to asymmetric activation of slip systems [21]. Simulations on dislocation dynamics that is informed by atomistic calculations reveal that even subtle variations in the resolved shear stress and non-glide stress can alter the activation of slip system and critical resolved shear stress, amplifying the tension-compression asymmetry [22]. Simulation study on MoNbTi calculating the local slip resistance (LSR) for edge and screw dislocations on {110}, {112}, and {123} planes revealed the probabilistic nature of the dislocation glide in this complex alloy system [23]. Figure 4 (a) shows variations in LSR, depending on the local atomic configurations, the lowest stress to move a dislocation can occur on either {110}, {112}, or {123} plane. Especially for {112} plane, the dislocation slip asymmetry due to either twinning or anti-twinning asymmetry is also probabilistic in nature. Figure 4 (c) shows the cumulative distribution of LSR values, showing that in MoNbTi, the gliding on {123} planes is the easiest, which agrees with the experimental observation where 1⁄2 [1-11](-213) is the active slip system at yield. In situ neutron diffraction experiments have provided direct evidence of deformation behavior of BCC RHEAs. Lee et al. [24] demonstrated that the strength of NbTaTiV and CrMoNbV RHEAs could be controlled by edge dislocation, revealed through in situ neutron diffraction study. Another study on tensile loaded (TiZrHfNb)98N2

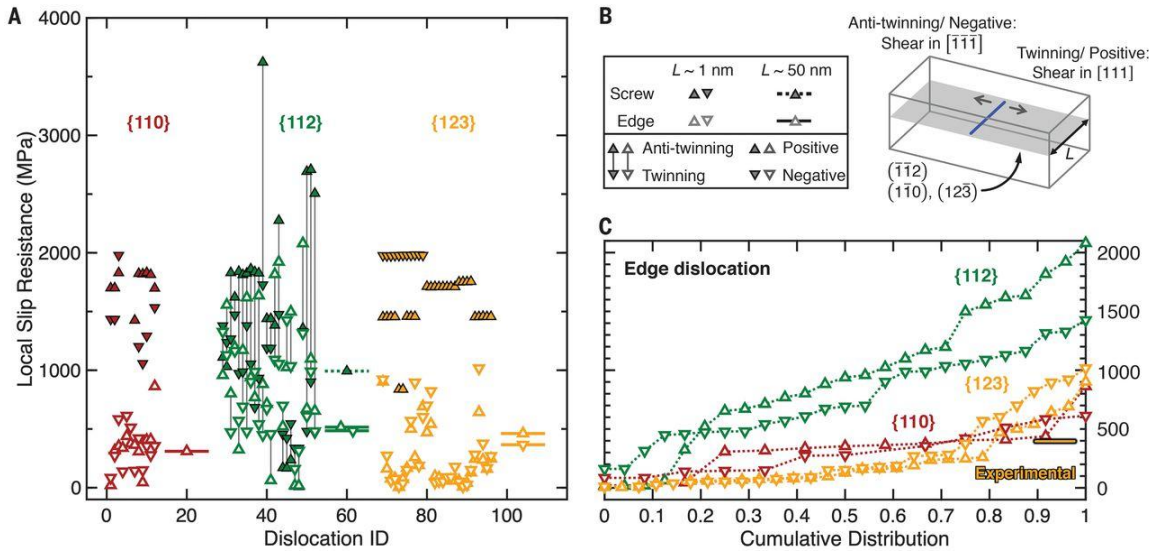


Figure 4 Simulated (a) local slip resistance for screw and edge dislocations on {110}, {112}, and {123} planes in MoNbTi. The schematic of simulated dislocation moving on a plane is illustrated in (b), where the thick blue line was moved to create shear in either direction to assess the slip sense asymmetry. The cumulative distribution of local slip resistance is shown in (c), with the experimentally determined resolved shear stress on the active slip system 1⁄2 [1-11](-213) is shown in thick yellow horizontal line. [23]

probed by in situ neutron diffraction revealed the three stages of deformation [25]. The first stage is anisotropic elastic deformation, the second stage is load sharing from {110} to {200} grain family, and the third stage is the strain-hardening of the different grain families. There were no twinning or phase transformations that were observed in this system, therefore, the deformation mechanism is purely by slip. However, the study on the tension-compression asymmetry on BCC RHEAs in real time by employing in situ neutron diffraction is still lacking.

Precipitation strengthening in FeCoNi-HEAs

Precipitation strengthening has been utilized in various alloys systems such as steels [26-29] and Mg alloys [30-32], often improving the strength at the cost of its ductility. Unlike the traditional alloy systems, HEAs are multicomponent and could widen the alloy design space to develop novel precipitates with novel deformation mechanisms which have the potential to accomplish the strength and ductility synergy [1, 2]. As shown in Figure 5 [33], although precipitation-strengthening can enhance HEAs, the work hardening rate could be reduced, therefore resulting in earlier necking according to Considère criterion [34-38].

Several studies have highlighted the strength-ductility tradeoffs in HEAs. Liu et al. [35] added Mo into CoCrFeNi which formed hard σ and μ intermetallic phases, with yield strength, ultimate strength, and ductility of 816 MPa, 1.2 GPa, and 19%, respectively. Gwalani et al [39] studied the role of Cu clusters in Al0.3Cu0.3Ti0.2CoCrFeNi, which results in yield strength, ultimate strength, and ductility of 820 MPa, 1100 MPa, and 20%, respectively. Oxide dispersion [36] and L12 precipitations [37, 38] were added to FeCoNi

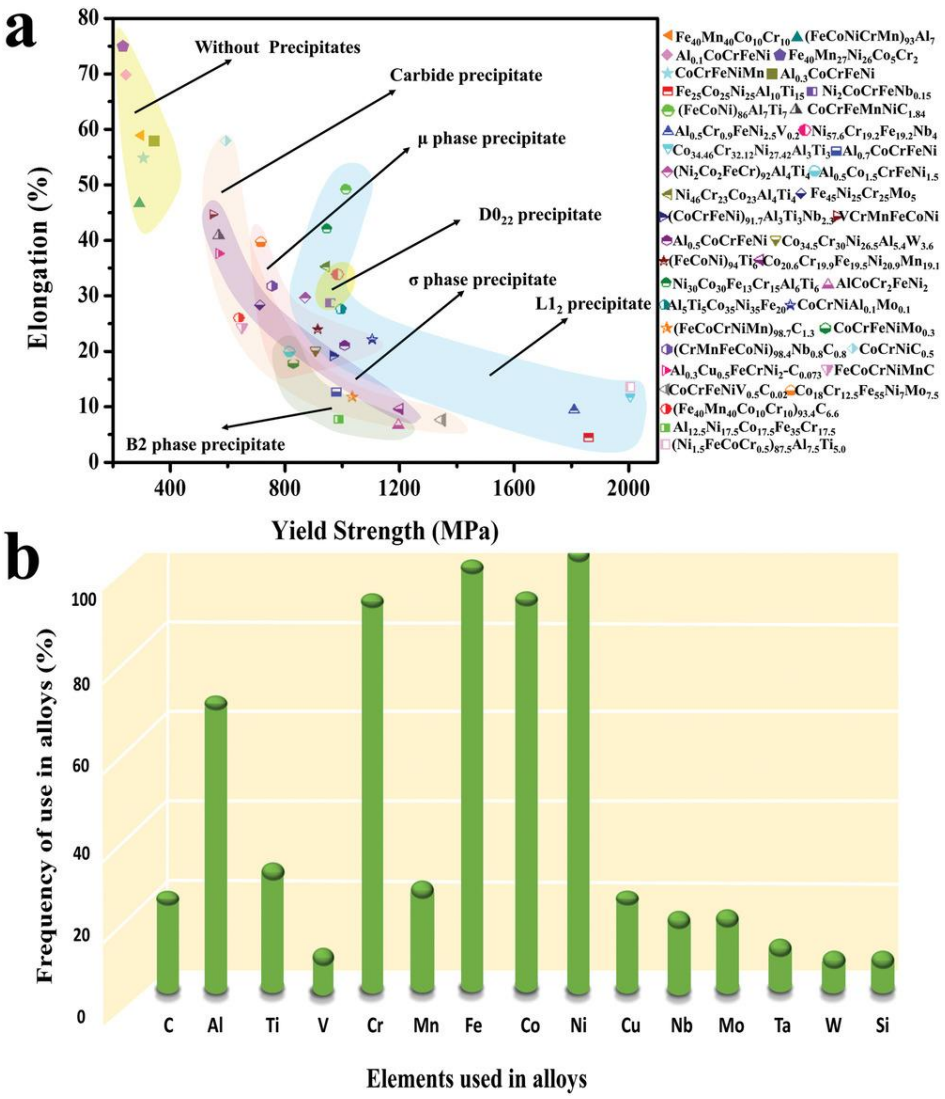


Figure 5 (a) Types of nanoprecipitates and their contribution to strength and (b) the frequency of elements used in nanoprecipitation-strengthened HEAs. [33]

as the base alloy to achieve up to five times the yield strength compared with the single-phase base alloy, although with an obvious ductility reduction. Yang et al. [40] proposed the multicomponent intermetallic nanoparticles (MCINPs) to break the strength-ductility trade-off in FeCoNi HEA by adding Al and Ti. The (FeCoNi)Al7Ti7 had ultimate strength up to 1500 MPa and ductility of 50% at room temperature. As shown in Figure 6, the strength-ductility synergy is attributed to the distinctive multistage work-hardening behavior, resulting from pronounced dislocation activities and formation of microbands at the late stage of deformation. Even with the recent success in utilizing the successive hardening mechanisms to obtain strength-ductility synergy, a major challenge is on the quantification of each contributing mechanisms to the overall hardening rate from the real-time deformation behavior.

Effect of alloying element on CoCrFeNi-HEAs

The effect of tuning the chemical composition of HEAs has been proven to enhance the mechanical behavior of CrCoNi-based HEAs [41]. A study comparing CoCrFeNiPd, CoCrFeMnNi, and the base alloy, CoCrFeNi, has shown that Pd addition increases the solid solution strengthening due to lattice size and shear modulus mismatch. Some alloy systems were also observed to have local elemental clustering that leads to compositional waves, acting as obstacles to dislocation motion and further strengthen the HEA. Beyond the solid solution effects, the formation of nanoprecipitates through alloying also improves mechanical performance [33].

For example, a small addition of Ti and Cu to Al0.3CoCrFeNi results in the formation of coherent L12 precipitates, increasing the yield strength to approximately 1100 MPa [39].

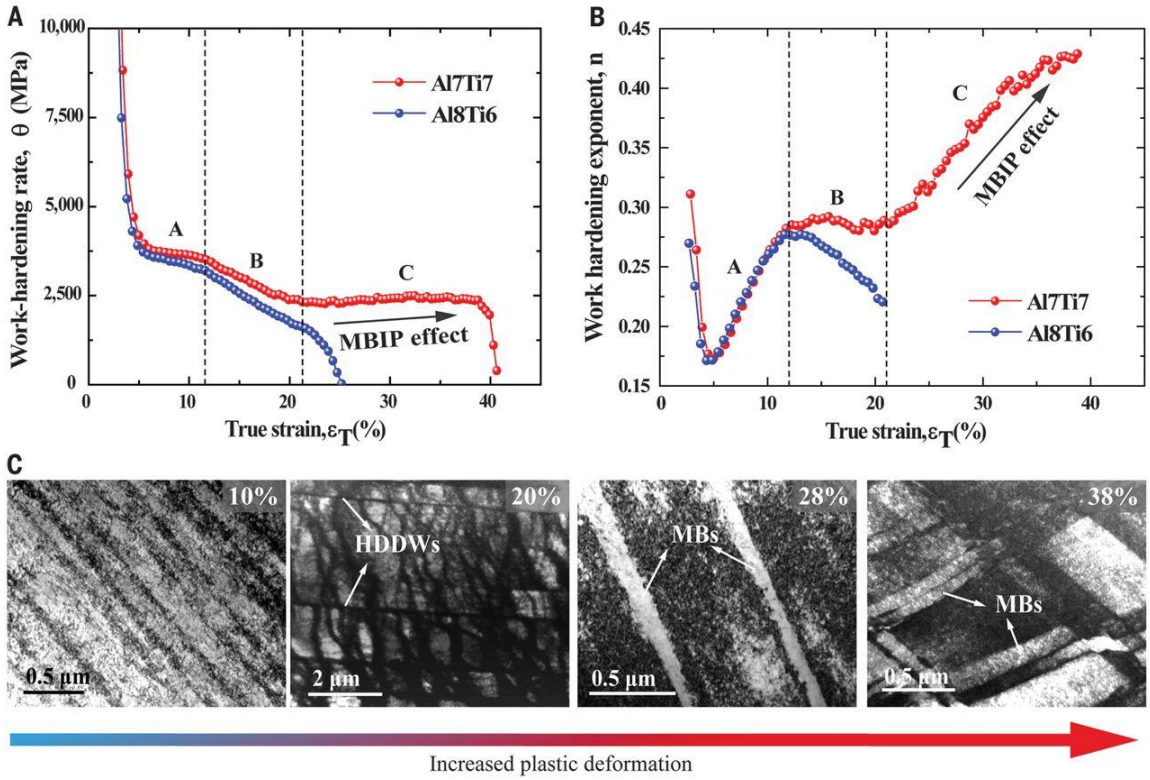


Figure 6 (a) Work-hardening rate and (b) work hardening exponent of $(FeCoNi)_{86}Al_7Ti_7$ and $(FeCoNi)_{86}Al_8Ti_6$. (c) evolution of deformation substructures of $(FeCoNi)_{86}Al_7Ti_7$ with increasing tensile loading, taken with transmission electron microscope.

In addition to the increase of strength, precipitates also contribute to improved ductility by dislocation bowing mechanisms, due to the dislocation and coherent L12 precipitate interactions. It was observed that Cu clusters act as nucleation sites for L12 precipitation. Furthermore, L21 precipitates were observed at the grain boundary, leading to grain boundary strengthening. While adding various alloying elements and its effect on mechanical properties, evolution of microstructure, and other properties of interest, have been studied in the past, they are rarely done within the same alloy systems [42-44].

The addition of Cu to CoCrFeNi has been reported to improve several functional properties, including wear resistance [45], high-temperature hardness [46], irradiation tolerance [47-49], corrosion resistance [50, 51], and have also been studied for semisolid state processing [52-54]. Figure 7 shows simulation study on CoCrCuFeNi, CoCrFeNi, and CoCrFeNiMn revealed that CoCrCuFeNi has the largest stair-rod and Hirth dislocation density compared to the other studied composition, acting as obstacles for dislocation [55]. Although Cu clustering has been studied in CoCrFeNi-xCu, their role in mechanical properties has not been investigated [56, 57]. Despite the aforementioned experimental and simulation studies, a systematic study of the compositional effect of Cu doping, the microstructural tunability, and the possible roles of nanoclusters, stacking faults, twinning, and their interactions in real time is still lacking.

Compositional effect on HfNbTaTiZr

Elemental composition plays an important role in dictating mechanical behavior and microstructural stability of HfNbTaTiZr. Yurchenko et al. [58] studied the chemical composition variations in Hf-Nb-Ta-Ti-Zr-Mo-V-Si. Three different systems,

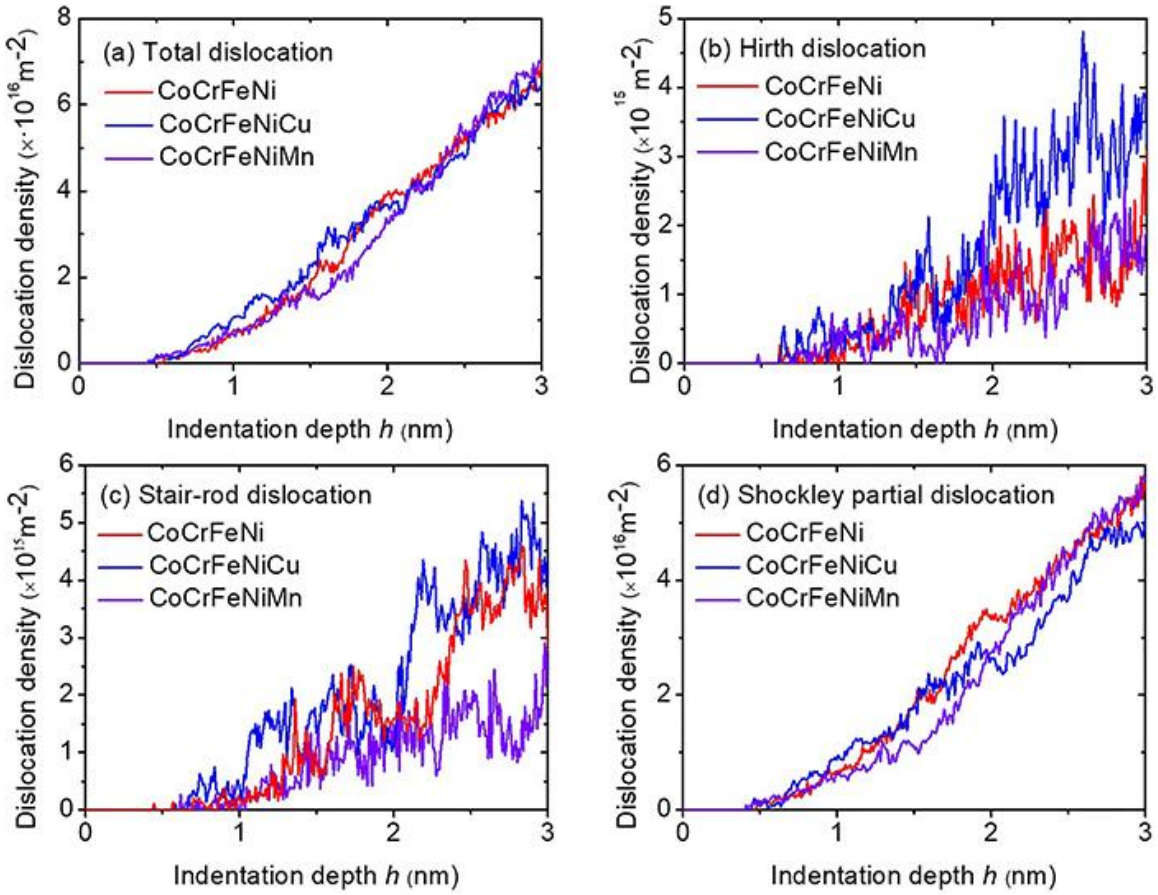


Figure 7 Simulated dislocation density as a function of indentation depth. (a) total dislocation; (b) Hirth dislocation; (c) stair-rod dislocation; (d) Shockley partial dislocation [55]

(HfNbTaTiZr)84Si16 (base-RHEA), (HfMoNbTaTiZr)84Si16 (Mo-RHEA), and (HfMoNbTaTiVZr)84Si16 (MoV-RHEA), in as-cast conditions are studied for microstructural changes and mechanical properties in compressive load. Microstructural studies show the formation of intermetallic compounds which are Me5Si3 in the base-RHEA and Me5Si3 and HFMoSi-type phase in the Mo- and MoV-RHEAs. At room temperature, the addition of Mo and V to the base-RHEA increased the strength in expense of the ductility.

Li et al. [59] studied the microstructure and tensile mechanical behavior of non-equimolar HfTaTiNbZr with varied Fe addition and heat treatments. It was found that Ti15Zr10Hf36.65Nb10Ta25Fe3.35 that was heat treated at 525ºC for 30 minutes and observed to have no Hf2Fe precipitates had the better strength-ductility synergy compared to the other materials studied with the Hf2Fe precipitates. Higher and longer heat treatment was reported to decrease the strength and ductility significantly.

Senkov et al. [60] studied the effects of varying Al, Hf, Mo, and Ta in HfNbTaTiZr system. At room temperature, compression test reveals the partial reduction of Hf and partial addition of Al in Al0.4Hf0.6NbTaTiZr formed a single-phase BCC structure and increased the yield strength to 1.85 GPa. Meanwhile, the addition of Al and the partial addition of Mo and Ta in AlMo0.5NbTa0.5TiZr formed a two-phase BCC structure and had the highest yield strength of up to 2 GPa. However, the ductility of these alloys only reached around 10% of strain.

Another study varying the element composition within the HfNbTaTiZr was conducted by Zýka et al. [61]. Various derivatives of HfNbTaTiZr (NbTaTi, TaTiZr,

NbTaTiZr, HfNbTaTiZr, Nb1.5TaTiZr0.5, and Nb0.5TaTiZr1.5) in as-cast condition were tested in room-temperature tension test. Submicron-sized precipitates were found in the grain boundaries of TaTiZr, Nb1.5TaTiZr0.5, and Nb0.5TaTiZr1.5. X-ray diffraction (XRD) patterns show HfNbTaTiZr and NbTaTi has single phase BCC structure, while the rest contain other BCC structures. Among these compositions, TaTiZr, Nb1.5TaTiZr0.5, and Nb0.5TaTiZr1.5 failed after yielding. NbTaTiZr possessed the lowest strength but highest ductility. Meanwhile, removing Hf from HfNbTaTiZr reduces the ductility and removing Hf and Ta reduces the strength. The compositional tuning in RHEAs often leads to the formation of intermetallic phases that either reduce the ductility, strength, or both. It is also a frequent phenomenon where the increase of strength comes with a significant reduction in ductility. Therefore, it is important to have a new approach in designing RHEAs to obtain strength-ductility synergy. Understanding the deformation behavior of HfNbTaTiZr and its derivatives in real time is also important to gain knowledge on the possible strengthening mechanisms.

References

1. Yeh, J.W., S.K. Chen, S.J. Lin, J.Y. Gan, T.S. Chin, T.T. Shun, C.H. Tsau, and S.Y. Chang, *Nanostructured high-entropy alloys with multiple principal elements: novel alloy design concepts and outcomes.* Advanced engineering materials, 2004. **6**(5): p. 299-303.
2. Cantor, B., I.T. Chang, P. Knight, and A. Vincent, *Microstructural development in equiatomic multicomponent alloys.* Materials Science and Engineering: A, 2004. **375**: p. 213-218.
3. Liu, H., L. Syama, L. Zhang, C. Lee, C. Liu, Z. Dai, and Q. Yan, *High-entropy alloys and compounds for electrocatalytic energy conversion applications.* SusMat, 2021. **1**(4): p. 482-505.
4. Verma, V., C.H. Belcher, D. Apelian, and E.J. Lavernia, *Diffusion in high entropy alloy systems–a review.* Progress in Materials Science, 2024. **142**: p. 101245.
5. Zhang, Y., T.T. Zuo, Z. Tang, M.C. Gao, K.A. Dahmen, P.K. Liaw, and Z.P. Lu, *Microstructures and properties of high-entropy alloys.* Progress in materials science, 2014. **61**: p. 1-93.
6. Lee, C., G. Song, M.C. Gao, R. Feng, P. Chen, J. Brechtl, Y. Chen, K. An, W. Guo, and J.D. Poplawsky, *Lattice distortion in a strong and ductile refractory high-entropy alloy.* Acta Materialia, 2018. **160**: p. 158-172.
7. Yao, M., K.G. Pradeep, C.C. Tasan, and D. Raabe, *A novel, single phase, non-equiatomic FeMnNiCoCr high-entropy alloy with exceptional phase stability and tensile ductility.* Scripta Materialia, 2014. **72**: p. 5-8.

8. Juan, C.-C., M.-H. Tsai, C.-W. Tsai, C.-M. Lin, W.-R. Wang, C.-C. Yang, S.-K. Chen, S.-J. Lin, and J.-W. Yeh, *Enhanced mechanical properties of HfMoTaTiZr and HfMoNbTaTiZr refractory high-entropy alloys.* Intermetallics, 2015. **62**(76): p. e83.

9. Shi, Y., B. Yang, P.D. Rack, S. Guo, P.K. Liaw, and Y. Zhao, *High-throughput synthesis and corrosion behavior of sputter-deposited nanocrystalline Alx (CoCrFeNi) 100-x combinatorial high-entropy alloys.* Materials & Design, 2020. **195**: p. 109018.

10. Joo, S.H., H. Kato, M.J. Jang, J. Moon, C.W. Tsai, J.W. Yeh, and H.S. Kim, *Tensile deformation behavior and deformation twinning of an equimolar CoCrFeMnNi high-entropy alloy.* Materials Science and Engineering: A, 2017. **689**: p. 122-133.

11. Laplanche, G., A. Kostka, O. Horst, G. Eggeler, and E. George, *Microstructure evolution and critical stress for twinning in the CrMnFeCoNi high-entropy alloy.* Acta Materialia, 2016. **118**: p. 152-163.

12. Stepanov, N., M. Tikhonovsky, N. Yurchenko, D. Zyabkin, M. Klimova, S. Zherebtsov, A. Efimov, and G. Salishchev, *Effect of cryo-deformation on structure and properties of CoCrFeNiMn high-entropy alloy.* Intermetallics, 2015. **59**: p. 8-17.

13. Considère, A., *Annales des ponts et chaussées.* Comm. Ann. Ponts Chaussees Paris, 1885. **9**: p. 574-575.

14. Woo, W., J. Jeong, D.-K. Kim, C. Lee, S.-H. Choi, J.-Y. Suh, S. Lee, S. Harjo, and T. Kawasaki, *Stacking fault energy analyses of additively manufactured stainless*

steel 316L and CrCoNi medium entropy alloy using in situ neutron diffraction. Scientific reports, 2020. **10**(1): p. 1350.

15. Frank, M., S. Nene, Y. Chen, S. Thapliyal, S. Shukla, K. Liu, S. Sinha, T. Wang, M. Frost, and K. An, *Direct evidence of the stacking fault-mediated strain hardening phenomenon.* Applied Physics Letters, 2021. **119**(8).
16. Mills, L.H., M.G. Emigh, C.H. Frey, N.R. Philips, S.P. Murray, J. Shin, D.S. Gianola, and T.M. Pollock, *Temperature-dependent tensile behavior of the HfNbTaTiZr multi-principal element alloy.* Acta Materialia, 2023. **245**: p. 118618.
17. Lee, C., G. Song, M.C. Gao, R. Feng, P. Chen, J. Brechtl, Y. Chen, K. An, W. Guo, J.D. Poplawsky, S. Li, A.T. Samaei, W. Chen, A. Hu, H. Choo, and P.K. Liaw, *Lattice distortion in a strong and ductile refractory high-entropy alloy.* Acta Materialia, 2018. **160**: p. 158-172.
18. Detor, A., S. Oppenheimer, R. Casey, and C. Crawford, *Refractory high entropy alloy dataset with room temperature ductility screening.* Data in Brief, 2022. **45**: p. 108582.
19. Pan, Y., T. Fu, M. Duan, C. Li, H. Hu, and X. Peng, *Tension–Compression Asymmetry of BCC NbMoTaW in High Entropy Alloy Nanowires.* ACS Applied Nano Materials, 2024. **7**(7): p. 8121-8129.
20. Pichl, W., *Slip Geometry and Plastic Anisotropy of Body-Centered Cubic Metals.* physica status solidi (a), 2002. **189**(1): p. 5-25.

21. Gröger, R. and V. Vitek, *Impact of non-Schmid stress components present in the yield criterion for bcc metals on the activity of {110}< 111> slip systems.* Computational Materials Science, 2019. **159**: p. 297-305.

22. Wang, Z. and I. Beyerlein, *An atomistically-informed dislocation dynamics model for the plastic anisotropy and tension–compression asymmetry of BCC metals.* International Journal of Plasticity, 2011. **27**(10): p. 1471-1484.

23. Wang, F., G.H. Balbus, S. Xu, Y. Su, J. Shin, P.F. Rottmann, K.E. Knipling, J.-C. Stinville, L.H. Mills, and O.N. Senkov, *Multiplicity of dislocation pathways in a refractory multiprincipal element alloy.* Science, 2020. **370**(6512): p. 95-101.

24. Lee, C., F. Maresca, R. Feng, Y. Chou, T. Ungar, M. Widom, K. An, J.D. Poplawsky, Y.-C. Chou, and P.K. Liaw, *Strength can be controlled by edge dislocations in refractory high-entropy alloys.* Nature communications, 2021. **12**(1): p. 5474.

25. Zhou, Y., W. Song, F. Zhang, Y. Wu, Z. Lei, M. Jiao, X. Zhang, J. Dong, Y. Zhang, M. Yang, Z. Lu, S. Harjo, T. Kawasaki, W. Gong, Y. Zhao, D. Ma, and Z. Lu, *Probing deformation behavior of a refractory high-entropy alloy using in situ neutron diffraction.* Journal of Alloys and Compounds, 2024. **971**: p. 172635.

26. Niu, M., G. Zhou, W. Wang, M.B. Shahzad, Y. Shan, and K. Yang, *Precipitate evolution and strengthening behavior during aging process in a 2.5 GPa grade maraging steel.* Acta Materialia, 2019. **179**: p. 296-307.

27. Li, Y., W. Yan, J.D. Cotton, G.J. Ryan, Y. Shen, W. Wang, Y. Shan, and K. Yang, *A new 1.9 GPa maraging stainless steel strengthened by multiple precipitating species.* Materials & Design, 2015. **82**: p. 56-63.

28. Xu, S., Y. Zhao, D. Chen, L. Sun, L. Chen, X. Tong, C. Liu, and Z. Zhang, *Nanoscale precipitation and its influence on strengthening mechanisms in an ultra-high strength low-carbon steel.* International Journal of Plasticity, 2019. **113**: p. 99-110.

29. Jiang, S., H. Wang, Y. Wu, X. Liu, H. Chen, M. Yao, B. Gault, D. Ponge, D. Raabe, and A. Hirata, *Ultrastrong steel via minimal lattice misfit and high-density nanoprecipitation.* Nature, 2017. **544**(7651): p. 460-464.

30. Xie, D., Z. Li, T. Sasaki, Y. Gao, Z. Lyu, R. Feng, Y. Chen, K. An, H. Chew, and T. Nakata, *Identifying the effect of coherent precipitates on the deformation mechanisms by in situ neutron diffraction in an extruded magnesium alloy under low-cycle fatigue conditions.* Acta Materialia, 2023. **251**: p. 118903.

31. Gao, L., R. Chen, and E. Han, *Microstructure and strengthening mechanisms of a cast Mg–1.48 Gd–1.13 Y–0.16 Zr (at.%) alloy.* Journal of materials science, 2009. **44**(16): p. 4443-4454.

32. Xie, D., Z. Lyu, M. Fan, H.B. Chew, P.K. Liaw, H. Bei, Z. Zhang, and Y. Gao, *Micromechanical origin of the enhanced ductility in twinless duplex Mg–Li alloy.* Materials Science and Engineering: A, 2021. **815**: p. 141305.

33. Liu, L., Y. Zhang, J. Han, X. Wang, W. Jiang, C.T. Liu, Z. Zhang, and P.K. Liaw, *Nanoprecipitate-strengthened high-entropy alloys.* Advanced Science, 2021. **8**(23): p. 2100870.

34. He, J., H. Wang, H. Huang, X. Xu, M. Chen, Y. Wu, X. Liu, T. Nieh, K. An, and Z. Lu, *A precipitation-hardened high-entropy alloy with outstanding tensile properties.* Acta Materialia, 2016. **102**: p. 187-196.

35. Liu, W., Z. Lu, J. He, J. Luan, Z. Wang, B. Liu, Y. Liu, M. Chen, and C. Liu, *Ductile CoCrFeNiMox high entropy alloys strengthened by hard intermetallic phases.* Acta Materialia, 2016. **116**: p. 332-342.

36. Guo, Y., M. Li, P. Li, C. Chen, Q. Zhan, Y. Chang, and Y. Zhang, *Microstructure and mechanical properties of oxide dispersion strengthened FeCoNi concentrated solid solution alloys.* Journal of Alloys and Compounds, 2020. **820**: p. 153104.

37. Chen, Y., H. Deng, Z. Xie, M. Wang, J. Yang, T. Zhang, Y. Xiong, R. Liu, X. Wang, and Q. Fang, *Tailoring microstructures and tensile properties of a precipitation-strengthened (FeCoNi) 94Ti6 medium-entropy alloy.* Journal of Alloys and Compounds, 2020. **828**: p. 154457.

38. Fu, A., B. Liu, S. Xu, J. Huang, Y. Zhang, Y. Cao, and Y. Liu, *Mechanical properties and microstructural evolution of a novel (FeCoNi) 86.93 Al6. 17Ti6. 9 medium entropy alloy fabricated via powder metallurgy technique.* Journal of Alloys and Compounds, 2021. **860**: p. 158460.

39. Gwalani, B., S. Gorsse, V. Soni, M. Carl, N. Ley, J. Smith, A.V. Ayyagari, Y. Zheng, M. Young, and R.S. Mishra, *Role of copper on L12 precipitation strengthened FCC based high entropy alloy.* Materialia, 2019. **6**: p. 100282.

40. Yang, T., Y. Zhao, Y. Tong, Z. Jiao, J. Wei, J. Cai, X. Han, D. Chen, A. Hu, and J. Kai, *Multicomponent intermetallic nanoparticles and superb mechanical behaviors of complex alloys.* Science, 2018. **362**(6417): p. 933-937.

41. Ding, Q., Y. Zhang, X. Chen, X. Fu, D. Chen, S. Chen, L. Gu, F. Wei, H. Bei, and Y. Gao, *Tuning element distribution, structure and properties by composition in high-entropy alloys.* Nature, 2019. **574**(7777): p. 223-227.

42. Salishchev, G., M. Tikhonovsky, D. Shaysultanov, N. Stepanov, A. Kuznetsov, I. Kolodiy, A. Tortika, and O. Senkov, *Effect of Mn and V on structure and mechanical properties of high-entropy alloys based on CoCrFeNi system.* Journal of Alloys and Compounds, 2014. **591**: p. 11-21.

43. Oh, M.C., A. Sharma, H. Lee, and B. Ahn, *Phase separation and mechanical behavior of AlCoCrFeNi-X (X= Cu, Mn, Ti) high entropy alloys processed via powder metallurgy.* Intermetallics, 2021. **139**: p. 107369.

44. Zhu, Z., K. Ma, Q. Wang, and C. Shek, *Compositional dependence of phase formation and mechanical properties in three CoCrFeNi-(Mn/Al/Cu) high entropy alloys.* Intermetallics, 2016. **79**: p. 1-11.

45. Lu, J., B. Wang, X. Qiu, Z. Peng, and M. Ma, *Microstructure evolution and properties of CrCuFexNiTi high-entropy alloy coating by plasma cladding on Q235.* Surface and Coatings Technology, 2017. **328**: p. 313-318.

46. Lin, C.-M. and H.-L. Tsai, *Equilibrium phase of high-entropy FeCoNiCrCu0. 5 alloy at elevated temperature.* Journal of Alloys and Compounds, 2010. **489**(1): p. 30-35.

47. Jiang, L., Y.J. Hu, K. Sun, P. Xiu, M. Song, Y. Zhang, W.L. Boldman, M.L. Crespillo, P.D. Rack, and L. Qi, *Irradiation-induced extremes create hierarchical face-/body-centered-cubic phases in nanostructured high entropy alloys.* Advanced Materials, 2020. **32**(39): p. 2002652.

48. Kombaiah, B., Y. Zhou, K. Jin, A. Manzoor, J.D. Poplawsky, J.A. Aguiar, H. Bei, D.S. Aidhy, P.D. Edmondson, and Y. Zhang, *Nanoprecipitates to enhance radiation tolerance in high-entropy alloys.* ACS applied materials & interfaces, 2023. **15**(3): p. 3912-3924.

49. Zhang, Y., Y.N. Osetsky, and W.J. Weber, *Tunable chemical disorder in concentrated alloys: defect physics and radiation performance.* Chemical Reviews, 2021. **122**(1): p. 789-829.

50. Mukanov, S., P. Loginov, A. Fedotov, M. Bychkova, M. Antonyuk, and E. Levashov, *The effect of copper on the microstructure, wear and corrosion resistance of CoCrCuFeNi high-entropy alloys manufactured by powder metallurgy.* Materials, 2023. **16**(3): p. 1178.

51. Lach, T.G., C.M. Silva, Y. Zhou, W.L. Boldman, P.D. Rack, W.J. Weber, and Y. Zhang, *Dynamic substrate reactions during room temperature heavy ion irradiation of CoCrCuFeNi high entropy alloy thin films.* npj Materials Degradation, 2022. **6**(1): p. 60.

52. Campo, K.N., C.C. de Freitas, L. Fanton, and R. Caram, *Melting behavior and globular microstructure formation in semi-solid CoCrCuxFeNi high-entropy alloys.* Journal of materials science & technology, 2020. **52**: p. 207-217.

53. de Freitas, C.C., R. Caram, and K.N. Campo, *Semisolid deformation behavior and processing of CoCrCuxFeNi high-entropy alloys.* Intermetallics, 2022. **150**: p. 107682.

54. Rogal, Ł., *Semi-solid processing of the CoCrCuFeNi high entropy alloy.* 2017.

55. Qi, Y., T. He, and M. Feng, *The effect of Cu and Mn elements on the mechanical properties of single-crystal CoCrFeNi-based high-entropy alloy under nanoindentation.* Journal of Applied Physics, 2021. **129**(19).

56. Nam, S., J.Y. Hwang, J. Jeon, J. Park, D. Bae, M.J. Kim, J.-H. Kim, and H. Choi, *Deformation behavior of nanocrystalline and ultrafine-grained CoCrCuFeNi high-entropy alloys.* Journal of Materials Research, 2019. **34**(5): p. 720-731.

57. San, S., Y. Tong, H. Bei, B. Kombaiah, Y. Zhang, and W.-Y. Ching, *First-principles calculation of lattice distortions in four single phase high entropy alloys with experimental validation.* Materials & Design, 2021. **209**: p. 110071.

58. Yurchenko, N., V. Mirontsov, E. Mishunina, and N. Stepanov, *Effect of chemical composition variations in refractory Hf-Nb-Ta-Ti-Zr-Mo-V-Si complex concentrated alloys on the structure, mechanical properties, and oxidation behaviour.* Materials Characterization, 2025. **222**: p. 114856.

59. Li, J., H. Ke, B. Wang, L. Wang, and Y. Xue, *Ductility Control via Nano-Precipitation at Grain Boundaries in Ti-Zr-Hf-Nb-Ta Multi-Principal Element Alloys.* Materials, 2025. **18**(7): p. 1463.

60. Senkov, O.N., S.V. Senkova, and C. Woodward, *Effect of aluminum on the microstructure and properties of two refractory high-entropy alloys.* Acta Materialia, 2014. **68**: p. 214-228.

61. Zýka, J., J. Málek, J. Veselý, F. Lukáč, J. Čížek, J. Kuriplach, and O. Melikhova, *Microstructure and Room Temperature Mechanical Properties of Different 3 and 4 Element Medium Entropy Alloys from HfNbTaTiZr System.* Entropy, 2019. **21**(2): p. 114.

62. Senkov, O., G. Wilks, D. Miracle, C. Chuang, and P. Liaw, *Refractory high-entropy alloys.* Intermetallics, 2010. **18**(9): p. 1758-1765.

63. Fleischer, R.L., *Substitutional solution hardening.* Acta metallurgica, 1963. **11**(3): p. 203-209.

64. Gypen, L. and A. Deruyttere, *Multi-component solid solution hardening: Part 2 agreement with experimental results.* Journal of materials science, 1977. **12**(5): p. 1034-1038.

CHAPTER II

COPPER EFFECTS ON THE MICROSTRUCTURES AND DEFORMATION MECHANISMS OF CoCrFeNi HIGH ENTROPY ALLOYS

This chapter was published in Applied Physics Letters by Lia Amalia, Yongkang Li, Hongbin Bei, Yan Chen, Dunji Yu, Ke An, Zongyang Lyu, Peter K. Liaw, Yanwen Zhang, Qingqing Ding, and Yanfei Gao:

Lia Amalia, Yongkang Li, Hongbin Bei, Yan Chen, Dunji Yu, Ke An, Zongyang Lyu, Peter K. Liaw, Yanwen Zhang, Qingqing Ding, Yanfei Gao. "Copper effects on the microstructures and deformation mechanisms of CoCrFeNi high entropy alloys." Applied Physics Letters 124, no. 14 (2024).

This chapter is adapted from the published article and has been reformatted to conform to the formatting requirements of the University of Tennessee, Knoxville, and to fit the structure of this dissertation. The author contributions are retained as reported in the published article using the CRediT author contribution taxonomy. Lia Amalia contributed equally to data curation, formal analysis, investigation, methodology, project administration, resources, software, validation, visualization, writing–original draft, and writing–review and editing. The coauthors contributed to the original publication through combinations of conceptualization, data curation, formal analysis, funding acquisition, investigation, methodology, project administration, resources, software, supervision, validation, visualization, writing–original draft, and writing–review and editing, as stated in the published article.

Abstract

In situ neutron diffraction experiments have been performed to investigate the deformation mechanisms on CoCrFeNi high entropy alloys (HEAs) with various amounts of doped Cu. Lattice strain evolution and diffraction peak analysis were used to derive the stacking fault probability, stacking fault energy, and dislocation densities. Such diffraction analyses indirectly uncovered that a lower degree of Cu doping retained the twinning behavior in undoped CoCrFeNi HEAs while increasing Cu content increased the Cu clusterings which suppressed twinning and exhibited prominent dislocation strengthening. These results agree with direct observations by transmission electron microscopy.

Introduction

High entropy alloys (HEAs) which were independently developed by Yeh and Cantor have uncovered novel deformation mechanisms, contrasting typical traditional alloys in the past twenty years [1, 2]. Previous studies revealed that HEAs possess unique features such as short-range ordering (SRO) [3], large lattice distortion [4], transformation-induced plasticity (TRIP) [5], twinning-induced plasticity (TWIP) [6], strong and dense nanoprecipitates [7] and compositional waves [8], which led to enhancement of mechanical properties. Although these interesting mechanisms have previously been revealed, it needs to be pointed out that they operate in vastly different alloy systems, making it elusive to quantitatively assess and compare these mechanisms. It is more desirable to have one alloy system that has the potential to be developed into a wide range of microstructural features, deformation mechanisms, and desirable properties so that quantitative comparisons could

be done, similar to existing conventional alloy systems such as nickel-based superalloys [9] and stainless steels [10].

At the early stage of research on HEAs, CoCrFeMnNi was one of the pioneering alloy systems that was studied for its mechanical behavior. CoCrFeMnNi revealed interesting mechanical behavior, especially at cryogenic temperatures, where both ductility and ultimate strength were increased up to 60% elongation to failure and 1000 MPa, respectively [11]. At cryogenic temperature, twinning is activated from approximately 8% of true strain, with nanoscale twin size and micrometer-scale spacing which act as boundaries for dislocation motion, providing the dynamic Hall-Petch effect [11]. At room temperature, the ultimate strength decreased to 460 MPa with elongation to failure of around 45% [11]. At an earlier stage of deformation, slip occurs on {111} planes by the planar glide of ½<110>, then split into 1/6<112> Shockley partial dislocation. At further stages of deformation, around 15-20% of straining, the partial dislocations are activated on multiple-slip systems, increasing the dislocation density. Towards the last stage of deformation, twinnings are finally formed [11, 12].

Tuning the element and chemical composition of HEAs has been shown to enhance the mechanical behavior of CrCoNi-based HEAs [8]. By comparing CrCoFeNiPd and CrCoFeNiMn to CrCoFeNi, it was found that Pd addition increased the solid solution strengthening due to lattice size and shear modulus mismatch between CrCoFeNiPd and CrCoFeNi. Element clusterings leading to compositional waves were also reported to increase the obstacle-hardening effect. Incorporating nanoprecipitates by element tuning has also been reported to increase the strength of HEAs [7]. A small addition of Ti and Cu

to Al0.3CoCrFeNi was reported to form L12 coherent precipitates and increase the strength to 1100MPa [13]. Cu clusters also act as nucleation sites for L12 precipitates and contribute to the increased strength. The interaction of dislocation and precipitate was observed to be the bowing mechanism, leading to enhanced ductility. It was reported that higher strengthening was observed in the sample with smaller L12 particles. L21 precipitates were also observed to populate the grain boundaries, which could lead to grain boundary strengthening [13]. Even though the effect of different compositions of alloying elements in high entropy alloys has been studied, it is rarely done within the same alloy system and to explicate the evolution of microstructure, mechanical properties, and other properties of interest caused by fine element tuning [14-16].

Cu addition to CoCrFeNi-based HEA was reported to improve wear resistance [17], high-temperature hardness [18], irradiation tolerance [19-21], and corrosion resistance [22, 23], they have also been studied for semisolid state processing [24-26]. A simulation study revealed that CoCrCuFeNi has the largest stair-rod and Hirth dislocations density compared to CoCrFeNi and CoCrFeNiMn, acting as obstacles for dislocation [27]. Cu clusterings were observed in previous studies of CoCrFeNi-xCu, but their role in mechanical properties has not been fully investigated [28, 29]. Despite the above simulation and experimental studies, a systematic study of the compositional effect of Cu doping and the resulting microstructural tunability is still lacking, especially the roles played by possible nanoclusters, stacking faults, twinning, and their interactions are not clear.

Methods

In this study, we investigate the effect of increasing Cu content to CoCrFeNi (CoCrFeNi-xCu, x=1, 3, and 5) by utilizing in situ neutron diffraction experiment. The specimens were prepared using arc melter, homogenized at 1100oC for 8 hours, rolled with 86% reduction, and annealed at 1050oC for 30 minutes. Scanning electron microscopy (SEM) equipped with energy-dispersive spectroscopy (EDS), together with transmission electron microscopy (TEM), has been used for microstructural characterization. TEM studies were conducted to observe the microstructural change after the tension test. The TEM samples were taken from both the undeformed samples and the gauge region. After grinding until around 50μm thickness, the samples were electrochemically polished using twin-jet polishing with 5vol% perchloric acid-95vol% ethanol solution.

Figures 8a, b, and c show SEM images of the as-fabricated CoCrFeNi-1Cu, CoCrFeNi-3Cu, and CoCrFeNi-5Cu, respectively, showing all samples having similar grain sizes of around 70μm. EDS element maps on CoCrFeNi-1Cu and CoCrFeNi-5Cu in Figures 8d and e, respectively. Both CoCrFeNi-1Cu and CoCrFeNi-5Cu show the clusterings of Cu. However, the Cu cluster size in CoCrFeNi-1Cu is noticeably smaller compared to those in CoCrFeNi-5Cu. Many studies of the CoCrCuFeNi alloy system reported Cu clusterings, which sometimes could be identified in the x-ray diffraction pattern, overlapping with the FCC matrix diffraction pattern [18, 22]. Consequently, our focus of this work is placed on the connection between microstructural change (i.e., from homogenous solution without Cu doping to nanoclusters with 1Cu, 3Cu, and 5Cu) and mechanical properties (i.e., from twinning/stacking-fault behavior in CoCrFeNi to possible

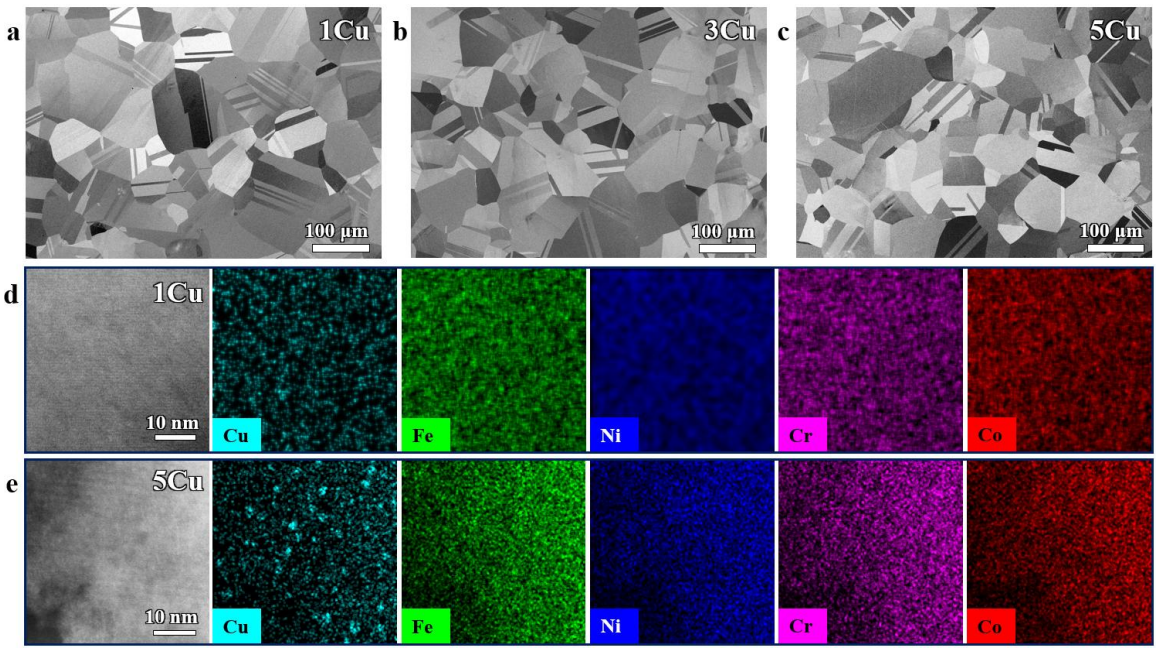


Figure 8. Scanning electron microscope (SEM) images of the (a) CoCrFeNi-1Cu, (b) CoCrFeNi-3Cu, and (c) CoCrFeNi-5Cu microstructures showing similar grain sizes (around 70µm) and EDS element map images of (d) CoCrFeNi-1Cu showing smaller sized clusterings of Cu, and (e) of CoCrFeNi-5Cu showing larger sized Cu clusters.

nanocluster-strengthening mechanisms in 1Cu, 3Cu, and 5Cu).

Utilizing in situ neutron diffraction techniques allows for observation and quantitative investigation of microstructural change during tensile loading, such as peak intensity, peak width, d-spacing, and individual lattice strain, making the observation of interesting mechanical behavior possible [30]. In this work, in situ neutron diffraction studies were performed in the Spallation Neutron Source (SNS), Oak Ridge National Laboratory (ORNL), using the engineering diffractometer in the VULCAN beamline [31]. There are two detector banks at ± 90o to the incident beam for the diffraction data collection, which corresponds to the neutron diffraction in the loading direction with the vector of diffraction parallel to the applied load (Bank 1 (Q||) Detector) and transverse direction with the vector of diffraction perpendicular to the applied load (Bank 2 (Q⊥) Detector) (Figure 9a). The samples were machined as per the requirement of VULCAN room temperature tension 3-mm dog bone plate sample (gauge size: 15 × 2.6 × 3 mm). The specimens were loaded in tension until fracture with a strain rate of 2×10^{-4} s^{-1}, which is a relatively slow strain rate to allow a sufficient neutron penetration to the sample.

The obtained diffraction data were chopped into 180-second intervals. GSAS software was used to conduct the full-pattern Rietveld refinement to observe the lattice parameter changes and phase fractions during loading. The data were also analyzed using single peak fitting by the VDRIVE software to obtain the hkl-specific behavior of the sample [32]. The lattice-specific strain (ε_{hkl}) was obtained by calculating the ratio of the difference of lattice spacing of the specific orientation (d_{hkl}) to the orientation-specific lattice spacing prior to loading ($d_{0,hkl}$), as shown in Eq. 1.

$$\varepsilon_{hkl} = \frac{d_{hkl} - d_{0,hkl}}{d_{0,hkl}} \quad (1)$$

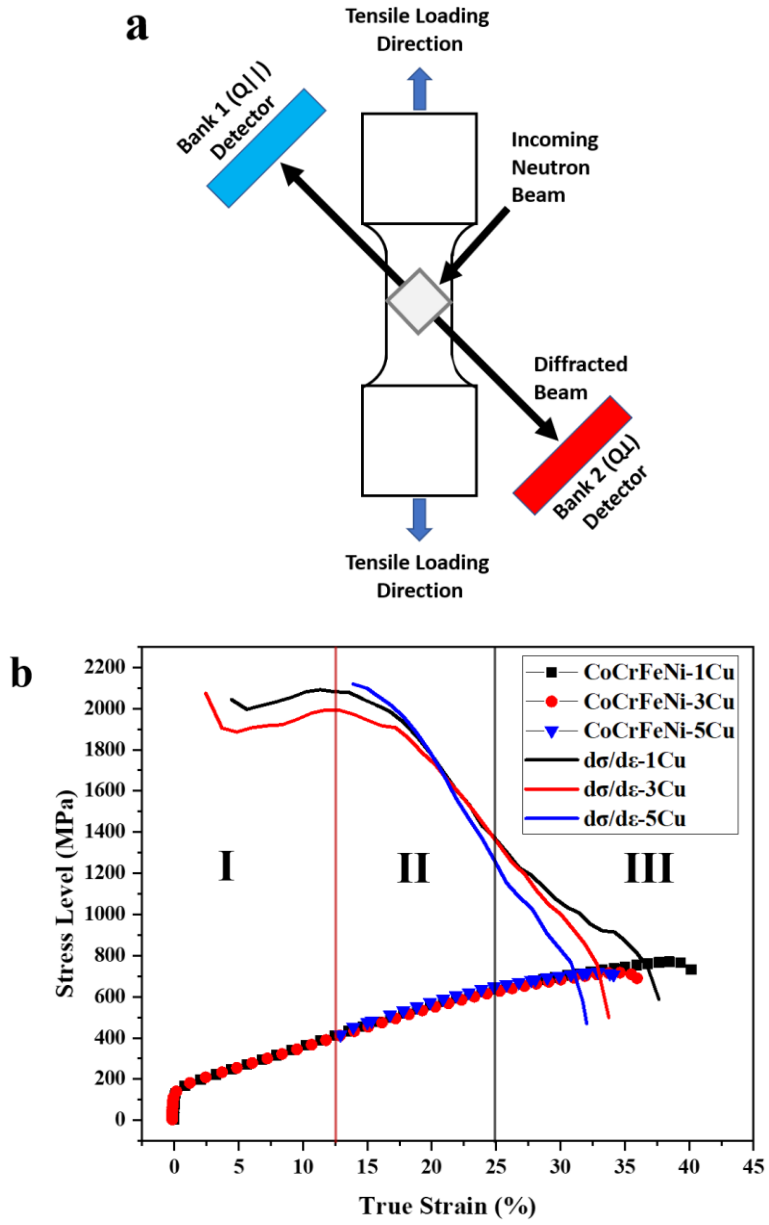


Figure 9. (a) Schematic drawing of the experimental setup at Vulcan beamline, SNS, ORNL. (b) True stress versus true strain overlapping with the work hardening rate (dσ/dε) of CoCrFeNi-1Cu, CoCrFeNi-3Cu, and CoCrFeNi-5Cu, showing three different regions of deformation behavior.

The stacking fault energy (SFE) is calculated with Reed and Schramm's relationship shown in Eq. 2 [33, 34], where a_0 is lattice parameter (nm), Psf is the stacking fault probability (SFP), $\langle \varepsilon_{50}^2 \rangle_{111}$ is the mean square strain, and C11, C12, and C44 are the single-crystal elastic constants (SCECs) [35]. SFP was evaluated by Eq. 3 from the peak shift caused by stacking fault which was caused by the difference in lattice strains of {111} and {222} grains in FCC, while $\frac{1}{0.0517}$ was derived from reflection quantity of (111) and (222) orientation. Mean square strain, $\langle \varepsilon_{50}^2 \rangle_{111}$, were calculated using the integral breadth method with pseudo-Voigt convolution (Eq. 4) [36].

$$SFE = \frac{6.6a_0}{\pi\sqrt{3}} \left(\frac{2c_{44}}{c_{11}-c_{12}} \right)^{-0.37} \frac{\langle \varepsilon_{50}^2 \rangle_{111}}{P_{sf}} \left(\frac{c_{44}+c_{11}-c_{12}}{3} \right) \quad (2)$$

$$P_{sf} = \frac{1}{0.0517} \left(\varepsilon_{\{222\}} - \varepsilon_{\{111\}} \right) \quad (3)$$

$$\langle \varepsilon_{50}^2 \rangle^{1/2} = 2\pi^{1/2} \beta_G \frac{d_{hkl}}{2} \quad (4)$$

The dislocation density was obtained from the modified Williamson-Hall peak broadening analysis (Eq. 5) [37, 38], where $\Delta K = -K(\Delta d/d)$ and $K = 1/d$, with *d* is d-spacing (nm) and Δd is the peak broadening in the full-width at half maximum (FWHM) (nm). *D* is the grain size, *A* is a constant that depends on the effective outer cutoff radius of dislocation, *b* is Burger's vector of the dislocation ($b = \sqrt{2}a_0/2$), ρ is the dislocation density, and the last term refers to a noninterpreted higher-order term. C can be calculated using Eq. 6 which depends on C_{h00} and q where their values are dependent on the dislocation type, the centering of the crystal, and the ratio of C_{12}/C_{44}, with C_{h00} calculated using ANIZC software [39]. Dislocation density can be obtained by plotting $(\Delta K)^2$ versus K^2C of the *(hkl)* reflections, where the slope of linear regression is equivalent to $(\pi A^2 b^2/2)\rho$. The

value of A needs to be determined using an initial value of dislocation density. In this study, we use the published value of dislocation density of CoCrFeNi in [40], 6.3×10^{14} m^{-2}, which makes the A value in our case to be 0.429. The initial value of dislocation density was chosen because of the similar sample initial condition.

$$(\Delta K)^2 = (0.9/D)^2 + (\pi A^2 b^2)\rho(K^2C) + O(K^2C)^2 \quad (5)$$

$$C = C_{h00}\left(1 - q\frac{h^2k^2+h^2l^2+k^2l^2}{(h^2+k^2+l^2)^2}\right) \quad (6)$$

Results and Discussion

Figure 9b shows the true stress-strain curves and the work-hardening behaviors for CoCrFeNi-1Cu, CoCrFeNi-3Cu, and CoCrFeNi-5Cu. Due to the diffraction apparatus problem during testing, only half of the CoCrFeNi-5Cu data could be acquired, therefore we could not obtain information on CoCrFeNi-5Cu during elastic deformation. All samples have similar yield strengths, which are 140 MPa and 142 MPa for CoCrFeNi-1Cu and CoCrFeNi-3Cu, respectively. The ultimate tensile strengths for CoCrFeNi-1Cu, CoCrFeNi-3Cu, and CoCrFeNi-5Cu are 770 MPa, 717 MPa, and 719 MPa respectively. The elongations to failure are 40%, 35%, and 34% for CoCrFeNi-1Cu, CoCrFeNi-3Cu, and CoCrFeNi-5Cu, respectively. The addition of copper is observed to not change the yield strength and only slightly reduced the ultimate tensile strength and elongation to failure. However, as will be shown shortly, the deformation mechanisms are radically different in these different alloys.

Based on Considère's necking criterion, when the strain hardening rate is equal to the stress in the uniaxial tensile stress-strain curve ($d\sigma/d\varepsilon = \sigma$), necking is predicted to occur [41]. As can be observed from Figure 9b, the necking occurred approximately at 759 MPa

and 36.6% strain in CoCrFeNi-1Cu, 709 MPa and 33% strain in CoCrFeNi-3Cu, and 710 MPa and 31% strain in CoCrFeNi-5Cu. For CoCrFeNi-1Cu, the work hardening rate increased at Stage I and then decreased at Stage II. The decreasing rate slows down slightly towards the end, which is thus denoted as Stage III after 25% of strain. Meanwhile, the work hardening rate of CoCrFeNi-3Cu and CoCrFeNi-5Cu increased at Stage I but continued to decrease from Stage II until failure occurred. However, even when the addition of copper slightly reduced the elongation to failure and ultimate tensile strength, the mechanical behavior of CoCrFeNi-3Cu and CoCrFeNi-5Cu could still keep up with CoCrFeNi-1Cu. It compels us to look closer at the microstructural behavior of these alloys to explain the differences in deformation behavior.

Figures 10a and b show the measured diffraction patterns collected during the tensile loading for CoCrFeNi-1Cu and CoCrFeNi-3Cu. Both samples show only one phase during loading, which is the face-centered cubic (FCC) phase. Figures 10c and d show the lattice strain evolution of CoCrFeNi-1Cu and CoCrFeNi-3Cu obtained from the single peak fitting analysis. Two deformation stages could be observed from the slope of these lattice strains which are the elastic deformation and plastic deformation. Elastic deformation occurs below the yield point (around 140 MPa) where all grain orientation is shown to have a linear relationship between the applied stress and the corresponding lattice strain. The plastic deformation behavior occurs after the yield point where there are nonlinear relationship between the applied stress and the corresponding lattice strain. For cubic materials, the anisotropy of the grain orientation could be characterized by the cubic elastic anisotropy factor A_{hkl} (Eq.7), where h, k, and l are the Miller indices of the grains.

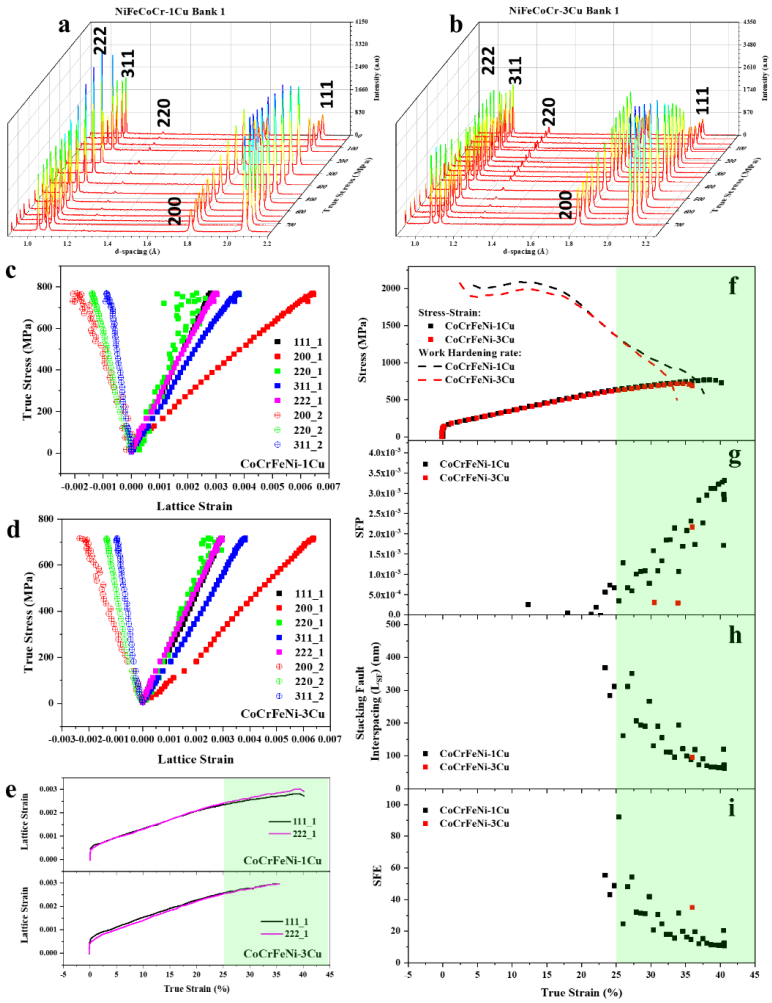


Figure 10. The measured diffraction patterns upon tensile loading, collected at bank 1 (corresponding to loading direction) for (a) CoCrFeNi-1Cu and (b) CoCrFeNi-3Cu. The evolution of lattice strains in loading (bank 1) and transversal direction (bank 2) of (c) CoCrFeNi-1Cu and (d) CoCrFeNi-3Cu. (e) showed the lattice strain difference between {111} and {222} in CoCrFeNi-1Cu and CoCrFeNi-3Cu, indicating stacking fault formation. Higher (f) work hardening rate and (g) stacking fault probability, with lower (h) stacking fault interspacing and (i) stacking fault energy of CoCrFeNi-1Cu starting from 25% of strain as compared to CoCrFeNi-3Cu.

The elastic strain of a specific grain orientation diffracted from the loading direction and transversal direction can be predicted using Eq. 8, respectively. With that, the modulus of elasticity of a specific grain (E_{hkl}) could be calculated using Eq. 9 [42].

$$A_{hkl} = \frac{h^2k^2+k^2l^2+h^2l^2}{(h^2+k^2+l^2)^2} \tag{7}$$

$$\frac{\varepsilon_{hkl,LD}}{\sigma} = S_{11} - 2[S_{11} - S_{12} - 0.5S_{44}]A_{hkl} \tag{8}$$

$$E_{hkl} = \frac{\sigma}{\varepsilon_{hkl}} \tag{9}$$

S11, S12, and S44 are elastic compliance of the material obtained from the Kroner's self-consistent model. The calculated values are summarized in Table 1 and Table 2. Figures 10c and 10d show the {200} grains have the lowest elastic modulus, with {311} grains shown to be the second lowest, then the other grains, {220}, {111}, and {222}, have the higher elastic modulus, which is consistent with the calculated Ehkl in Table 2, cubic structure's elastic anisotropy factor, and other reported data [43, 44].

During the plastic deformation, the applied load is distributed among the grains where softer grain families such as {220} transfer the load to the harder grain families, in this case {200} grains. Generally, both CoCrFeNi-1Cu and CoCrFeNi-3Cu follow this trend. However, some differences are noticeable. In FCC crystalline materials, the change in Bragg scattering positions in {111} and {222} could occur if stacking faults are formed, otherwise they would have the same value [45]. Figure 10e shows the difference of {111} and {222} in loading direction in CoCrFeNi-1Cu starting from 25% true strain, which we do not see in CoCrFeNi-3Cu, indicating stacking faults forming in CoCrFeNi-1Cu but not in CoCrFeNi-3Cu. Figure 10f shows the last stage of the work hardening rate evolution during tensile loading, showing CoCrFeNi-1Cu having a larger work hardening rate

Table 1. Calculated elastic constants.

	S_{11}	S_{12}	S_{44}	C_{11}	C_{12}	C_{44}
	10^{-2} GPa^{-1}			GPa		
CoCrFeNi-1Cu	0.716	-0.267	1.197	250.61	148.88	83.54
CoCrFeNi-3Cu	0.965	-0.401	1.094	253.42	180.18	91.40

Table 2. Calculated elastic moduli with respect to specific grain orientations.

Grain orientation	**111**	**200**	**220**	**311**	**222**
A_{hkl}	0.33	0	0.25	0.16	0.33
	Calculated E_{hkl} along the loading direction (LD) (GPa)				
CoCrFeNi-1Cu	217.50	139.64	190.89	167.96	217.50
CoCrFeNi-3Cu	238.67	103.66	180.05	141.32	238.67

compared to CoCrFeNi-3Cu starting at a true strain of 25%. Coincidentally, as shown in Figure 10g the stacking fault probability of CoCrFeNi-1Cu started to increase from around 1×10^{-4} to 3.317×10^{-3}. Meanwhile, the stacking fault probability of CoCrFeNi-3Cu is negligible since there are barely any differences in {111} and {222} lattice strains. Stacking fault probability can also be defined as the stacking fault formation frequency along the {111} plane in the FCC structure. Stacking fault interspacing is defined as the space between formed stacking faults, with a larger value indicating fewer stacking faults were formed. The average value of interspacing between formed stacking faults (L_{sf}) could be estimated using stacking fault probability and the d-spacing of {111} grain (Eq. 10) [46, 47].

$$L_{sf} = \frac{d_{111}}{P_{sf}} \tag{9}$$

Figure 10h shows the evolution of stacking fault interspacing with increasing strain. During elastic deformation, the L_{sf} of CoCrFeNi-1Cu reached 368 nm. The stacking fault interspacing continued to decrease with increasing strain levels where CoCrFeNi-1Cu reached saturation in L_{sf} value of around 62 nm. Note that reported stronger materials such as Co-Cr-Mo alloy [47] and $Fe_{40}Mn_{20}Cr_{15}Co_{20}Si_5$ [46] had around 10 nm of L_{sf} after being heavily deformed. Since the stacking fault probability of CoCrFeNi-3Cu is negligible, we do not see clear evolution of stacking fault interspacing. The decrease in interspacing of stacking fault is correlated with the increased fault density as the material continues to deform until it breaks. The stacking fault hardening phenomenon has also been reported where it was experimentally observed that the increase in stacking fault interspacing corresponded to the delay of decrease in macroscopic strain hardening during plastic

deformation and the collapse of fault interspacing enabled strain hardening in $Fe_{38.5}Mn_{20}Cr_{15}Co_{20}Si_5Cu_{1.5}$ [48].

Stacking fault energy is indicative of how easily a perfect dislocation splits into two partial dislocations. The range of SFE values has been used to indicate the deformation mechanism in various metals and also in high-entropy alloys. The SFE of less than 20 mJ/m^2 is reported in materials with phase transformation during loading, SFE between 20 to 45 mJ/m^2 typically deform by twinning, while SFE beyond 45 mJ/m^2 deform by slip [10, 34, 49]. The stacking fault energy (SFE) of CoCrFeNi-1Cu and CoCrFeNi-3Cu is presented in Figure 10i. In CoCrFeNi-3Cu the lattice strain of {222} grain never surpasses the lattice strain of {111} grain, until a few data points near the end of tensile loading, which explains why there is only one visible SFE in Figure 10i. In CoCrFeNi-1Cu, the SFE value is around 50 mJ/m^2 at around 25% of true strain, then gradually decreases to the value of 30 to 10 mJ/m^2 until the sample breaks. The average SFE of CoCrFeNi-1Cu is around 37 mJ/m^2. The evolution of SFE with increasing strain levels could be correlated to the changes in the deformation substructure [34]. TEM study on CoCrFeNi fabricated with high-pressure torsion reported the change of microstructure with the observation of nanoband, twinning, nanoband interactions, and nanoband-twin interactions with increasing deformation level [50]. Hence, the in situ neutron diffraction patterns during deformation which captured the microstructural changes during deformation could provide us with parameters related to faulting, such as SFP, L_{sf}, and SFE, and their changes at each level of strain. Therefore, in the case of CoCrFeNi-1Cu, the increase of work hardening rate at stage III, as seen in Figure 9b is caused by the formation of twins, causing the

dynamic Hall-Petch effect, consistent with the TEM evidence in Figure 11b and literature [11].

The dislocation density of CoCrFeNi-1Cu and CoCrFeNi-3Cu in common edge (<111>{110} type) and screw (<111> type) dislocation system at a true strain of 1%, 5%, 12%, 15%, 20%, 25%, 30%, and 35% is presented in Figure 11a and summarized in Table 3. The value of dislocation density of CoCrFeNi-3Cu shows minor differences as compared to CoCrFeNi-1Cu. There are also minor differences between edge and screw dislocations in both CoCrFeNi-1Cu and CoCrFeNi-3Cu. Figure 11**Error! Reference source not found.**c shows the microstructure image using TEM on CoCrFeNi-5Cu after the tensile test. The TEM image of highly deformed CoCrFeNi-5Cu shows many dislocations was formed after tensile loading, where the density of dislocation agrees with the calculated dislocation density listed in Table 3. This goes to show that although CoCrFeNi-3Cu did not form twinnings, it formed enough dislocations, resulting in comparable strength compared to CoCrFeNi-1Cu. The addition of Cu in CoCrFeNi was reported to form a Cu-rich FCC phase, suggesting the low solubility of Cu in CoCrFeNi [51]. The in-situ neutron diffraction analyses and TEM observations suggest that adding more Cu alters the stacking fault formation behavior which in turn alters the deformation mechanism of this alloy system where twins formation is not necessary to achieve comparable strength. Suppression of twinning has been reported previously in various systems where it is most likely due to the lower energy of deforming in another way, hence twinning not being formed [52, 53].

This study has provided a quantitative assessment of many deformation mechanisms in just one HEA system. The noticeable change of microstructure seen from

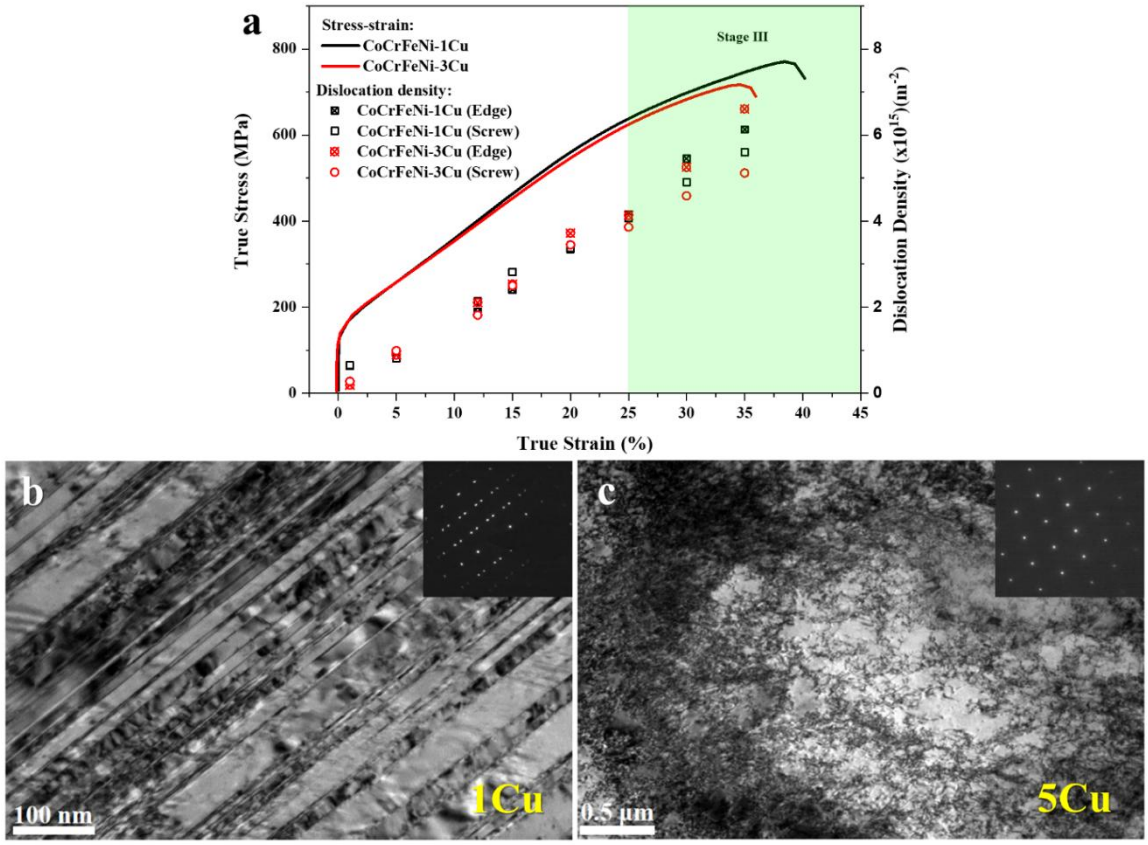


Figure 11. (a) Dislocation density of CoCrFeNi-1Cu and CoCrFeNi-3Cu, with TEM images of (b) CoCrFeNi-1Cu showing twinnings and (c) CoCrFeNi-5Cu showing dislocation forests. Both images were taken near the end of the stress-strain curves in Figure 9.

Table 3. Slopes of the linear regression from the modified Williamson-Hall plot and dislocation densities of CoCrFeNi-1Cu and CoCrFeNi-3Cu at several strain levels, obtained from the modified Williamson-Hall peak broadening analysis.

True Strain (%)	Slope ($\times 10^{-4}$)				Dislocation density ($\times 10^{15}$) (m^{-2})			
	CoCrFeNi-1Cu		CoCrFeNi-3Cu		CoCrFeNi-1Cu		CoCrFeNi-3Cu	
	Edge	Screw	Edge	Screw	Edge	Screw	Edge	Screw
1	0.117	0.121	0.035	0.051	0.628	0.653	0.187	0.276
5	0.158	0.150	0.166	0.184	0.849	0.808	0.890	0.989
12	0.353	0.399	0.393	0.339	1.891	2.139	2.104	1.816
15	0.449	0.526	0.474	0.467	2.407	2.818	2.533	2.500
20	0.626	0.631	0.696	0.646	3.346	3.372	3.719	3.450
25	0.778	0.761	0.775	0.724	4.156	4.065	4.131	3.861
30	1.021	0.919	0.985	0.861	5.449	4.906	5.250	4.588
35	1.149	1.050	1.238	0.959	6.128	5.599	6.603	5.118

the EDS map and the subsequent deformation mechanism seen from in situ tensile measurement by tuning the elemental composition have been revealed. The deformation mechanism of the sample that is observed in this study is similar to other HEAs with the same microstructural features. For example, the CoCrFeNi-1Cu with relatively smaller Cu clusters behaves similarly to CoCrFeMnNi at room temperature where we would see twinning formation at the last stage of deformation [11]. On the other hand, with the existence of relatively larger Cu clusters on CoCrFeNi-3Cu and CoCrFeNi-5Cu, the sample deforms by forming many dislocations, similar to nanoprecipitate-strengthened HEAs [49, 54].

Conclusion

To summarize, one alloy system was studied where little compositional change led to a plethora of microstructural and mechanistic change while the macroscopic stress-strain behavior was not changed drastically, observed by both direct and indirect methods which yielded consistent results. In situ diffraction and post-mortem characterizations were performed on CoCrFeNi-1Cu, CoCrFeNi-3Cu, and CoCrFeNi-5Cu. The ultimate tensile strength, elongation to failure, and stress at necking slightly decreased with increasing Cu content, while yield strength was maintained. Lattice strain evolution shows similar features where softer grain families {220} transfer the load to harder grain families {200}. Stacking fault formation was observed from the difference of lattice strains between {111} and {222} grains in CoCrFeNi-1Cu at the later stage of deformation. Stacking fault energy calculation on CoCrFeNi-1Cu suggests that twinnings are formed at the later stage of deformation, which was confirmed by the TEM image of post tensile loading sample.

Although the lattice strain evolution of CoCrFeNi-3Cu and CoCrFeNi-5Cu did not suggest stacking fault formation, the TEM study shows many dislocations were formed which causes these alloys to retain their strength and ductility, indicating that twinning alone might not necessarily lead to a high strength.

References

1. B. Cantor, I. Chang, P. Knight, and A. Vincent, Materials Science and Engineering: A, **375**: p. 213-218. (2004).
2. J.W. Yeh, S.K. Chen, S.J. Lin, J.Y. Gan, T.S. Chin, T.T. Shun, C.H. Tsau, and S.Y. Chang, Advanced engineering materials, **6**.(5): p. 299-303. (2004).
3. S. Chen, Z.H. Aitken, S. Pattamatta, Z. Wu, Z.G. Yu, D.J. Srolovitz, P.K. Liaw, and Y.-W. Zhang, Materials Today, **65**: p. 14-25. (2023).
4. C. Lee, G. Song, M.C. Gao, R. Feng, P. Chen, J. Brechtl, Y. Chen, K. An, W. Guo, and J.D. Poplawsky, Acta Materialia, **160**: p. 158-172. (2018).
5. Z. Li and D. Raabe, Jom, **69**.(11): p. 2099-2106. (2017).
6. J. Su, D. Raabe, and Z. Li, Acta Materialia, **163**: p. 40-54. (2019).
7. L. Liu, Y. Zhang, J. Han, X. Wang, W. Jiang, C.-T. Liu, Z. Zhang, and P.K. Liaw, Advanced Science, **8**.(23): p. 2100870. (2021).
8. Q. Ding, Y. Zhang, X. Chen, X. Fu, D. Chen, S. Chen, L. Gu, F. Wei, H. Bei, Y. Gao, M. Wen, J. Li, Z. Zhang, T. Zhu, R.O. Ritchie, and Q. Yu, Nature, **574**.(7777): p. 223-227. (2019).
9. Q. Ding, H. Bei, X. Wei, Y. Gao, and Z. Zhang, Materials Today Nano, **14**: p. 100110. (2021).
10. K.H. Lo, C.H. Shek, and J. Lai, Materials Science and Engineering: R: Reports, **65**.(4-6): p. 39-104. (2009).
11. G. Laplanche, A. Kostka, O.M. Horst, G. Eggeler, and E.P. George, Acta Materialia, **118**: p. 152-163. (2016).

12. Z. Wu, Y. Gao, and H. Bei, Acta Materialia, **120**: p. 108-119. (2016).

13. B. Gwalani, S. Gorsse, V. Soni, M. Carl, N. Ley, J. Smith, A.V. Ayyagari, Y. Zheng, M. Young, R.S. Mishra, and R. Banerjee, Materialia, **6**: p. 100282. (2019).

14. G.A. Salishchev, M.A. Tikhonovsky, D.G. Shaysultanov, N.D. Stepanov, A.V. Kuznetsov, I.V. Kolodiy, A.S. Tortika, and O.N. Senkov, Journal of Alloys and Compounds, **591**: p. 11-21. (2014).

15. M.C. Oh, A. Sharma, H. Lee, and B. Ahn, Intermetallics, **139**: p. 107369. (2021).

16. Z.G. Zhu, K.H. Ma, Q. Wang, and C.H. Shek, Intermetallics, **79**: p. 1-11. (2016).

17. J. Lu, B. Wang, X. Qiu, Z. Peng, and M. Ma, Surface and Coatings Technology, **328**: p. 313-318. (2017).

18. C.-M. Lin and H.-L. Tsai, Journal of Alloys and Compounds, **489**.(1): p. 30-35. (2010).

19. L. Jiang, Y.J. Hu, K. Sun, P. Xiu, M. Song, Y. Zhang, W.L. Boldman, M.L. Crespillo, P.D. Rack, and L. Qi, Advanced Materials, **32**.(39): p. 2002652. (2020).

20. B. Kombaiah, Y. Zhou, K. Jin, A. Manzoor, J.D. Poplawsky, J.A. Aguiar, H. Bei, D.S. Aidhy, P.D. Edmondson, and Y. Zhang, ACS Applied Materials & Interfaces. (2023).

21. Y. Zhang, Y.N. Osetsky, and W.J. Weber, Chemical Reviews, **122**.(1): p. 789-829. (2021).

22. S. Mukanov, P. Loginov, A. Fedotov, M. Bychkova, M. Antonyuk, and E. Levashov, Materials, **16**.(3): p. 1178. (2023).

23. T.G. Lach, C.M. Silva, Y. Zhou, W.L. Boldman, P.D. Rack, W.J. Weber, and Y. Zhang, npj Materials Degradation, **6**.(1): p. 60. (2022).

24. K.N. Campo, C.C. de Freitas, L. Fanton, and R. Caram, Journal of Materials Science & Technology, **52**: p. 207-217. (2020).

25. C.C. de Freitas, R. Caram, and K.N. Campo, Intermetallics, **150**: p. 107682. (2022).

26. Ł. Rogal, Materials and Design, **119**: p. 406-416. (2017).

27. Y. Qi, T. He, and M. Feng, Journal of Applied Physics, **129**.(19): p. 195104. (2021).

28. S. Nam, J.Y. Hwang, J. Jeon, J. Park, D. Bae, M.J. Kim, J.-H. Kim, and H. Choi, Journal of Materials Research, **34**.(5): p. 720-731. (2019).

29. S. San, Y. Tong, H. Bei, B. Kombaiah, Y. Zhang, and W.-Y. Ching, Materials & Design, **209**: p. 110071. (2021).

30. K. An, Y. Chen, and A.D. Stoica, MRS Bulletin, **44**.(11): p. 878-885. (2019).

31. K. An, H.D. Skorpenske, A.D. Stoica, D. Ma, X.-L. Wang, and E. Cakmak, Metallurgical and Materials Transactions A, **42**.(1): p. 95-99. (2011).

32. K. An, ORNL Report No. ORNL-TM-2012-621. (2012).

33. M. Frank, Y. Chen, S. Nene, S. Sinha, K. Liu, K. An, and R. Mishra, Materials Today Communications, **23**: p. 100858. (2020).

34. W. Woo, J.S. Jeong, D.K. Kim, C.M. Lee, S.H. Choi, J.Y. Suh, S.Y. Lee, S. Harjo, and T. Kawasaki, Scientific Reports, **10**.(1): p. 1350. (2020).

35. Z. Wang, A.D. Stoica, D. Ma, and A.M. Beese, Materials Science and Engineering: A, **674**: p. 406-412. (2016).

36. S. Harjo, Y. Tomota, P. Lukáš, D. Neov, M. Vrana, P. Mikula, and M. Ono, Acta materialia, **49**.(13): p. 2471-2479. (2001).

37. T. Ungár, I. Dragomir, Á. Révész, and A. Borbély, Journal of applied crystallography, **32**.(5): p. 992-1002. (1999).

38. W. Woo, T. Ungár, Z. Feng, E. Kenik, and B. Clausen, Metallurgical and Materials Transactions A, **41**: p. 1210-1216. (2010).

39. A. Borbély, J. Dragomir-Cernatescu, G. Ribárik, and T. Ungár, Journal of applied crystallography, **36**.(1): p. 160-162. (2003).

40. W. Woo, M. Naeem, J.-S. Jeong, C.-M. Lee, S. Harjo, T. Kawasaki, H. He, and X.-L. Wang, Materials Science and Engineering: A, **781**: p. 139224. (2020).

41. W. Zhang, Y. Gao, Z. Feng, X. Wang, S. Zhang, L. Huang, Z. Huang, and L. Jiang, Acta Materialia, **194**: p. 378-386. (2020).

42. R. Blondé, E. Jimenez-Melero, L. Zhao, J. Wright, E. Brück, S. Van der Zwaag, and N. Van Dijk, Acta Materialia, **60**.(2): p. 565-577. (2012).

43. B. Cai, B. Liu, S. Kabra, Y. Wang, K. Yan, P.D. Lee, and Y. Liu, Acta Materialia, **127**: p. 471-480. (2017).

44. K. Yan, K.-D. Liss, I.B. Timokhina, and E.V. Pereloma, Materials Science and Engineering: A, **662**: p. 185-197. (2016).

45. Y. Wang, B. Liu, K. Yan, M. Wang, S. Kabra, Y.-L. Chiu, D. Dye, P.D. Lee, Y. Liu, and B. Cai, Acta Materialia, **154**: p. 79-89. (2018).

46. M. Frank, S.S. Nene, Y. Chen, B. Gwalani, E.J. Kautz, A. Devaraj, K. An, and R.S. Mishra, Scientific Reports, **10**.(1): p. 22263. (2020).

47. K. Yamanaka, M. Mori, S. Sato, and A. Chiba, Scientific Reports, **7**.(1): p. 10808. (2017).

48. M. Frank, S.S. Nene, Y. Chen, S. Thapliyal, S. Shukla, K. Liu, S. Sinha, T. Wang, M.J. Frost, K. An, and R.S. Mishra, Applied Physics Letters, **119**.(8). (2021).

49. L. Fan, T. Yang, Y. Zhao, J. Luan, G. Zhou, H. Wang, Z. Jiao, and C.-T. Liu, Nature Communications, **11**.(1): p. 6240. (2020).

50. W. Wu, M. Song, S. Ni, J. Wang, Y. Liu, B. Liu, and X. Liao, Scientific reports, **7**.(1): p. 46720. (2017).

51. A. Verma, P. Tarate, A.C. Abhyankar, M.R. Mohape, D.S. Gowtam, V.P. Deshmukh, and T. Shanmugasundaram, Scripta Materialia, **161**: p. 28-31. (2019).

52. M. Vronka, M. Karlik, J. Vesely, J. Manak, and O. Heczko, Journal of materials science, **54**.(8): p. 6586-6593. (2019).

53. S. Stappert, B. Rellinghaus, M. Acet, and E. Wassermann, The European Physical Journal D-Atomic, Molecular, Optical and Plasma Physics, **24**: p. 351-354. (2003).

54. K. Ming, X. Bi, and J. Wang, International Journal of Plasticity, **100**: p. 177-191. (2018).

CHAPTER III

TANGENT MODULI AND SUCCESSIVE HARDENING MECHANISMS: QUANTIFICATION FROM IN SITU NEUTRON DIFFRACTION AND DUCTILITY IMPROVEMENT OF NANOPRECIPITATION-STRENGTHENED HEAS

This chapter was published in Materials Science and Engineering: A by Lia Amalia, Zongyang Lyu, Xuesong Fan, Ke An, Yan Chen, Dunji Yu, James Burns, Kangkang Wen, Baoru Sun, Tongde Shen, Peter K. Liaw, and Yanfei Gao:

Lia Amalia, Zongyang Lyu, Xuesong Fan, Ke An, Yan Chen, Dunji Yu, James Burns, Kangkang Wen, Baoru Sun, Tongde Shen, Peter K. Liaw, and Yanfei Gao. "Tangent moduli and successive hardening mechanisms: Quantification from in situ neutron diffraction and ductility improvement of nanoprecipitation-strengthened HEAs." Materials Science and Engineering: A (2026): 150187.

This chapter is adapted from the published article and has been reformatted to conform to the formatting requirements of the University of Tennessee, Knoxville, and to fit the structure of this dissertation. The author contributions are retained as reported in the published article using the CRediT author contribution taxonomy. Lia Amalia contributed to conceptualization, data curation, formal analysis, investigation, methodology, resources, software, supervision, validation, visualization, writing–original draft, and writing–review and editing. Zongyang Lyu, Xuesong Fan, Ke An, Yan Chen, Dunji Yu, James Burns, Kangkang Wen, and Baoru Sun contributed to conceptualization, data curation, formal analysis, investigation, methodology, resources, software, supervision, validation, visualization, writing–original draft, and writing–review and editing. Tongde Shen, Peter K. Liaw, and Yanfei Gao contributed to conceptualization, data curation, formal analysis, funding acquisition, investigation, methodology, project administration, resources, software, supervision, validation, visualization, writing–original draft, and writing–review and editing.

Abstract

According to the Considère criterion for necking, the improvement of tensile ductility can be accomplished by designing a number of hardening mechanisms that operate successively and thus sustain a continuously increasing work hardening rate (or at least not decreasing rapidly). This work proposes a novel mechanics approach to extract the tangent moduli of each constituent phase and diffraction-selected grain families from in situ neutron diffraction measurements, thus permitting a quantitative assessment of hardening-rate contributions from each individual mechanism. This methodology has been applied to a nanoprecipitation-strengthened high entropy alloy, $(FeCoNi)_{86}Al_7Ti_7$ (at.%) alloy with $L1_2$ precipitates (size of ~100-200 nm), which gives an ultimate tensile strength of ~1.2 GPa and a failure strain of ~38.5%. It is found that, beyond the classic load sharing between two phases in the early stage, some grain families in the $L1_2$ precipitates subsequently exhibit elevated hardening, followed by the continued dislocation hardening in the matrix phase before the onset of necking. The yielding and hardening-rate sequences can be extracted and compared to the successive load sharing mechanisms. The quantification of tangent moduli and successive hardening mechanisms from in situ neutron diffraction contrast sharply with prior qualitative studies in literature (e.g., post-mortem or interrupted characterizations). A new design strategy is proposed, based on maximizing differences in all tangent moduli, for the ductility improvement of metallic materials with complex microstructures.

Introduction

Precipitation strengthening has been widely studied and used in steels [1-4], Mg alloys [5-7], and others. However, in most conventional metallic materials, the precipitates increase the strengths of the materials at the expense of the ductility. Unlike the traditional steels and alloys which are based on one principal element, the multicomponent high entropy alloys (HEAs) [8,9] could greatly widen the alloy design space for developing novel precipitates and invoking novel deformation mechanisms, all of which have the potential of accomplishing the strength-ductility synergy [10-15]. The incorporation of precipitates or second phases of various sizes can easily improve the HEA strength, but the work hardening rate is oftentimes reduced or cannot keep up with the strength increase, which results into earlier necking according to the Considère criterion [16-20]. For example, the extremely hard σ and μ intermetallic phases were created by adding Mo into the CoCrFeNi HEA by Liu et al. [17]. The resulting alloy showed a yield strength of 816 MPa and tensile strength of 1.2 GPa with a ductility of ~19%. The FeCoNi alloy as the base alloy was added with oxide dispersion [18] and $L1_2$ precipitations [19,20] to achieve as high as five times yield strengths compared with the FCC single-phase base alloy while the ductility had an obvious reduction. Cu clusters have been developed by Gwalani et al. [21] to strengthen the $Al_{0.3}Cu_{0.3}Ti_{0.2}$CoCrFeNi HEA which exhibited yield and ultimate tensile strengths of 820 MPa and 1100 MPa, respectively, with a moderate ductility of ~ 20%. Amalia et al. [22] showed the doping of CoCrFeNi HEA with a small amount of Cu retains the solid solution and twinning mechanism, while a larger amount led to Cu clusters and a change of deformation mechanisms. Nevertheless, the macroscopic stress-strain

curves were indistinguishable even with different doping amounts. B2 ordered precipitates have also been used for strengthening HEAs in the AlCoCrFeNi HEA system [23] which could double the yield strengths but again with a corresponding ductility reduction.

The Considère necking condition gives $\partial\sigma/\partial\varepsilon = \sigma$, i.e., the material tangent (i.e., work hardening rate) from stress σ and strain ε being equal to the stress. The most effective strategy to improve tensile ductility is to sustain a high hardening rate from a number of deformation mechanisms in a successive manner. For example, a spatially hierarchical microstructure can have multiple hardening mechanisms that are operated at different locations at different strain levels – independent mechanisms are sequential in time [24]. In two phase materials, there could be competition and/or cooperation among different deformation mechanisms. In a duplex Mg-Li alloy [7], the initial yielding of the BCC β-Li phase was followed by the basal slip in the HCP α-Mg phase, and then by the elevated hardening in β-Li. The soft β-Li phase relaxed the Mises constraint due to the limited slip systems in the HCP phase, and the overall high stress helped activate the activation of no-basal slips in the later stage of the deformation. In an austenite-ferrite duplex steel [25], the initially soft austenite and hard ferrite phases triggered a hetero-deformation induced hardening, thus subsequently leading to a strength reversal of these two phases. Yang et al. [15] proposed a strategy to break the strength-ductility trade-off by introducing high-density ductile multicomponent intermetallic nanoparticles (MCINPs) in the FeCoNi HEA by adding Al and Ti, which showed superior tensile strength of ~1500 MPa and ductility of ~50% at room temperature. The excellent ductility in such precipitation-strengthened HEAs was attributed to triggering a distinctive multistage work-

hardening behavior, resulting from pronounced dislocation activities and deformation-induced microbands.

Despite many recent successes in utilizing successive hardening mechanisms for ductility improvements, a major challenge lies on how to quantify the contributions from each mechanism to the overall hardening rate. Literature works predominately utilize post-mortem transmission electron microscopy (TEM) and other characterization tools. While some insights on the competition and cooperation among various mechanisms can be obtained, a real-time and quantitative understanding of continuous deformation mechanisms is oftentimes lacking. This is because the post-mortem measurements are usually conducted within limited local areas and cannot quantitatively provide the load partitioning of various phases and grain orientations. Furthermore, the ability to continuously track activations and evolutions of deformation mechanisms can only be performed on multiple interrupted tests. A unique approach that can mitigate the above challenges is the in situ neutron diffraction technique. Owing to the deep penetration capability, neutron beams can probe the collective behavior of all grains and phases and therefore can provide a quantitative understanding and demarcation of multiple deformation mechanisms. However, a mechanistic connection between interpretations of such data and the material tangent does not easily transpire. For example, neutron diffraction data from the duplex Mg-Li alloy [7] were interpreted by a yielding sequence from the yield strain of the constituent phases/grain families, while those from the austenite-ferrite duplex steel [25] by a strength sequence of the two phases only. None of

these works has a clear reference to the material tangent that is central to the Considère condition.

Based on the above gap studies, the main hypothesis of this work is to develop a mechanics approach on how to extract the tangent moduli of different phases and grain families from in situ neutron diffraction measurements. The analysis procedure is employed to a multicomponent nanoprecipitation strengthened HEA of $(FeCoNi)_{86}Al_7Ti_7$ (at.%), as denoted as Al7Ti7-this-work, similar to Yang et al. [15] but with slightly different microstructural features. It is fabricated here with a sufficiently large sample size for in situ neutron diffraction measurements under tension. Multistage work hardening behavior is observed during tension, which are now interpreted by the evolution of various tangent moduli. Consequently, it is found that the early stage corresponds to a classic load-sharing behavior in two-phase materials, followed by complex hardening-rate sequences in precipitate and matrix phases. The microband-induced plasticity (MBIP) confirmed by TEM studies in Yang et al. [15] was not observed here, primarily due to much larger precipitate size in our work. Instead, the tangent modulus study reveals how successive hardening mechanisms help delay the necking occurrence. As will be shown by the details later, this study could fill the knowledge gap of the deformation mechanisms of the MCINPs strengthened HEAs and help to provide a better understanding of ductility improvement, which will be beneficial to further design of high-performance alloys.

Experimental Procedures

The $(FeCoNi)_{86}Al_7Ti_7$ alloy (at.%) was prepared with pure elements (>99.9% wt.%) by vacuum induction melting and casting. The alloy ingot was homogenized at

1200 °C for 2 h followed by water-quenching. Then cold rolling was conducted with a thickness reduction of ~65%. After that, the alloy ingot was heat treated at 1150 °C for ~1.5 min for recrystallization. The final heat treatment to grow the precipitates was by annealing at 780 °C for 4 h, followed by water-quenching. Dog-bone bar samples were machined with the dimensions of Φ6.35 mm × 13 mm in the gauge section for the tensile test.

TEM was performed on a ZEISS LIBRA 200 HT FE MC (Institute of Advanced Materials and Manufacturing, University of Tennessee). The TEM samples were prepared by twin-jet polishing with an electrolyte consisting of 95% ethanol and 5% perchloric acid in a volume fraction under −40 °C and voltage of 30 V.

Atom Probe Tomography (APT) was conducted for atomic-scale compositional analysis. The needle-shaped samples were extracted from the polished samples using dual-beam SEM and focused ion-beam instruments using in-situ lift-out protocol. APT was conducted using Cameca Instrument LEAP 4000 XHR Local Electrode Atom Probe at Center for Nanophase Materials Sciences (CNMS), Oak Ridge National Laboratory (ORNL).

The uninterrupted and continuous in situ neutron diffraction measurements were conducted with an MTS load frame at the VULCAN Engineering Materials Diffractometer [26,27], the Spallation Neutron Source (SNS), ORNL. A slower strain rate of 10^{-4} /s was used to have ample time for data acquisitions, as opposed to ex situ tensile test which used 10^{-3} /s as the strain rate. As per the beamline facility requirement, the tension dog-bone bar sample has gauge section dimension of Φ6.35 mm × 13 mm. Diffraction data were

analyzed using the VULCAN Data Reduction and Interactive Visualization software (VDRIVE) [28]. The lattice strain of a particular {hkl} plane is determined by:

$$\varepsilon_{hkl} = \frac{d_{hkl} - d_{hkl}^0}{d_{hkl}^0}, \quad (1)$$

where d_{hkl}^0 and d_{hkl} are the lattice *d*-spacing in stress-free condition and the lattice *d*-spacing during loading condition, respectively. Loosely speaking, grains with their <hkl> orientations aligning with the diffraction vector will contribute to diffraction signals for the calculations in Eq. (1). Both matrix and precipitates are cubic crystals so that we simply denote the above grains as the {hkl} grain family.

Diffraction data were divided into continuous, shorter, and equal time interval dataset, which then averaged to produce a single representative diffraction pattern per time interval to allow time-resolved analysis (data binning). In this experiment, the bin time was 117 seconds for a dataset of 3611 seconds which produced 31 datasets. Full-pattern Rietveld refinements [29] were conducted on each dataset to obtain the lattice parameters of FCC and $L1_2$ using GSAS software [30]. The phase strain of each phase was calculated using $(a - a_0)/a_0$, with a_0 being the lattice parameter at unloaded state and *a* is the lattice parameter at each dataset [31,32].

Experimental Results

As shown in Figure. 12(a), the neutron diffraction patterns indicate that the Al_7Ti_7-this-work contains FCC and $L1_2$ phases. The relative intensities of diffraction peaks in loading direction (LD) are similar to those in transversal direction (TD). The diffraction intensity of a certain *hkl* peak is proportional to the volume fraction of the {hkl} grain family [33]. In this way, the Al_7Ti_7-this-work had similar microstructure in the LD and TD.

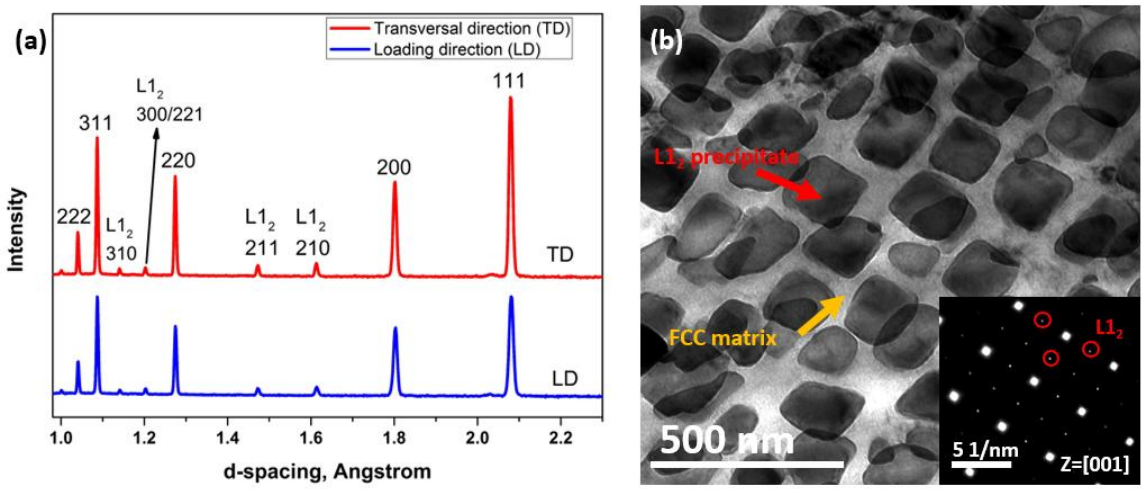


Figure 12. Microstructural characterization of the undeformed Al_7Ti_7-this-work by (a) neutron diffraction and (b) bright-field transmission electron microscopy (TEM) along the {001} zone axis. Note that the FCC peaks overlap with the $L1_2$ peaks in (a).

Full profile Rietveld analysis revealed FCC and $L1_2$ phases having lattice constants of 3.602639 Å and 3.608693 Å, respectively. The lattice mismatch, calculated from $2\frac{a_{L12}-a_{FCC}}{a_{L12}+a_{FCC}}$ is 0.168%. Rietveld refinement also provides a weight fraction of each phase, which are 60.138% and 39.865% for FCC and $L1_2$ phase, respectively. The microstructure of the Al_7Ti_7-this-work by TEM is shown in Figure 12(b). Cuboidal $L1_2$ precipitates with the size ~ 100-200 nm are generated from the FCC matrix in the Al_7Ti_7-this-work. The $L1_2$ particle size is larger than that in [15], where their particle size is ~30-50 nm.

Figure 13 shows the atom maps, precipitate shape, and proximity histograms of $(FeCoNi)_{86}Al_7Ti_7$ in undeformed and deformed states. The L_{12} precipitate is rich in Ni, Co, and Ti, and depleted in Al and Fe, while the FCC matrix is rich in Fe, Co, and Ni and depleted in Al and Ti. The chemical compositions of the FCC matrix and $L1_2$ precipitate are $Fe_{40.6}Co_{30.426}Ni_{20.762}Al_{4.462}Ti_{2.55}$ (at%) and $Fe_{7.837}Co_{22.436}Ni_{43.633}Al_{9.989}Ti_{15.886}$ (at%), respectively, from Figure 13(c). The chemical composition from APT listed here excludes traces of Cu, Mn, and V with the total composition of 0.196% (undeformed) and 0.244% (deformed). Yang et. al identified the $L1_2$ precipitates as $(Ni_{43.3}Co_{23.7}Fe_8)_3(Ti_{14.4}Al_{8.6}Fe_2)$ using first-principles calculations [15]. The composition of $L1_2$ precipitates produced in our work is very close to the one reported by Yang et al. with the minor difference coming from Al and Fe compositions. The minor difference from Al and Fe composition does not change the $L1_2$ composition because with Ni and Co occupying the A sublattice with 66.069% and Ti, Al, and Fe occupying the B sublattice with 33.712%. The A_3B stoichiometry is still satisfied. The Ti/Al ratio from our precipitate is around 1.59 (undeformed) to 1.63 (deformed), which is very close to 1.67 as reported by Yang et al.

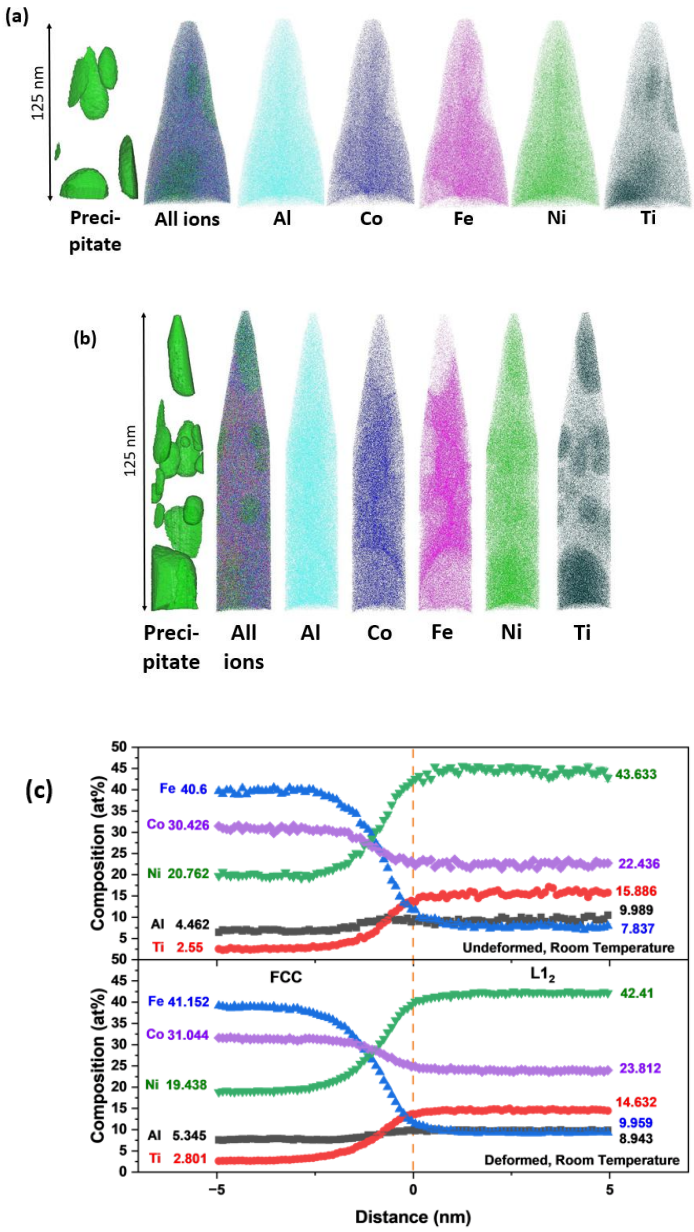


Figure 13. Atom Probe Tomography (APT) reconstruction of needle samples, showing the isoconcentration surface of the samples taken from (a) undeformed state and (b) deformed state (after the tensile fracture). (c) The proxigrams show clear distinction between the FCC matrix and the $L1_2$ precipitates.

[15]. The higher Ti/Al ratio was chosen to reduce environmental embrittlement and promote higher work-hardening due to dislocation cross-slip generation. There is no significant difference of composition from undeformed and deformed state, which confirms that the precipitates are chemically stable upon room temperature mechanical loading.

The studied Al_7Ti_7-this-work was mechanically tested ex situ and has the yield strength and ultimate tensile strength of 893 MPa and 1205 MPa, respectively, with a ductility of ~38.5%, as shown in Figure 14(a). The engineering stress-strain curves of the $(FeCoNi)_{86}Al_8Ti_6$ and $(FeCoNi)_{86}Al_7Ti_7$ from [15], denoted as Al_8Ti_6-Yang and Al_7Ti_7-Yang, were also plotted in Figure 14(a) for comparison. The studied alloy shows lower ultimate tensile strength than that of Al8Ti6-Yang (~ 1267 MPa) and Al_7Ti_7-Yang (~ 1500 MPa). The ductility of the Al_7Ti_7-this-work is higher than that of the Al_8Ti_6-Yang (~ 33.6%), but inferior to that of the Al_7Ti_7-Yang (~ 50%). To further understand the mechanical behavior, the work hardening rate of the Al_7Ti_7-this-work during tension is plotted in Figure 14(b). The Al_7Ti_7-this-work shows a multistage work hardening behavior during tension and there could be three stages to describe the whole deformation behavior. Stage I has a fast decrease of work hardening rate which is typical for deformation immediate after the macroscopic yield point [34]. In Stage II, the decrease of the work hardening rate slows down and turns into an increase part followed by a continuous decrease of the work hardening rate. The decrease of work hardening rate in Stage III tends to be slower than that in the later part of Stage II. It should be noted that the transition from

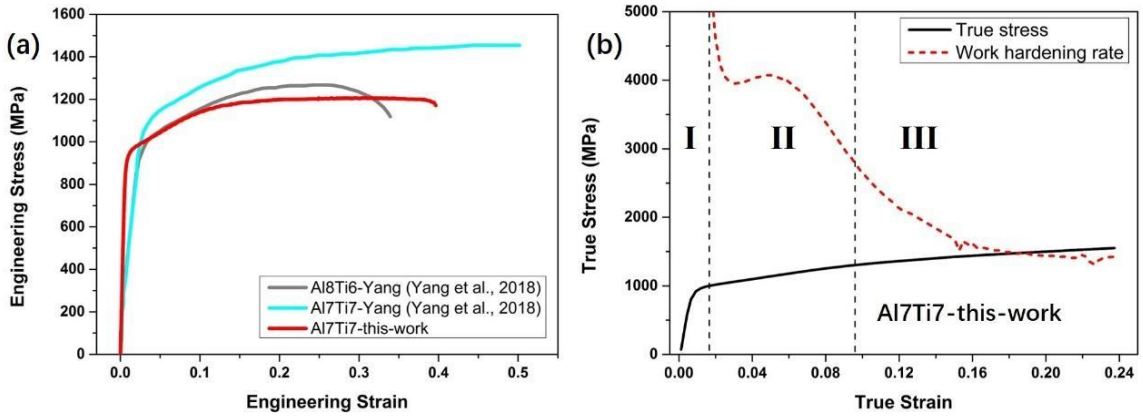


Figure 14. (a) Engineering stress-strain curves of three materials, including Al7Ti7-this-work obtained from ex situ tensile test, Al8Ti6-Yang, and Al7Ti7-Yang (the latter two obtained from [15]), and (b) the work hardening behavior of the Al7Ti7-this-work under uniaxial tension.

Stage II to Stage III may not be clear from this plot, but this will be further illustrated clearly by the lattice strain evolution in Figure 15.

The lattice strain evolutions of the FCC and $L1_2$ phases with different grain families are plotted in Figure 15(a) with two representative TEM images at the beginning and end of the tensile test in Figs. 15(b) and 4(c), respectively. It should be noted that the FCC fundamental reflections (i.e., {111}, {200}, {220}, {222}, and {311}) are convoluted with the ordered $L1_2$ reflections due to their shared crystallographic structure. For $L1_2$ phase, {300} and {221} reflections are coincidental because of the same d-spacing as calculated from $\sqrt{h^2+k^2+l^2}$. Stage I contains the whole linear increasing part of the lattice strain and the first slope change (oftentimes called "bending" or "splitting") of each lattice strain curve. In this stage, the {200} lattice strain shows an obvious rightward turn (i.e., a smaller slope), which means the {200} grain family tends to share more load, meaning they are hard grains compared to the other grain families. At the same time, the {111} and {220} have upward trends (i.e., a larger slope), meaning that these grain families deform plastically. The slope change is a result of the successive yielding or hardening of various grain families and/or various phases, as will be discussed in the next section. Thus, in this work, successive hardening is defined as sequential contribution of each phase to the overall hardening response. During the transition from Stage I to II, the {210}, {211} and {310} grain families of $L1_2$ phase start to take more load sharing from the matrix with a dramatic right bend of the lattice strain. Correspondingly, the {200} and {311} lattice strain curves tend to show upward turns in Stage II. From lattice strain evolution of {200} grain family of FCC phase, the transition from Stage II to Stage III can be easily delineated. In

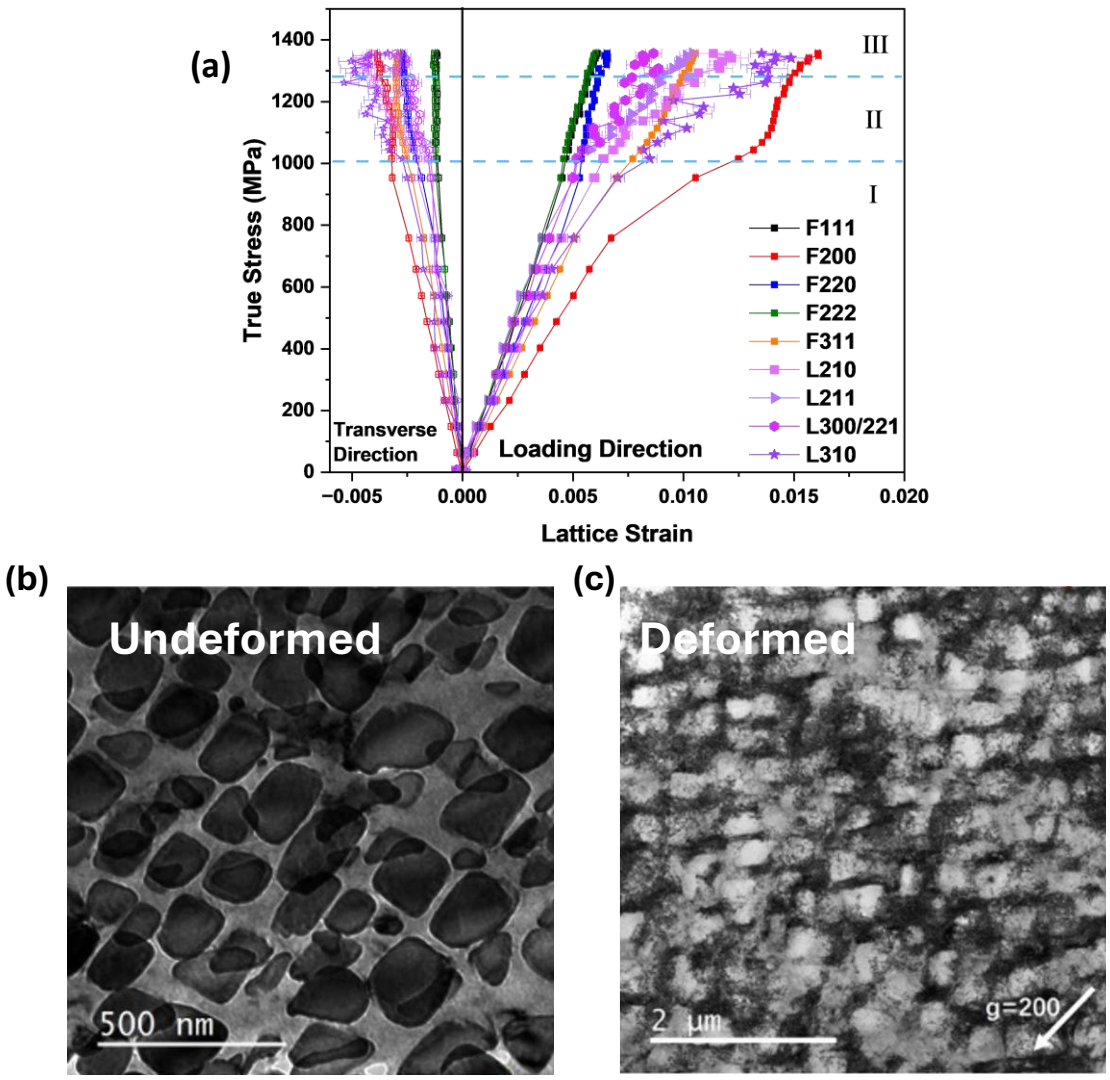


Figure 15. (a) Lattice strain evolutions of different grain families in Al_7Ti_7-this-work along loading direction. (b) and (c) Representative TEM images of the undeformed and fractured Al_7Ti_7-this-work.

the middle of Stage III, surprisingly, the {200} has a second right turn, which means that the {200} grain family starts to bear the load-carrying capacity again. The transition of the lattice strain slopes in both FCC and $L1_2$ grains indicates intergranular stress partitioning occurring in both the matrix and precipitates [7,34]. The stress partitioning arises from the contrast in the mechanical strength between the soft FCC matrix and the hard $L1_2$ precipitates as indicated in Figure 20(b). After the macroscopic yielding, the plastic deformation localized in the FCC matrix first while the $L1_2$ phase remains largely elastic and acts as the load-bearing particles. Similar load partitioning between soft and hard phase have been documented by both in situ neutron diffraction and microscopy study [43, 44].

The Mechanics Model for Tangent Moduli

The lattice strain bending/splitting is usually interpreted by the yielding sequence [35,36], as illustrated in Figure 16. The deformation field of a polycrystal can be approximated by the Taylor iso-strain model, in which all grains or constituents experience the same strain fields as the applied one. Two materials have different yield strains ($\varepsilon_Y = \sigma_Y / E$), and the stress of the composite can be calculated from the rule of mixture of stresses on these two materials. Because of the iso-strain assumption ($\varepsilon_A = \varepsilon_B = \varepsilon$), the one with lower yield strain, i.e., $\varepsilon_Y^A < \varepsilon_Y^B$ in the drawing here, will yield first and the corresponding lattice strain shows upward bending/splitting in Figure 16(c). The corresponding tangent moduli, $E_A^* = \partial\sigma_A / \partial\varepsilon$ and $E_B^* = \partial\sigma_B / \partial\varepsilon$, are shown in Figure 16(d). Indeed, most diffraction analyses argue that the upward splitting indicates a “soft grain/phase” while the rightward splitting indicates a “hard grain/phase” (e.g., [7]). It

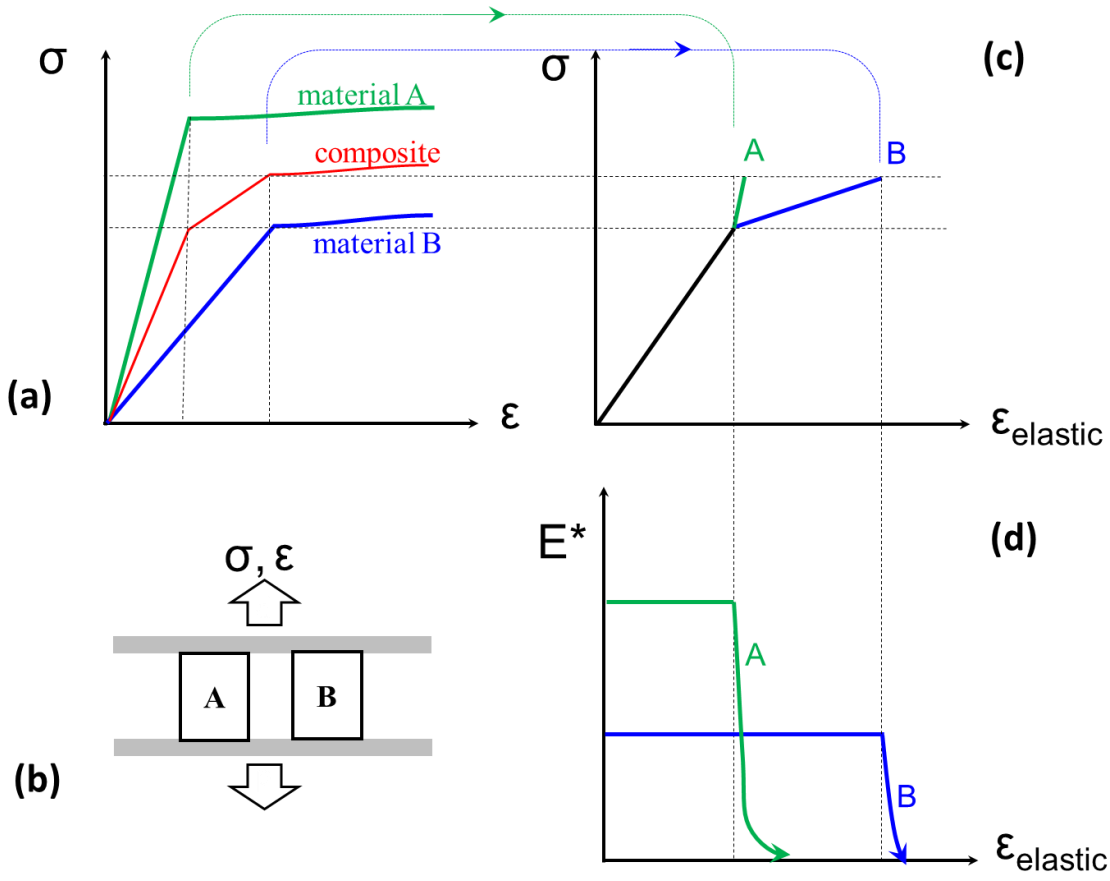


Figure 16. Schematic illustration of how the yielding sequence governs the lattice strain splitting. (a) The stress-strain curves showing the initial yield takes place for the material with low yield strain. (b) The Taylor iso-strain composite model. (c) The corresponding stress vs. elastic strain curves for the two constituents. (d) The corresponding evolution of material tangent.

should be pointed out that the so-called yielding sequence should indicate the sequence of ε_Y, but not the strength sequence (e.g., [25]).

In the same manner, it can be shown that different hardening rates can lead to a similar lattice strain splitting, as shown in Figure. 17. The material with a high hardening rate will display the rightward bending, while the one with no hardening will lead to perfectly upward bending. Clearly, both the yielding sequence in Figure 16(a) and the hardening-rate sequence in Figure 17(a) give essentially the same type of lattice strain splitting (i.e., Figure 16(b) and Figure 17(b) are identical). This is a many-to-one mapping problem. A question that naturally arises is that, with the lattice strains in Figure 15, what are the underlying deformation mechanisms. The distinguishing factor will be the difference in the tangent moduli of the constituents between Figure 16(d) and Figure 17(d).

Previous work has successfully calculated the hardening contribution of each phase [45, 46, 47], but the real-time hardening rate, i.e. the tangent modulus of each grain orientation of each phase has not been reported yet. Therefore, it is now imperative to develop a procedure to determine the tangent moduli from lattice strain data. Denote $E_{hkl,\alpha}$ and $E^{*}_{hkl,\alpha}$ as the elastic tangent and the instantaneous material tangent of the {hkl} grain family of the α-th phase. The lattice strains in Figure 15(a) are elastic ones, thus denoted as $\varepsilon^{el}_{hkl,\alpha}$. Under uniaxial tensile tests and assuming the Taylor iso-strain condition (i.e., the strain on any given grain family, $\varepsilon_{hkl,\alpha}$, is the same as the macroscopic strain, ε), we can write

$$E_{hkl,\alpha}=\frac{\partial\sigma_{hkl,\alpha}}{\partial\varepsilon^{el}_{hkl,\alpha}},\ E^{*}_{hkl,\alpha}=\frac{\partial\sigma_{hkl,\alpha}}{\partial\varepsilon_{hkl,\alpha}}=\frac{\partial\sigma_{hkl,\alpha}}{\partial\varepsilon}. \tag{2}$$

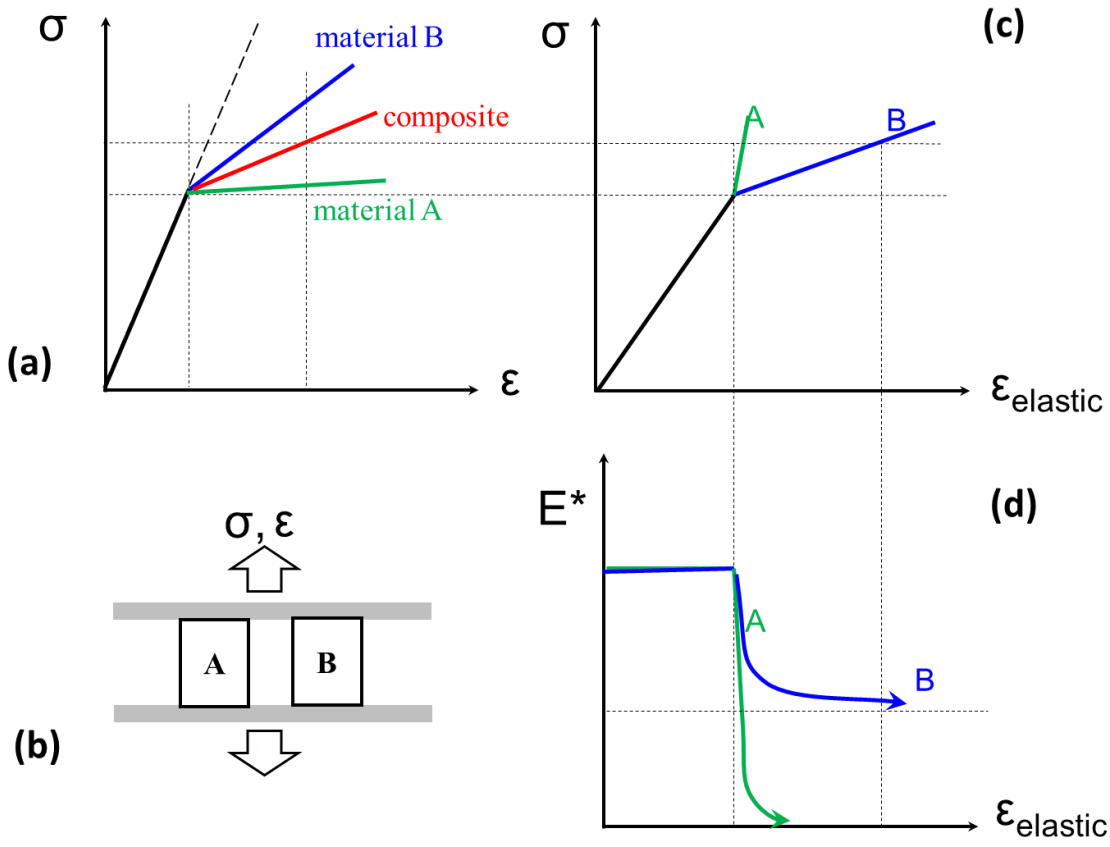


Figure 17. Schematic illustration of how different hardening rates govern the lattice strain splitting. (a) The stress-strain curves of each material and the composite. (b) The Taylor iso-strain composite model. (c) The corresponding stress vs. elastic strain curves for the two constituents. (d) The corresponding evolution of material tangent.

The rule of mixture gives the relationship between phase/grain stresses, $\sigma_{hkl,\alpha}$, and overall stress, σ, in the incremental form,

$$\Delta\sigma = \sum_{hkl,\alpha} f_{hkl,\alpha}\Delta\sigma_{hkl,\alpha} = \left(\sum_{hkl,\alpha} f_{hkl,\alpha} E^*_{hkl,\alpha} \right) \Delta\varepsilon = E^* \Delta\varepsilon \,, \tag{3}$$

where $f_{hkl,\alpha}$ is the corresponding volume fraction, and $E^* = \partial\sigma/\partial\varepsilon$ is the material tangent of the macroscopic stress-strain curve. It should be noted that each curve in Figure 15 presents $\sigma \sim \varepsilon^{el}_{hkl,\alpha}$ and thus gives $\partial\sigma/\partial\varepsilon^{el}_{hkl,\alpha}$. Lattice strain measurements in Figure 15, together with Eqs. (2) and (3), results into

$$\frac{\partial\sigma}{\partial\varepsilon^{el}_{hkl,\alpha}} = E^* \frac{\partial\varepsilon}{\partial\varepsilon^{el}_{hkl,\alpha}} = E^* \frac{E_{hkl,\alpha}}{E^*_{hkl,\alpha}} \,. \tag{4}$$

The procedure to determine $E^*_{hkl,\alpha}$ is listed in the following and is illustrated in Figure 18:

i. Data preparation
   a. From the macroscopic tensile test, obtain $\sigma \sim \varepsilon$ in the form of true stress and strain.
   b. From the in situ neutron diffraction tests, obtain lattice strains, $\sigma \sim \varepsilon^{el}_{hkl,\alpha}$, from the {hkl} grain family of the α-th phase.

ii. Calculate the following tangents
   a. Macroscopic material tangent, E^*, from the $\sigma \sim \varepsilon$ curve.
   b. Using the elastic constants and the crystallographic orientation {hkl}, calculate the directional modulus $E_{hkl,\alpha}$.
   c. From lattice strain results, calculate $\partial\sigma/\partial\varepsilon^{el}_{hkl,\alpha}$ (i.e., slopes in Figure 15).

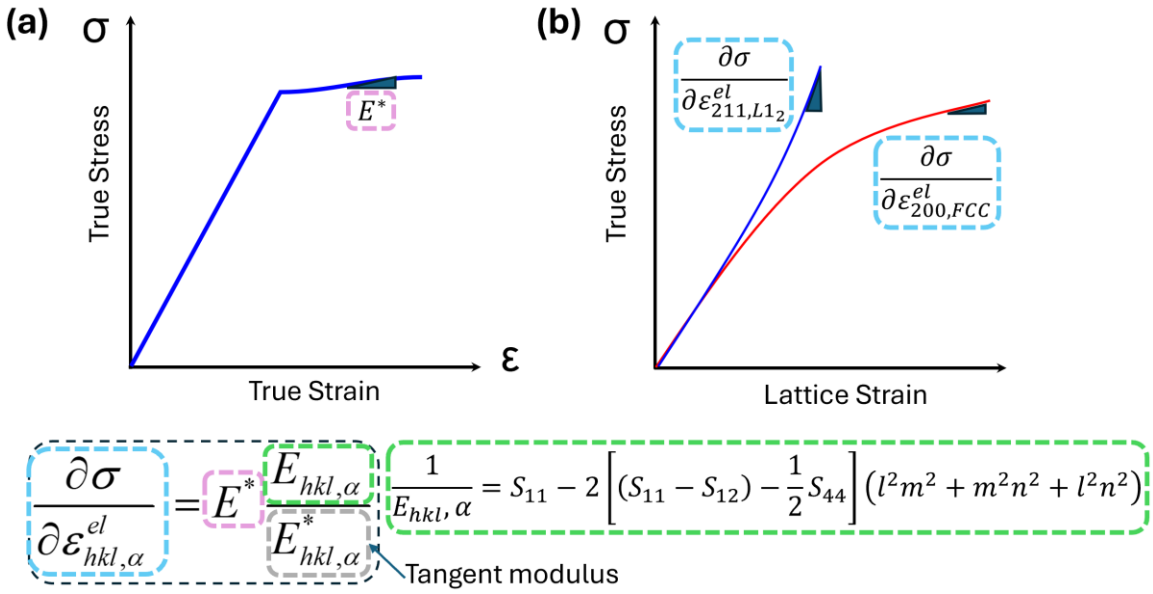


Figure 18. Illustration of data processing from (a) true stress versus true strain and (b) true stress versus lattice strain to obtain the tangent modulus.

iii. Obtain the individual material tangent, $E^{*}_{hkl,\alpha}$ from E^{*}, $E_{hkl,\alpha}$, and $\partial\sigma/\partial\varepsilon^{el}_{hkl,\alpha}$ as shown in Eq. (4).

The results can then be used to quantify the hardening contributions and reveal the sequence of hardening of various phases/grain families.

It should be noted that the volume fractions in Eq. (3) are not explicitly used in the above model. However, such information can be extracted from the Rietveld analysis, and therefore phase strains, $\varepsilon^{el}_{\alpha}$, and phase stresses, σ_{α}, can be obtained. Using the Taylor iso-strain assumption again can give us $\partial\sigma_{\alpha}/\partial\varepsilon$, as a supplement to $E^{*}_{hkl,\alpha}$, which will be discussed further in next section.

To complete the calculation of tangent modulus, the directional modulus, $E_{hkl,\alpha}$, is obtained from

$$\frac{1}{E_{hkl}} = S_{11} - 2\left[\left(S_{11} - S_{12}\right) - \tfrac{1}{2}S_{44}\right]\frac{h^2k^2 + k^2l^2 + l^2h^2}{\left(h^2 + k^2 + l^2\right)^2}. \tag{5}$$

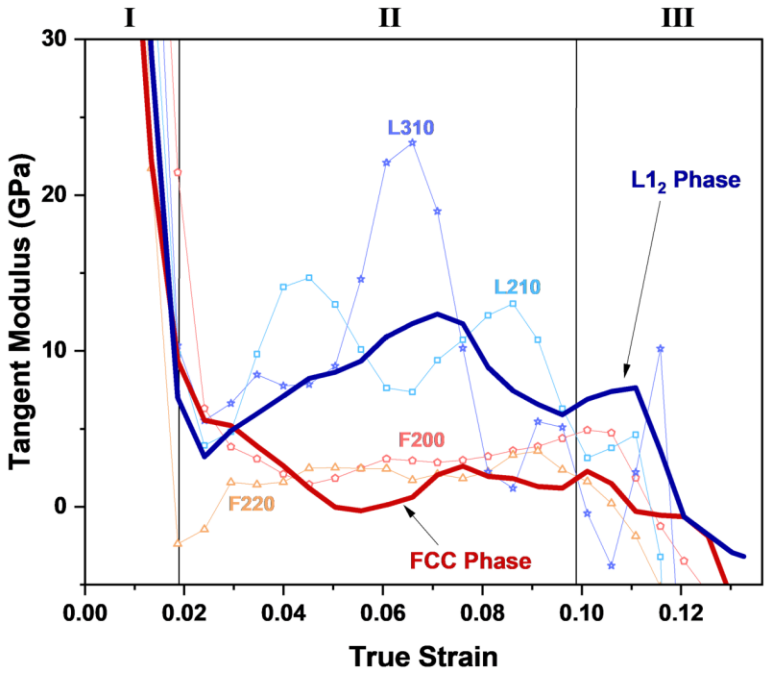
where S_{ij} is the contracted compliance tensor. The procedure to determine the compliance constants, known as the Kröner's self-consistent model, can be found in [37,38]. Since the FCC and $L1_2$ peaks overlap in the fundamental reflections (i.e., {111}, {200}, {220}, {222}, and {311}) and no obvious peak splitting during loading, the data obtained from the fundamental reflections were used to calculate the elastic constants for FCC phase. Results are presented in Table 4.

Discussions

Results in Figure 19 present the tangent modulus evolution of various grain families of each phase. In Stage I and the early stage of Stage II, the lattice strain evolution in Figure

Table 4. Calculated stiffness and compliance constants for the two phases.

	C_{11}	C_{12}	C_{44}	S_{11}	S_{12}	S_{44}
	GPa			GPa^{-1}		
FCC	197.421	117.186	82.465	0.009081	-0.003382	0.012126
$L1_2$	266.040	171.097	75.828	0.007570	-0.002963	0.013188



Tangent modulus	I	II	III
Precipitate Phase	↓	↗	→
Matrix Phase	↓	↘	↘

Figure 19. Tangent modulus evolution of three representative grain families of FCC phase and three representative grain families of $L1_2$ phase. The table below shows the schematic trends in the three deformation stages.

15(a) is quite monotonic and the extracted tangent moduli have small differences. Thus, the lattice strain splitting is primarily governed by the yielding sequence. That is, {310} and {200} are "hard grains" and {220} is the "soft grain" for the FCC phase, while {310} and {210} are "hard grains" for the $L1_2$ phase. The yield strain, as determined from strength-to-stiffness ratio, is inversely proportional to the product of Schmid factor (S_{hkl} under uniaxial test) and directional modulus E_{hkl} with a given <hkl> direction. For cubic materials with octahedral slip, it has been shown that <100> directions are "hard" and directions close to <110> and <111> are "soft" [35,36]. The lattice strain splitting sequence in Stage I of Figure 15(a) does agree with such a yield-strain analysis.

As the deformation proceeds into Stage II, the tangent moduli of $L1_2$ grain families increases, while those of FCC grain families continue to decrease. The calculation of phase tangent moduli from the Rietveld analysis will be presented in Figure 20. As explained in previous section, a smaller slope in the plot of $\sigma \sim \varepsilon^{el}_{hkl,\alpha}$ suggests a higher tangent modulus, $E^{*}_{hkl,\alpha}$, which are therefore "hard grains" for a different reason than the yield-strain analysis. Consequently, the lattice strain evolution in Figure 15(a) and the tangent moduli in Figure 19 suggest the following:

- The initial lattice-strain splitting is largely governed by a hard-grain indicator, $\frac{E_{100}}{S_{hkl}E_{hkl}}$. If this indicator is high, the corresponding grain family is "hard" as schematically shown in Figure 16.
- When all fundamental reflections (i.e., {111}, {200}, {220}, {222}, and {311} for FCC materials) exhibit noticeable bending, the deformation proceeds to full plastic stage and

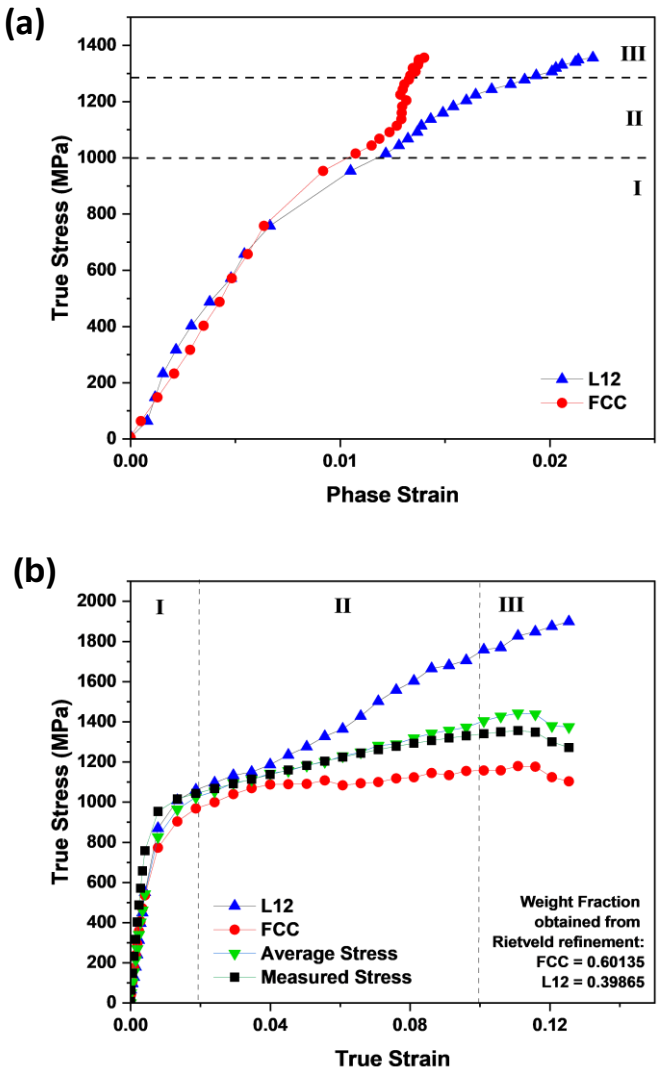


Figure 20. (a) Phase strain evolution of FCC and $L1_2$ phase versus true stress; (b) phase stresses of FCC and $L1_2$ phase with the calculated average stress compared to the measured bulk stress tested in situ during neutron diffraction data acquisition.

thereafter the lattice-strain splitting is primarily governed by the hardening-rate sequence as schematically shown in Figure 17.

Looking closely at the tangent modulus of each grain family, the hardening contribution of $L1_2$ phase during Stage II is directly observable where tangent moduli of $L1_2$ grain families are nearly one order of magnitude higher than those of FCC grain families. All grain families of FCC phase have similar tangent moduli. In contrast, the soft grains in $L1_2$ phase continue to decrease, but the hard grains in $L1_2$ phase exhibit an increase, which resembles the observations of phase-transformation-induced plasticity (TRIP) in metastable steels [34] but for completely different reasons. Combined with a diffraction-peak profile analysis, to be presented in Figures 21 and 22, it can be concluded that the hard grains (e.g., {310}) of $L1_2$ phase in Stage II have a sharp increase of dislocation densities and thus elevated hardening rates in Figure 19. However, the soft grains of $L1_2$ phase and all grain families of FCC phase have reduced rates of dislocation multiplication and thus a continued decrease of their tangent moduli. None of these conclusions can be easily made without the quantification of $E^*_{hkl,\alpha}$.

From the diffraction peak shifts (thus leading to all $\varepsilon^{el}_{hkl,\alpha}$) and the peak heights (thus approximately giving $f_{hkl,\alpha}$ in Eq. (3)) of a given phase, the Rietveld analysis gives the phase strain, $\varepsilon^{el}_{\alpha}$, as plotted in Figure 20(a). Multiplied with the phase-specific Young's modulus, the phase stress σ_α can be obtained as plotted against the overall strain in Figure 20(b), from which the phase-specific tangent moduli can be extracted as shown by the thick solid curves in Figure 19. The average phase stress, which can be calculated with rule of mixtures, $f_{L1_2}\sigma_{L1_2} + f_{FCC}\sigma_{FCC}$, which matches well with the measured bulk stress. The

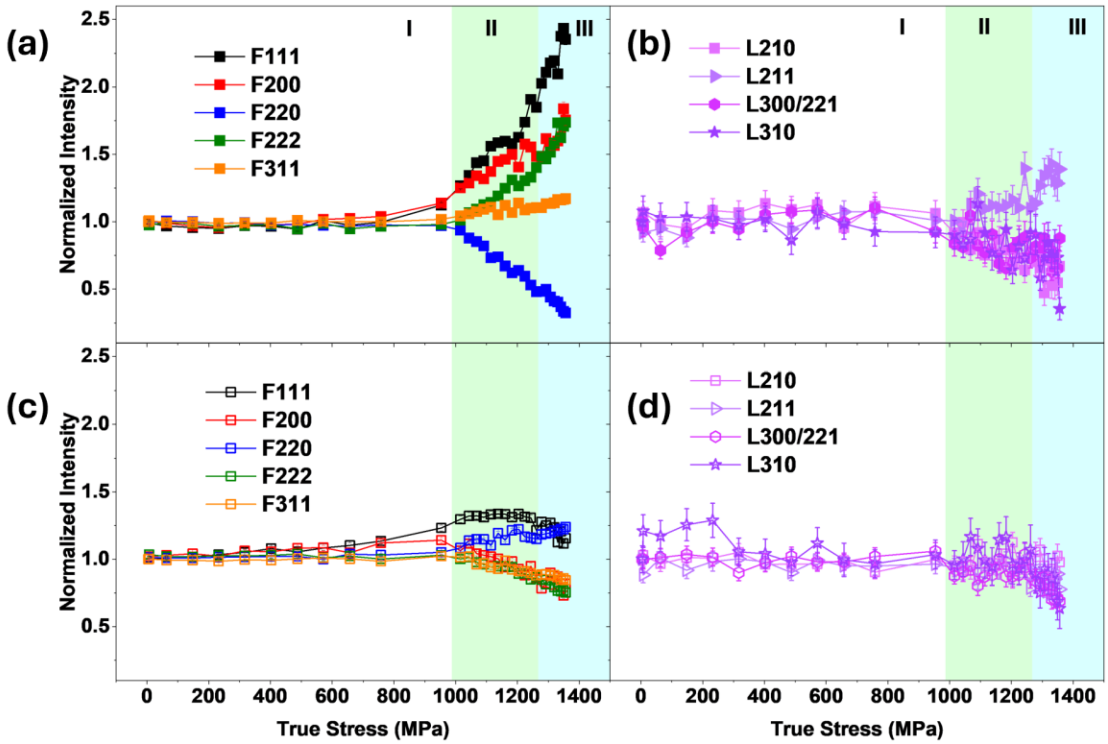


Figure 21. Evolution of normalized intensity of FCC phase in (a) loading direction and (c) transversal direction, and $L1_2$ precipitates in (b) loading direction and (d) transversal direction.

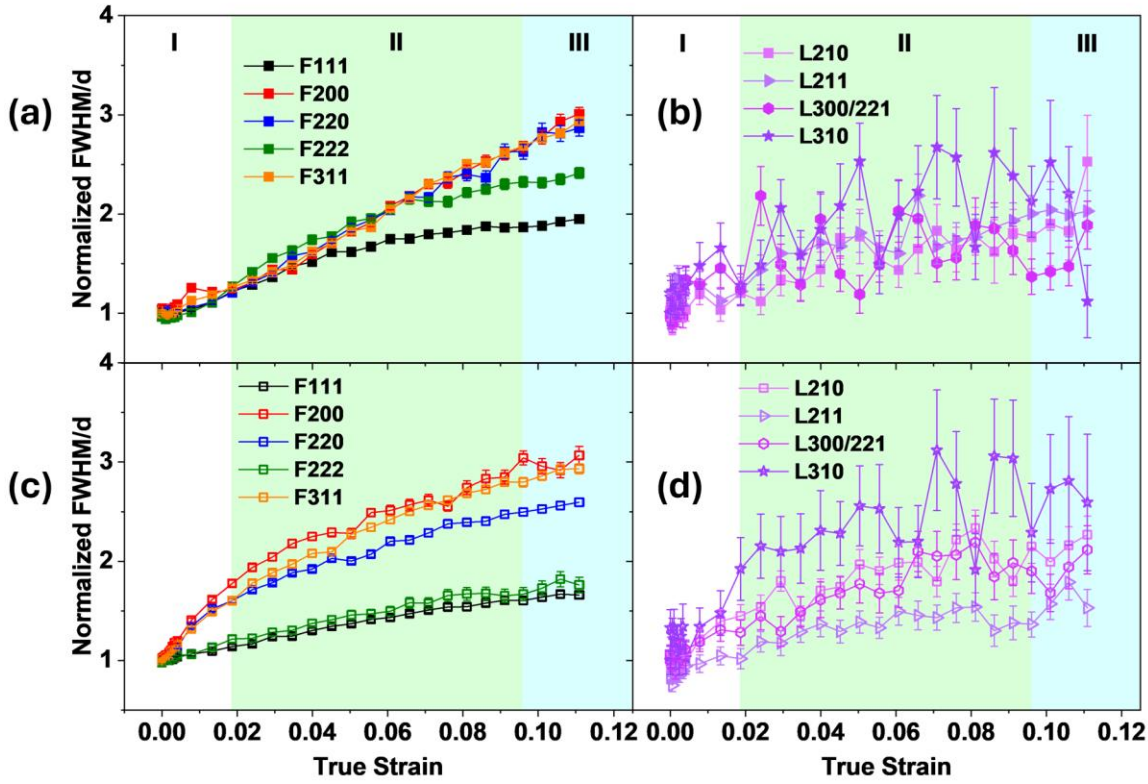


Figure 22. Evolution of normalized peak width divided with d-spacing of FCC phase in (e) loading direction and (g) transversal direction, and $L1_2$ precipitates in (f) loading direction and (h) transversal direction.

evolution of E_{α}^{*} confirms that during Stage I, FCC phase bears more load, and then the load is transferred to $L1_2$ phase during Stage II, followed by a transfer back to the FCC phase during Stage III. The extracted overall phase behavior during loading in Figure 20 does not represent the intrinsic mechanical behavior of each phase directly because each phase experiences different lattice strain histories in different grain orientations due to different slip systems, dislocation behavior, and other possible intrinsic mechanical mechanisms. For these reasons, the lattice strain, intensity, and peak width evolution is evaluated, giving rise to $E_{hkl,\alpha}^{*}$. Apparently, E_{α}^{*} is not a weighted average of $E_{hkl,\alpha}^{*}$, and the latter gives more salient features that can be connected to the dislocation density studies in Figures. 21 and 22.

Figures 21 and 22 presents the evolution of normalized intensity and normalized peak width divided with the d-spacing of the corresponding grain orientation (FWHM/d) of the FCC and $L1_2$ phases in both LD and TD. The evolution of peak intensity gives qualitative information on grain reorientation and rotation during plastic deformation [39] while the evolution of FWHM/d gives insight into strain-induced substructures such as dislocation and stacking faults during plastic deformation [40]. The increase in normalized intensity indicates the grain families are reorienting during plastic deformation. Meanwhile, the decreasing trend indicates the grain families are rotating away. In Stage I, the integrated intensities of all grain families remained somewhat constant. In Stage II as shown in Figure 21(a), the normalized intensity of FCC {111}, {200}, and {222} grain families increased starting from around stress level of 1000 MPa, when the material started yielding. The intensity continued to increase until the end of Stage III, indicating grain

reorientation into these grain families. In contrast, the normalized intensity of FCC {220} decreased from Stage II until Stage III, indicating {220} grain families are rotating away. The opposite trend is observed in LD, as shown in Figure 21(c), where the normalized intensity of {220} increases while the normalized intensity of other grain families decreases. As shown in Figure 21(b), the normalized intensity of $L1_2$ {211} grain family increases from Stage II to Stage III, indicating grain reorientation. Meanwhile, the normalized intensity of the other grain families in $L1_2$ decreases from Stage II to Stage III, both in LD and TD. This trend indicates that the stronger grains are reorienting toward preferred grain orientation in LD to accommodate plastic slip [41].

As shown by the FWHM/d evolution of the FCC matrix in LD and TD in Figure 22, the peak broadening indicates the existence of substructures formed during plastic deformation, such as dislocations and stacking faults. Due to the $L1_2$ phase reflections having weaker peaks compared to the FCC phase reflections, the FWHM fit of $L1_2$ phases might have larger error compared to the FCC peaks, however the trend is still discernible. The FWHM/d increases from Stage I to Stage III for both the matrix and the precipitates in both LD and TD, but these increases are quite asynchronous among different phases/grain families. The {311} and {200} grain families of FCC phase have higher increases in FWHM/d, compared to the other soft grain families in this phase. Similarly, FWHM/d data of the hard grain families (e.g., {310} and {210}) in $L1_2$ phase jump quickly to high values in Stage II, while soft grain families only catch up later in Stage III. In Figure 19, $E^*_{310,L1_2}$ increases sharply in the middle of Stage II, which agree nicely with their sharp

increases in FWHM/d in Figs. 10(b) and 10(d). The soft grain family in $L1_2$ phase and all grain families in FCC phase do not exhibit the dramatic rise of tangent moduli, and correspondingly their FWHM/d data increase only moderately.

The Al_7Ti_7-this-work has great improvements in both strengths and ductility with the precipitation strengthening compared with the FeCoNi HEA [42]. However, the strengths and ductility of Al_7Ti_7-this-work are not as high as those of Al_7Ti_7-Yang from the literature [15]. In terms of strength, the $L1_2$ precipitate sizes could play an important role in strengthening effect. The large-sized particles (~100-200 nm) in this work could have rotations indicated by the normalized intensity evolution, while the small particles (~30-50 nm) [15] could have higher efficiency in hindering the dislocation movements. Although the composition of the alloy used in this work is similar as the one reported in [15], we observed different deformation behaviors through in situ neutron diffraction measurements. Unlike the post-mortem measurements which focus on relatively small local areas, it is now possible to obtain real-time statistical information of bulk material which is more comprehensive and straightforward for the investigations of deformation mechanisms. As schematically illustrated in Figure 23, in Stage I of this work, the FCC matrix yielded first which could be similar to the first stages with the dislocation slips in the reported Al_8Ti_6-Yang and Al_7Ti_7-Yang. In Stage II, the tangent moduli of various grain families in $L1_2$ phase are much higher than those in FCC phase, and $E^*_{310,L1_2}$ and $E^*_{210,L1_2}$ even display significant increases. In contrast, the reported Al_8Ti_6-Yang and Al_7Ti_7-Yang showed the features of slip trace and high-density dislocation walls (HDDWs) in their

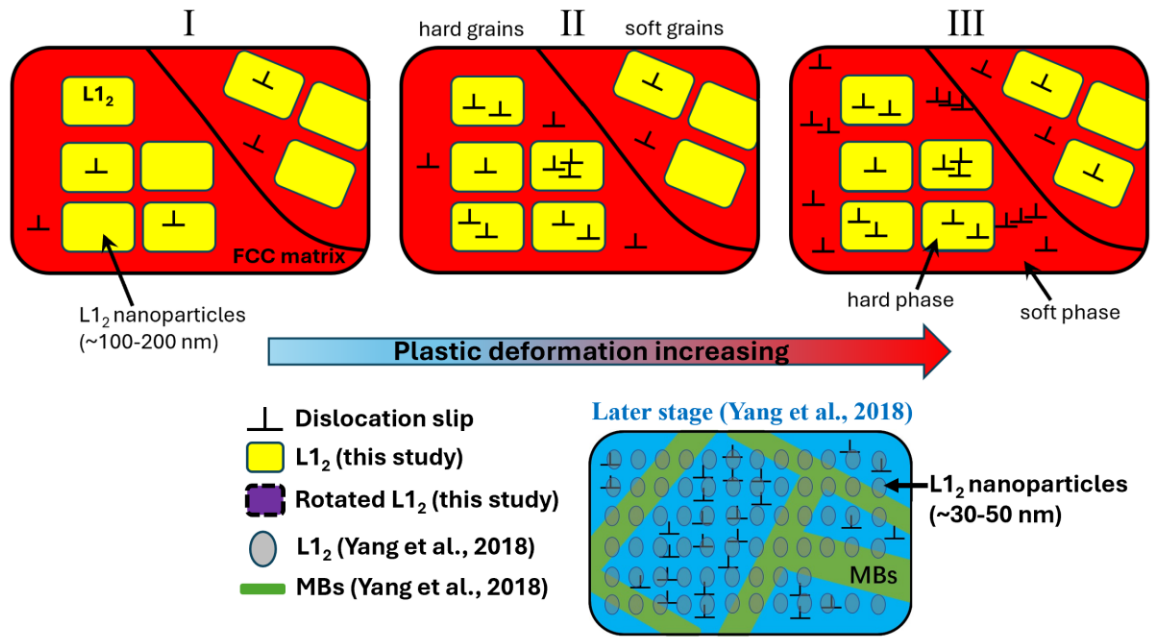


Figure 23. The evolution of deformation mechanisms in the three stages, including the initial elastic-plastic Stage I, the more pronounced hardening-rate in $L1_2$ than FCC phases in Stage II, and comparable dislocation densities in both phases in Stage III. As a comparison, the last stage in Yang et al. [15] has multiple micro-bands that extend over several precipitates, which are not seen in this work

second stages, respectively, but these post-mortem characterizations cannot identify the hardening-rate sequence as we found in Figure 19. In the third stage of the Al_7Ti_7-Yang, the micro-bands (MBs) were proposed to be the main deformation characteristics leading to the MBIP mechanism for the increase of ductility, although a mechanistic interpretation for MBIP is not known to the authors here. In contrast, the MBs were not observed in the late stage of deformation for Al_7Ti_7-this-work, primarily because our precipitates are several times larger in size. From the trend analysis in Figs. 8 and 10, schematics in Figure 23 show high and similar dislocation densities in hard grains of $L1_2$ phase in Stages II and III, but a low dislocation density in Stage II and a very high dislocation density in Stage III for hard grains of FCC phase. These conclusions can be further supported by the TEM image of the highly deformed specimen in Figure 15(c), whereas the dislocation mainly accumulates in the FCC matrix, consistent with it being the final active strengthening mechanism after precipitation hardening subsides.

The observation in Figure 21 indicates the rotation of {220} grain family in FCC matrix to rotate away at higher stress levels, which could efficiently release the stress concentrations and the coherent deformations between the two phases, thus lowering the strain accumulations and preventing crack initiation from precipitate-matrix interfaces [4]. In a single phase polycrystal, the texture tends to evolve to <211> orientation, but this is rarely as pronounced as in Figure 21(a). Note that the tangent modulus evolution in Figure 19 suggests that among all possible $E^*_{hkl,\alpha}$ out of fundamental reflections, the softest is $E^*_{220,FCC}$. The range in $E^*_{hkl,\alpha}$ (i.e., $E^*_{310,L1_2}$ vs $E^*_{220,FCC}$ in Stage II) in Figure 19 is more than one order of magnitude higher than that in a single-phase polycrystal made by the FCC

matrix phase. This could be the reason for an elevated degree of texture evolution in the two-phase material here.

Conclusions

Deformation mechanisms in two-phase or precipitation-strengthened alloys are often investigated by post-mortem or interrupted characterizations, so a quantitative and real-time understanding is still lacking. Using a nanoprecipitation-strengthened high entropy alloy, $(FeCoNi)_{86}Al_7Ti_7$, as an illustrative example, in situ neutron diffraction measurements are employed and a novel mechanics approach for the determination of tangent moduli is developed in this work, resulting in a quantitative assessment of successive hardening mechanisms for the ductility study of such materials. The successive deformation mechanisms were concluded from the lattice strain, intensity, peak width and tangent modulus evolutions of different grain orientations, which could delay the rapid decrease of the work hardening rate and thus help improve the tensile ductility of the material. In addition to the usual load sharing mechanism between the two phases based on the Rietveld analysis, salient features can be derived from the tangent modulus evolution. That is, in order to sustain a high overall hardening rate, a novel strategy would be to design a two-phase material with a wide range of $E^*_{hkl,\alpha}$, which will activate very different degrees of dislocation hardening of all these phases/grain families. As a result, successive hardening mechanisms can be realized, and features resembling TRIP behavior (e.g., $E^*_{310,L1_2}$ at 7% in Figure 19) can even be achieved by the standard dislocation plasticity.

References

1. Niu, M., G. Zhou, W. Wang, M.B. Shahzad, Y. Shan, and K. Yang, *Precipitate evolution and strengthening behavior during aging process in a 2.5 GPa grade maraging steel.* Acta Materialia, 2019. **179**: p. 296-307.
2. Li, Y., W. Yan, J.D. Cotton, G.J. Ryan, Y. Shen, W. Wang, Y. Shan, and K. Yang, *A new 1.9 GPa maraging stainless steel strengthened by multiple precipitating species.* Materials & Design, 2015. **82**: p. 56-63.
3. Xu, S., Y. Zhao, D. Chen, L. Sun, L. Chen, X. Tong, C. Liu, and Z. Zhang, *Nanoscale precipitation and its influence on strengthening mechanisms in an ultra-high strength low-carbon steel.* International Journal of Plasticity, 2019. **113**: p. 99-110.
4. Jiang, S., H. Wang, Y. Wu, X. Liu, H. Chen, M. Yao, B. Gault, D. Ponge, D. Raabe, and A. Hirata, *Ultrastrong steel via minimal lattice misfit and high-density nanoprecipitation.* Nature, 2017. **544**(7651): p. 460-464.
5. Xie, D., Z. Li, T. Sasaki, Y. Gao, Z. Lyu, R. Feng, Y. Chen, K. An, H. Chew, and T. Nakata, *Identifying the effect of coherent precipitates on the deformation mechanisms by in situ neutron diffraction in an extruded magnesium alloy under low-cycle fatigue conditions.* Acta Materialia, 2023. **251**: p. 118903.
6. Gao, L., R. Chen, and E. Han, *Microstructure and strengthening mechanisms of a cast Mg–1.48 Gd–1.13 Y–0.16 Zr (at.%) alloy.* Journal of materials science, 2009. **44**(16): p. 4443-4454.

7. Xie, D., Z. Lyu, M. Fan, H.B. Chew, P.K. Liaw, H. Bei, Z. Zhang, and Y. Gao, *Micromechanical origin of the enhanced ductility in twinless duplex Mg–Li alloy.* Materials Science and Engineering: A, 2021. **815**: p. 141305.

8. Cantor, B., I.T. Chang, P. Knight, and A. Vincent, *Microstructural development in equiatomic multicomponent alloys.* Materials Science and Engineering: A, 2004. **375**: p. 213-218.

9. Yeh, J.W., S.K. Chen, S.J. Lin, J.Y. Gan, T.S. Chin, T.T. Shun, C.H. Tsau, and S.Y. Chang, *Nanostructured high-entropy alloys with multiple principal elements: novel alloy design concepts and outcomes.* Advanced engineering materials, 2004. **6**(5): p. 299-303.

10. Li, W., D. Xie, D. Li, Y. Zhang, Y. Gao, and P.K. Liaw, *Mechanical behavior of high-entropy alloys.* Progress in Materials Science, 2021. **118**: p. 100777.

11. Li, Z., K.G. Pradeep, Y. Deng, D. Raabe, and C.C. Tasan, *Metastable high-entropy dual-phase alloys overcome the strength–ductility trade-off.* Nature, 2016. **534**(7606): p. 227-230.

12. Lei, Z., X. Liu, Y. Wu, H. Wang, S. Jiang, S. Wang, X. Hui, Y. Wu, B. Gault, and P. Kontis, *Enhanced strength and ductility in a high-entropy alloy via ordered oxygen complexes.* Nature, 2018. **563**(7732): p. 546-550.

13. Pan, Q., L. Zhang, R. Feng, Q. Lu, K. An, A.C. Chuang, J.D. Poplawsky, P.K. Liaw, and L. Lu, *Gradient cell–structured high-entropy alloy with exceptional strength and ductility.* Science, 2021. **374**(6570): p. 984-989.

14. Shi, P., R. Li, Y. Li, Y. Wen, Y. Zhong, W. Ren, Z. Shen, T. Zheng, J. Peng, and X. Liang, *Hierarchical crack buffering triples ductility in eutectic herringbone high-entropy alloys.* Science, 2021. **373**(6557): p. 912-918.

15. Yang, T., Y. Zhao, Y. Tong, Z. Jiao, J. Wei, J. Cai, X. Han, D. Chen, A. Hu, and J. Kai, *Multicomponent intermetallic nanoparticles and superb mechanical behaviors of complex alloys.* Science, 2018. **362**(6417): p. 933-937.

16. He, J., H. Wang, H. Huang, X. Xu, M. Chen, Y. Wu, X. Liu, T. Nieh, K. An, and Z. Lu, *A precipitation-hardened high-entropy alloy with outstanding tensile properties.* Acta Materialia, 2016. **102**: p. 187-196.

17. Liu, W., Z. Lu, J. He, J. Luan, Z. Wang, B. Liu, Y. Liu, M. Chen, and C. Liu, *Ductile CoCrFeNiMox high entropy alloys strengthened by hard intermetallic phases.* Acta Materialia, 2016. **116**: p. 332-342.

18. Guo, Y., M. Li, P. Li, C. Chen, Q. Zhan, Y. Chang, and Y. Zhang, *Microstructure and mechanical properties of oxide dispersion strengthened FeCoNi concentrated solid solution alloys.* Journal of Alloys and Compounds, 2020. **820**: p. 153104.

19. Chen, Y., H. Deng, Z. Xie, M. Wang, J. Yang, T. Zhang, Y. Xiong, R. Liu, X. Wang, and Q. Fang, *Tailoring microstructures and tensile properties of a precipitation-strengthened (FeCoNi)94Ti6 medium-entropy alloy.* Journal of Alloys and Compounds, 2020. **828**: p. 154457.

20. Fu, A., B. Liu, S. Xu, J. Huang, Y. Zhang, Y. Cao, and Y. Liu, *Mechanical properties and microstructural evolution of a novel (FeCoNi) 86.93 Al6. 17Ti6. 9 medium*

entropy alloy fabricated via powder metallurgy technique. Journal of Alloys and Compounds, 2021. **860**: p. 158460.

21. Gwalani, B., S. Gorsse, V. Soni, M. Carl, N. Ley, J. Smith, A.V. Ayyagari, Y. Zheng, M. Young, and R.S. Mishra, *Role of copper on L12 precipitation strengthened FCC based high entropy alloy.* Materialia, 2019. **6**: p. 100282.
22. Amalia, L., Y. Li, H. Bei, Y. Chen, D. Yu, K. An, Z. Lyu, P.K. Liaw, Y. Zhang, Q. Ding, and Y. Gao, *Copper effects on the microstructures and deformaiton mechanisms of CoCrFeNi high entroy alloys*. Applied Physics Letters, 2024. **124**: p. 141901.
23. Ma, Y., B. Jiang, C. Li, Q. Wang, C. Dong, P.K. Liaw, F. Xu, and L. Sun, *The BCC/B2 morphologies in Al x NiCoFeCr high-entropy alloys.* Metals, 2017. **7**(2): p. 57.
24. Ma, H., Y. Zhao, J. Luo, Y. Su, T. Zheng, Z. Yu, Y. Wu, and Y. Gao, *Sequential hardening mechanisms in addtive-manufactured NiTi shape memory alloys that can signficantly delay compressive failure*. Materials Today, 2025. **87**: p. 36-48.
25. Liu, T., X. Zhang, W. Song, C. Li, P. Wang, D. Li, Y. Zhu, and Y. Li, *Dynamic hetero-deformation induced hardening through strength reversal between hetero-zones in austenite-ferrite duplex steel*. Acta Materialia, 2025. **293**: p. 121120.
26. An, K., Y. Chen, and A.D. Stoica, *VULCAN: A "hammer" for high-temperature materials research.* Mrs Bulletin, 2019. **44**(11): p. 878-885.

27. An, K., H.D. Skorpenske, A.D. Stoica, D. Ma, X.-L. Wang, and E. Cakmak, *First in situ lattice strains measurements under load at VULCAN.* Metallurgical and Materials Transactions A, 2011. **42**: p. 95-99.

28. An, K., *Data reduction and interactive visualization software for event mode neutron diffraction.* ORNL Report, ORNL-TM-2012, 2012. **621**.

29. Rietveld, H.M., *A profile refinement method for nuclear and magnetic structures.* Applied Crystallography, 1969. **2**: p. 65-71.

30. Larson, A.C. and R.B. Von Dreele, General Structure Analysis System (GSAS). LANSCE, MS-H805, 1994.

31. Huang, S., Y. Gao, K. An, L. Zheng, W. Wu, Z. Teng, and P.K. Liaw, *Deformation mechanisms in a precipitation-strengthened ferritie superalloy revealed by in situ neutron diffraction studies at elevated temperatures*. Acta Materialia, 2015. **83**: p. 137-148.

32. Lyu, Z., C. Liu, D. Xie, R. Feng, D. Yu, Y. Chen, K. An, Y. Gao, H. Wang, and P.K. Liaw, *Low cycle fatigue peformance of Al0.3CoCrFeNi high entropy alloys: in situ neutron diffraction studies on the precipitation effects*. Intermetallics, 2024. **168**: p. 108241.

33. Stoica, G.M., A.D. Stoica, K. An, D. Ma, S. Vogel, J. Carpenter, and X.-L. Wang, *Extracting grain-orientation-dependent data from in situ time-of-flight neutron diffraction. I. Inverse pole figures.* Applied Crystallography, 2014. **47**(6): p. 2019-2029.

34. Xie, D., L. Huang, H.C. Shih, H. Tran, H.B. Chew, Z. Lyu, P.K. Liaw, Y. Ren, A.F. Bower, and Y.F. Gao, *In situ synchrotron X-ray diffraction and crystal plasticity studies of the deformation and fatigue crack growth behavior in a TRIP-assisted advanced high strength steel*. Acta Materialia, 2025. **293**: p. 121122.

35. Wong, S.L. and P.R. Dawson, *Influence of directional strength-to-stiffness on the elastic-plastic transition of FCC polcyrsytals under uniaxial tensile loading*. Acta Materialia, 2010. **58**: p. 1658-1678.

36. Zheng, L., Y. Gao, Y. Wang, A.D. Stoica, K. An, and X.L. Wang, *Grain orientation dependence of lattice strains and intergranular damage rates in polycrystals under cyclic loading*. Scripta Materialia, 2013. **68**: p. 265-268.

37. Kröner, E. *Berechnung der elastischen Konstanten des Vielkristalls aus den Konstanten des Einkristalls. Zeitschrift für Physik*, 1958. **151**(4): p. 504–518.

38. Wang, Z., A.D. Stoica, D. Ma, and A.M. Beese. *Diffraction and single-crystal elastic constants of Inconel 625 at room and elevated temperatures determined by neutron diffraction. Materials Science and Engineering: A*, 2016. **674**: p. 406–412.

39. Woo, W., E.-W. Huang, J.-W. Yeh, H. Choo, C. Lee, and S.-Y. Tu, *In-situ neutron diffraction studies on high-temperature deformation behavior in a CoCrFeMnNi high entropy alloy.* Intermetallics, 2015. **62**: p. 1-6.

40. Gao, Y., Y. Ding, H. Li, H. Dong, R. Zhang, J. Li, and Q. Luo, *Grain-size dependent elastic-plastic deformation behaviour of inconel 625 alloy studied by in-situ neutron diffraction.* Intermetallics, 2021. **138**: p. 107340.

41. Huang, E.-W., R. Barabash, N. Jia, Y.-D. Wang, G.E. Ice, B. Clausen, J. Horton, and P.K. Liaw, *Slip-system-related dislocation study from in-situ neutron measurements.* Metallurgical and Materials Transactions A, 2008. **39**: p. 3079-3088.

42. Wu, Z., Y. Gao, and H. Bei, *Thermal activation mechanisms and Labusch-type strengthening analysis for a family of high-entropy and equiatomic solid-solution alloys.* Acta Materialia, 2016. **120**: p. 108-119.

43. Coakley, James, Dong Ma, Matthew Frost, David Dye, David N. Seidman, David C. Dunand, and Howard J. Stone. *Lattice strain evolution and load partitioning during creep of a Ni-based superalloy single crystal with rafted γ′ microstructure. Acta materialia* 135 (2017): 77-87.

44. Liang, Yao-Jian, Linjing Wang, Yuren Wen, Baoyuan Cheng, Qinli Wu, Tangqing Cao, Qian Xiao et al. *High-content ductile coherent nanoprecipitates achieve ultrastrong high-entropy alloys. Nature communications* 9, no. 1 (2018): 4063.

45. Gao, Hongwei, Minghe Zhang, Ze Ji, Zhiye Zhang, Yunli Feng, Haiyang Chen, Shilei Li, and Yandong Wang. *Quantitative analysis of the micromechanical behavior and work hardening in Fe-0.1 C–10Mn steel via in-situ high-energy X-ray diffraction*. *Journal of Materials Research and Technology* 33 (2024): 773-784.

46. Mao, Wenqi, Si Gao, Wu Gong, Yu Bai, Stefanus Harjo, Myeong-Heom Park, Akinobu Shibata, and Nobuhiro Tsuji. *Quantitatively evaluating respective contribution of austenite and deformation-induced martensite to flow stress, plastic*

strain, and strain hardening rate in tensile deformed TRIP steel. Acta Materialia 256 (2023): 119139.

47. Gao, Si, Takuma Yoshimura, Wenqi Mao, Yu Bai, Wu Gong, Myeong-heom Park, Akinobu Shibata, Hiroki Adachi, Masugu Sato, and Nobuhiro Tsuji. *Tensile deformation of ultrafine-grained Fe-Mn-Al-Ni-C alloy studied by in situ synchrotron radiation X-ray diffraction. Crystals* 10, no. 12 (2020): 1115.

CHAPTER IV

TENSION-COMPRESSION ASYMMETRY IN HF-TI-ZR-NB-TA REFRACTORY HIGH ENTROPY ALLOYS STUDIED WITH IN SITU NEUTRON DIFFRACTION

This chapter is based on a manuscript prepared by Lia Amalia, Nathan Grain, Anshu Raj, Koushik Dey, Xin Wang, Kaijun Yin, John Whitlow, Xuesong Fan, Yanfei Gao, Ke An, Yan Chen, Dunji Yu, Shuozhi Xu, Jian-Min Zuo, Eric A. Lass, and Peter K. Liaw:

Lia Amalia, Nathan Grain, Anshu Raj, Koushik Dey, Xin Wang, Kaijun Yin, John Whitlow, Xuesong Fan, Yanfei Gao, Ke An, Yan Chen, Dunji Yu, Shuozhi Xu, Jian-Min Zuo, Eric A. Lass, and Peter K. Liaw. "Tension-compression asymmetry in Hf-Ti-Zr-Nb-Ta refractory high entropy alloys studied with in situ neutron diffraction."

This chapter has been reformatted to conform to the formatting requirements of the University of Tennessee, Knoxville, and to fit the structure of this dissertation. Lia Amalia contributed to the preparation of this chapter through data curation, formal analysis, investigation, methodology, software, validation, visualization, writing–original draft, and writing–review and editing. The coauthors contributed to the manuscript through combinations of conceptualization, data curation, formal analysis, investigation, methodology, resources, supervision, validation, visualization, and writing–review and editing.

Abstract

Hf–Nb–Ta–Ti–Zr refractory high-entropy alloys (RHEAs) offer a useful model system for examining how BCC phase stability affects deformation behavior. Here, in situ neutron diffraction measurements were performed during tensile and compressive loading of Hf–Nb–Ta–Ti–Zr RHEAs with systematically varied BCC phase stability. Orientation-dependent lattice strain evolution, peak broadening, lattice-strain-yielding behavior, and diffraction-derived elastic properties were analyzed and compared with Schmid and non-Schmid deformation criteria. The results show that changes in BCC phase stability are associated with distinct tension and compression responses, with differences in orientation-dependent yielding behavior. Peak-broadening and dislocation-density analyses further suggest that the deformation response cannot be fully described by conventional dislocation accumulation alone. By linking macroscopic mechanical behavior with in situ diffraction signatures and slip-activity predictions, this study provides a mechanistic framework for understanding the transition between Schmid-dominated and non-Schmid-influenced deformation in Hf–Nb–Ta–Ti–Zr RHEAs.

Introduction

Refractory high entropy alloys (RHEAs) have attracted interest in high-temperature structural application due to their high strength and phase stability [1, 2]. However, the room temperature ductility especially in tensile load, remains inconsistent [3]. One of the key challenges is that many RHEAs exhibit good plasticity in compression but limited ductility in tension [3, 4]. The Hf-Nb-Ta-Ti-Zr system of the refractory high entropy alloys family has been studied most frequently, especially its equimolar variant [5]. HfNbTaTiZr

show good ductility at room temperature [6], retained its strength after heat treatment [7], and have excellent workability [8]. As Hf, Ti, and Zr are elements associated with hexagonal close-packed (HCP) structure and Nb and Ta are elements associated with body-centered cubic (BCC) structure [9], Hf-Nb-Ta-Ti-Zr alloy family provides useful framework to study BCC/HCP phase stability and its influence on mechanical behavior.

The equimolar HfNbTaTiZr in as-cast condition were found to have a decent yield strength and ductility. Dirras et al. [6] reported yield strength of 820 MPa and ductility of 8% and the as-cast HfNbTaTiZr were reported to deform by slip. It was also confirmed that micro-segregation of the dendritic structure did not affect the mechanical behavior [6]. Zyka et al. [10] also reported as-cast HfNbTaTiZr having a decent fracture elongation of 12.3% and yield strength of 1155 which they attributed to the retained stable BCC phase, compared to the other system in their study. Sheikh et al. [11] reported the mechanical properties of Hf0.5Nb0.5Ta0.5Ti1.5Zr where yield strength were retained at 900 MPa and fracture elongation were increased to 18.8%, which were attributed to the lower VEC value but only if BCC phase is stable. Lower VEC value was argued to increase ductility due to the failure mode change from tensile cleavage to shear failure or shear instability [11]. Lilensten et al. [12] reported transformation induced plasticity (TRIP) in as-cast HfNb0.18Ta0.18Ti1.27Zr and observed an increase in fracture elongation up to 23% with yield strength of 540 MPa. HfNb0.18Ta0.18Ti1.27Zr was designed to have a Bond order ($\overline{(B_o)}$) and d-orbital energy ($\overline{(M_d)}$) level value combination closer to the BCC/HCP metastability threshold. So, along this line, the stability of BCC phase which is influenced by the elemental composition is important to the strength and ductility of Hf-Nb-Ta-Ti-Zr

system. A more recent study on the effect of BCC/HCP element ratio was by Carpenter et al. [13] where the tensile properties on heat-treated Hf-Nb-Ta-Ti-Zr were examined. However, it was found that higher HCP-element concentrations in the alloy did not increase the fracture elongation meaningfully. Overall, these results suggest that for compositions that did not deform by TRIP mechanism, phase stability alone is not sufficient to explain the strength and ductility response. The controlling factor may lie in how the composition variation alters slip activity.

A crystalline material would start to slip when the shear acting on the available slip system becomes large enough, this is well known as Schmid law [14]. However, in some materials, Schmid law alone could not describe the deformation behavior and additional stress components from shear stresses perpendicular to the Burgers vector or normal stress acting on the slip plane could influence the dislocation nucleation or motion. These additional stress components acting in addition to Schmid law are called non-Schmid effect. Non-Schmid effect is particularly important in BCC metals due to the non-planar core structure of screw dislocation [15] and stresses that are not directly aligned with slip direction could alter the core configuration and change the Peierls stress required for dislocation glide [16]. The yielding may depend on the magnitude of Schmid factor and loading direction and orientation which produce tension-compression asymmetry and orientation-dependent deviations from Schmid-law predictions as a consequence [17, 18]. Pan et al. [19] investigated NbMoTaW nanowire and found that it is harder to deform this alloy in compression due to the higher energy barrier in the anti-twinning direction compared to the lower energy barrier in the twining direction under tension. The tension-

compression asymmetry in BCC RHEAs is expected to not be independent of the chemistry of the alloy system. Intrinsically, applied stress can influence the dislocation gliding through non-Schmid effects [18]. Extrinsically, the tensile failure can be accelerated by strain localization and crack opening, while compressive load could suppress crack opening and allow for continued plastic flow [20]. At the same time, composition difference can influence the preferred deformation pathways by slip or whether there is additional accessible strengthening through phase transformation [21]. Therefore, understanding the deformation response requires comparing the two loading modes and considering the stability of the BCC phase by compositional control [22].

Although the BCC and HCP phase stability has been widely discussed in the metastable RHEAs [21, 23], its connection to deformation affected by loading mode is not fully resolved. Previously studied systems have shown that changing the balance between HCP-associated elements (Hf, Ti, and Zr) and BCC-stabilizing elements (Nb and Ta) can modify the phase stability, dislocation behavior, and tensile ductility [6, 10-12]. However, the way these compositional changes influence the tension-compression asymmetry and transition between Schmid and non-Schmid deformation remains unclear. In the present work, we investigate the loading-mode-dependent deformation behavior in Hf-Nb-Ta-Ti-Zr-based RHEAs with thermodynamic composition selection, mechanical testing, and in situ neutron diffraction. The investigated compositions were selected within the BCC-HCP phase-stability landscape. Tension and compression tests were performed to quantify the macroscopic strength, ductility, and reveal the tension-compression asymmetry behavior of each composition. In situ tension and compression neutron diffraction tests were

conducted to track the possible changes in deformation mechanism in real time. The experimentally measured lattice-strain yielding sequence was then compared with the yield sequence calculated using Schmid-only and with non-Schmid effect criteria. Through this approach, the present study clarifies how phase stability and loading mode collectively control the deformation behavior in Hf-Nb-Ta-Ti-Zr-based RHEAs.

Methods

Calphad calculation and sample fabrication

To help with alloy selection within the BCC/HCP stability range of Hf-Nb-Ta-Ti-Zr-based RHEAs, the Gibbs free energy difference between the BCC and HCP phases of alloy systems found in literature were calculated using CALPHAD. The BCC/HCP stability difference is defined in Eq. 1,

$$\Delta G_{BCC-HCP} = G_m^{HCP}(x_i, T) - G_m^{BCC}(x_i, T) \quad \text{Eq. 1}$$

where $G_m^{BCC}(x_i, T)$ and $G_m^{HCP}(x_i, T)$ are the calculated molar Gibbs free energies of BCC and HCP phases, respectively, for the nominal composition x_i at temperature T. With this definition, a smaller value indicates HCP phase is more stable while a larger value indicates stronger stability of the BCC phase.

Selected compositions were fabricated using arc melting from pure elements (>99.9 wt.%). The samples were melted at least four times to make sure homogeneous mixing. The samples were cast into plate and rod shapes for tension and compression tests, respectively. The dog-bone tensile samples have 3×2.6×15 mm gauge volume while the rod compression samples have Ø6×15 mm gauge volume.

Mechanical test and neutron diffraction measurement

In situ neutron diffraction measurement were conducted at VULCAN Engineering Materials Diffractometer [24, 25], the Spallation Neutron Source (SNS), ORNL, with an MTS load frame. As illustrated in Figure 24, two types of samples were tested, which are dog-bone samples for in situ tensile tests and rod samples for in situ compression tests. The measurements were conducted in an uninterrupted manner for each sample and analyzed with VULCAN Data Reduction and Interactive Visualization software (VDRIVE). The collected data were divided into continuous, shorter, and equal time interval datasets. The datasets were then averaged to produce a single representative diffraction pattern per time interval to allow time-resolved analysis. Peak position in d-spacing, peak intensity, and peak width were extracted using single-peak fitting function in VDRIVE. The lattice strain (ε_{hkl}) of a particular $\{hkl\}$ reflection is determined by Eq. 2, while the peak broadening change was evaluated using Eq. 3. Where d_{hkl}^0 and $FWHM_{hkl}^0$ are the d-spacing and peak width at zero applied stress, respectively. Meanwhile, d_{hkl} and $FWHM_{hkl}$ are the d-spacing and peak width during mechanical loading, respectively.

$$\varepsilon_{hkl} = \frac{d_{hkl} - d_{hkl}^0}{d_{hkl}^0} \quad \text{Eq.2}$$

$$Normalized\ peak\ broadening = \frac{FWHM_{hkl} - FWHM_{hkl}^0}{d_{hkl}^0} \quad \text{Eq.3}$$

Dislocation density calculations

Modified Williamson-Hall peak broadening analysis was used to obtain dislocation density as shown in Eq. 4. Where $\Delta K = -K(\Delta d/d)$ with $K = 1/d$, d is d-spacing (nm),

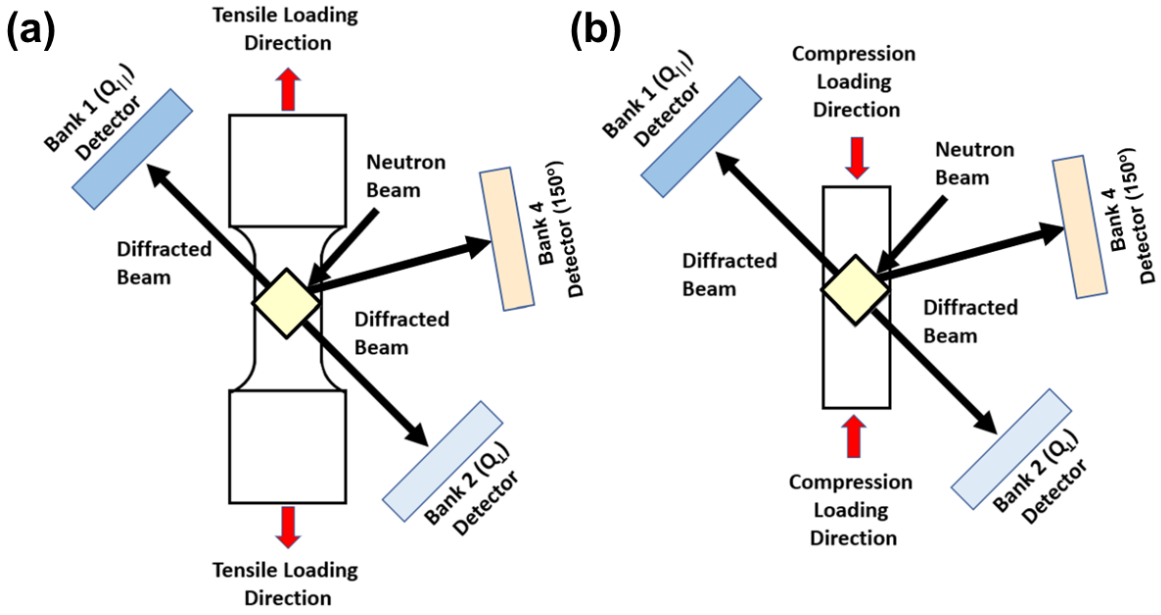


Figure 24. Experimental setup at VULCAN beamline, Spallation Neutron Source, Oak Ridge National Laboratory, illustrating mechanical test in (a) tension and in (b) compression.

Δd is the peak broadening in the full-width at half maximum (*FWHM*) (nm).

$$(\Delta K)^2 = (0.9/D)^2 + (\pi A^2 b^2)\rho(K^2 C) + O(K^2 C)^2 \quad \text{Eq.4}$$

Plotting $(\Delta K)^2$ on the y-axis versus $K^2 C$ on the x-axis, the intercept is proportional to $(0.9/D)^2$ where D is grain size. The slope is proportional to $(\pi A^2 b^2)\rho$ where A is a constant that depends on the effective outer cutoff radius of dislocation, b is Burger's vector of the dislocation ($b = \sqrt{2}a_0/2$), and ρ is the dislocation density. The last term, O refers to a noninterpreted higher-order term.

C is the contrast factor, which is calculated with Eq. 5, which is related to the contrast factor of $h00$ reflection (C_{h00}) and q, a parameter that quantifies the degree of anisotropy in dislocation strain fields. The value of both C_{h00} and q depends on the dislocation type, the centering of the crystal, and the ratio of C_{12}/C_{44}.

$$C = C_{h00}\left(1 - q\frac{h^2k^2 + k^2l^2 + l^2k^2}{(h^2 + k^2 + l^2)^2}\right) \quad \text{Eq. 5}$$

Local strain resistance

Simulation cells are built with specific crystallographic directions to facilitate the glide of dislocations. In all cells, the *y* axis is normal to the slip plane, either $\{110\}$ or $\{112\}$ plane. For edge dislocations, the *x* axis is parallel to the Burgers vector direction, which is $\langle 111 \rangle$; for screw dislocations, the *z* axis is parallel to the Burgers vector direction. Each simulation cell is sized at 40 nm, 50 nm, and 1 nm, respectively, along the *x*, *y*, and *z* directions. The total number of atoms varies by dislocation type and slip plane, ranging from 48,420 to 83,121. Periodic boundary conditions are applied along the *x* and *z* directions, while those along the *y* direction are traction-free. Once a dislocated cell is built, a gradual shear strain 10^{-6} per step for the screw dislocation and 10^{-5} per step for the edge

dislocation is applied. Energy minimization is applied after each incremental strain. We then monitor the dislocation motion across the crystal lattice until it traverses at least 1 nm.

To capture the randomness in atomic distribution, we build 10 to 20 atomistic structures for each dislocation type in each alloy. Three MPEAs, HfNbTiZr, $HfNb_{0.5}Ta_{0.5}TiZr$, and HfNbTaTiZr, are considered for the LSR calculations. The embedded-atom method interatomic potential developed by Xu et al. [26] is employed. LAMMPS [27] is used for all atomistic simulations; Atomsk [28] is utilized to construct crystalline structures; while OVITO [29] is employed for the analysis and visualization of our simulation outcomes.

Non-Schmid effect calculation

To calculate the non-Schmid effect and generate inverse pole figure of the hkl-specific yield stress, the orientation-dependent strains were calculated over each $[hkl]$ direction, treating it as the loading axis. For each orientation, the directional modulus E_{hkl} (Eq. 6) was calculated from the elastic constants (S_{11}, S_{12}, and S_{44}) obtained from the in situ neutron diffraction measurements. The BCC slip system of $\{110\}\langle 111\rangle$ was used as it is the most commonly activated slip system in BCC RHEAs. The resolved shear stress on each slip system was calculated using Eq. 7, where n_i and m_i are the slip-plane normal and slip direction, respectively. The resolved shear stress is calculated for both tension ($+\sigma$) and compression ($-\sigma$). The normal plane stress (NF_i) is calculated using Eq. 8. The Schmid-only yield strain is calculated using Eq. 9, while the non-Schmid yield strain is calculated using Eq. 10, where $\mu_2 = 0.2$ is the fraction of the non-Schmid effect contribution, with the sum of μ_1 and μ_2 equals to 1.

$$\frac{1}{E_{hkl}} = S_{11} - 2\left[(S_{11} - S_{12}) - \frac{1}{2}S_{44}\right]\frac{h^2k^2+k^2l^2+l^2h^2}{(h^2+k^2+l^2)^2} \quad \text{Eq. 6}$$

$$\tau_i = m_i \cdot \sigma \cdot n_i \quad \text{Eq. 7}$$

$$\tau NF_i = n_i \cdot \sigma \cdot n_i \quad \text{Eq. 8}$$

$$\varepsilon_{SF} = \frac{\tau_{CRSS}}{|\tau_i|\, E_{hkl}} \quad \text{Eq. 9}$$

$$\varepsilon_{nSF} = \frac{\tau_{CRSS}}{|\mu_1\tau_i + \mu_2\, \tau NF_i|\, E_{hkl}} \quad \text{Eq. 10}$$

Experimental Results

Compositional selection using BCC/HCP stability descriptor

The tensile elongation versus the $\Delta G_{BCC-HCP}$, along with the yield strength versus tensile elongation and the $\overline{B_o}$ versus $\overline{M_d}$ plot is presented in Figure 2. From Figure 2(a), eliminating either Nb or Ta while keeping both compositions relatively smaller than Hf, Ti, and Zr increased the stability of the HCP phase, reduced the $\Delta G_{BCC-HCP}$, and deformed by TRIP [23, 30]. Meanwhile, the equimolar composition of HfTiZr-X (X = Ta, Nb) did not show TRIP [23, 31]. However, comparing HfNbTiZr and HfTaTiZr, although having similar $\Delta G_{BCC-HCP}$ of -310 and -202, respectively, replacing Nb with Ta decreased the ductility significantly due to formation of secondary phases [31]. On the opposite end, eliminating Hf stabilized the BCC phase, increasing the $\Delta G_{BCC-HCP}$, but reducing the ductility [32]. In $NbTa_XTi_{(2-X)}Zr$ (X = 0.2, 0.4, 0.6, 0.8) system, when Ta is more than 15 at%, Nguyen et al. reported [32] the lattice distortion increased which increased strengthening but reducing the ductility. However, when Ta is below 10 at%, as seen in Figure 2(a), for $NbTa_{0.2}Ti_{1.8}Zr$ and $NbTa_{0.4}Ti_{1.6}Zr$, the BCC stability is reduced. It was reported that the lattice distortion is reduced enough to allow dislocation to move more easily and increased ductility [32].

Compared to HfNbTaTiZr, increasing Ti while reducing Hf-Nb-Ta increased the ductility in $Hf_{0.5}Nb_{0.5}Ta_{0.5}Ti_{1.5}Zr$ [11], and as can be observed from Figure 2(a), the BCC stability is reduced. Further composition modification on $HfNb_{0.18}Ta_{0.18}Ti_{1.27}Zr$ reduced the BCC stability further and increased the ductility by TRIP [12]. It also should be pointed out that an appropriate heat treatment for Hf-Nb-Ta-Ti-Zr could have a higher ductility while still maintaining strength [13].

Figure 25(b) shows the $\overline{B_o}$ - $\overline{M_d}$ map based on Ti-alloys [33, 34], where the red dash line corresponds to the values of which martensitic transformation of BCC to HCP will occur at room temperature (Ms=RT). The $\overline{B_o}$ - $\overline{M_d}$ map correctly predicts the $HfTa_XTiZr$, $HfNb_XTiZr$, and $HfNb_{0.18}Ta_{0.18}Ti_{1.27}Zr$ to deform by TRIP, since their $\overline{B_o}$ - $\overline{M_d}$ values are closer to the Ms=RT line. However, $NbTa_{0.2}Ti_{1.5}Zr$ is also relatively closer to Ms=RT line but it did not deform by TRIP. It should be noted that its BCC phase is still relatively more stable than HCP phase because the $\Delta G_{BCC-HCP}$ for $NbTa_{0.2}Ti_{1.5}Zr$ is 1659 J/mol. On the opposite end, based on the $\Delta G_{BCC-HCP}$ of -1900, $Ti_{20}Zr_{20}Hf_{20}Nb_{35}Ta_5$ should fall under the TRIP region in Figure 25(a). However, in the $\overline{B_o}$ - $\overline{M_d}$ map $Ti_{20}Zr_{20}Hf_{20}Nb_{35}Ta_5$ is relatively far from Ms=RT line which might explain why this composition did not deform by TRIP.

Figure 25(c) presents the tensile elongation versus the yield strength. Generally, compositions with lower value of $\Delta G_{BCC-HCP}$ are more ductile but lower in yield strength, especially when deformation occurs by TRIP mechanism. In contrast, the compositions that have larger value of $\Delta G_{BCC-HCP}$ to be less ductile but larger in yield strength. Between

these two regimes, the transition region contains compositions which have a combination of moderate strength and ductility.

Composition selection based only on compositional change due to the tendency of a particular element to form one phase or another may be oversimplifying the design strategy of Hf-Nb-Ta-Ti-Zr system. Since the mechanical behavior is influenced by local chemical environment, lattice distortion, dislocation behavior, and transformation tendency, relating ductility with the phase stability might provide a more thermodynamic basis for composition selection. Although it is not expected to fully predict ductility on its own, relating ductility with the BCC/HCP phase stability offers a less arbitrary framework on designing ductile RHEAs. To examine the deformation behavior within the ductile composition population, three compositions were designed within Hf-Nb-Ta-Ti-Zr compositional space. $HfNb_{0.5}Ta_{0.5}TiZr$ with $\Delta G_{BCC-HCP}$ of -246 J/mol, $HfNbTa_{0.5}TiZr$ with $\Delta G_{BCC-HCP}$ of 1008 J/mol, and $Hf_{0.5}NbTa_{0.5}TiZr$ with $\Delta G_{BCC-HCP}$ of 2148 J/mol. This selection allows the effect of increasing BCC stability to be evaluated while keeping the compositions within a range where measurable tensile plasticity is expected.

Tensile and compression test coupled with in situ neutron diffraction measurement were performed with strain rate of 10^{-4} /s. The tensile elongation of the three chosen composition falls within the ductile region, as shown in Figure 2. More ex situ compressive tests were performed to assess the repeatability of the mechanical performance with strain rate of 10^{-3} /s. The average compressive yield strengths were 868.67 ± 5.7 MPa for $HfNb_{0.5}Ta_{0.5}TiZr$, 863 ± 3.7 MPa for $HfNbTa_{0.5}TiZr$, and 882.5 ± 8.5 MPa for $Hf_{0.5}NbTa_{0.5}TiZr$.

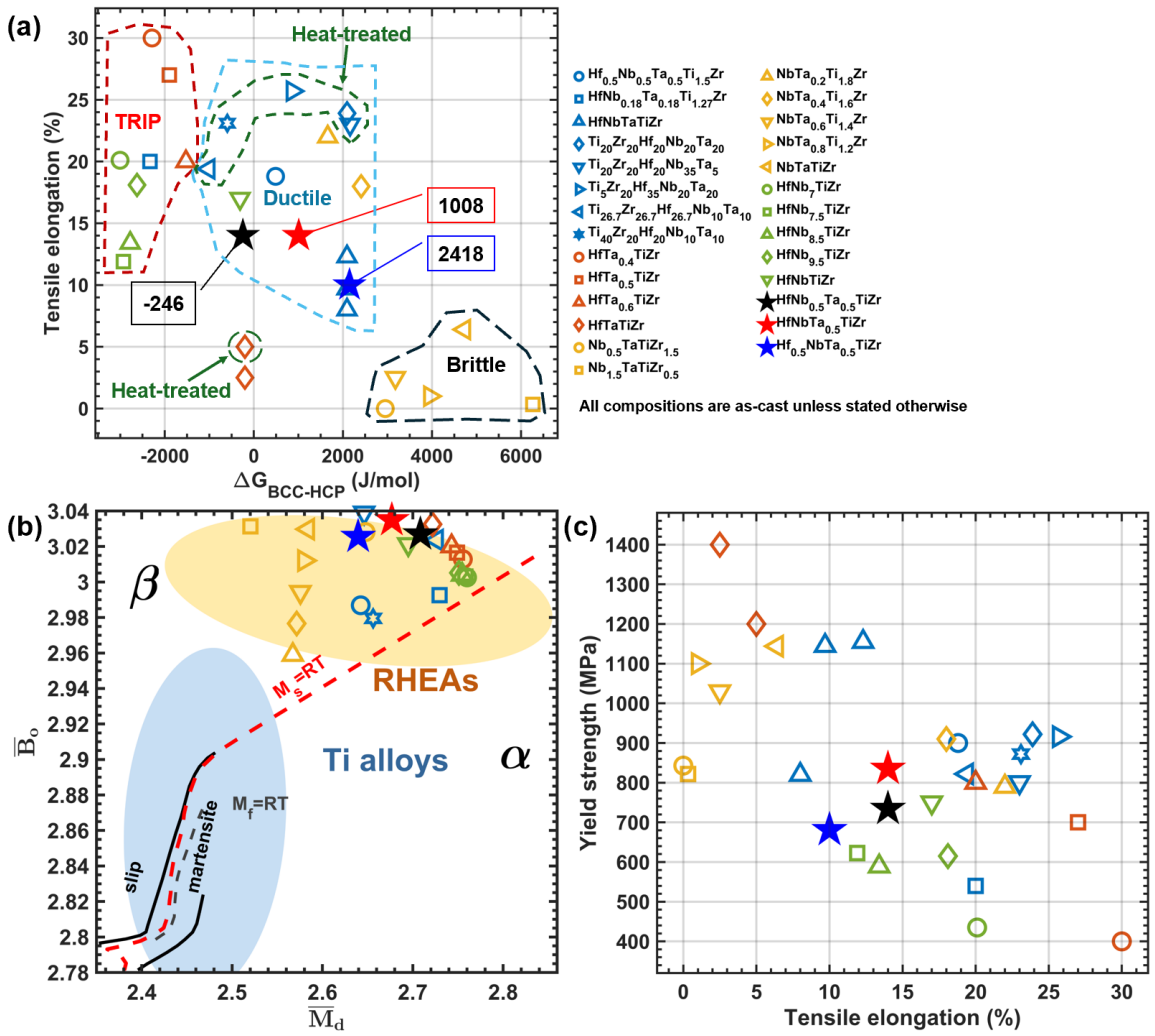


Figure 25. (a) Gibbs free energy of transformation from BCC to HCP versus tensile elongation, indicating compositions with transformation induced plasticity (TRIP) effect [12, 21, 30], ductile [11, 13, 32, 35], and brittle [10] during tensile loading. (b) Bond order ($\overline{B_o}$) versus d-orbital energy ($\overline{M_d}$) level [33, 34]. (c) Yield strength versus tensile elongation.

Macroscopic mechanical response and diffraction derived elastic constants

The stress strain curves of $HfNb_{0.5}Ta_{0.5}TiZr$, $HfNbTa_{0.5}TiZr$ and $Hf_{0.5}NbTa_{0.5}TiZr$ from both ex situ and in situ tests are presented in Figure 26, while the yield strength, elongation to failure, and necking strain is presented in Table 1. Figure 26(a) shows the true stress versus true strain curves obtained from in situ diffraction measurements during tensile loading overlayed with the corresponding work hardening rates. $HfNbTa_{0.5}TiZr$ has the highest strength, while $Hf_{0.5}NbTa_{0.5}TiZr$ has the lowest strength during in situ tension. $HfNbTa_{0.5}TiZr$ and $HfNb_{0.5}Ta_{0.5}TiZr$ have similar elongation to failure while $Hf_{0.5}NbTa_{0.5}TiZr$ failed at earlier elongation. Based on Considere's necking criterion, a material starts to neck during uniaxial loading when true stress equals to $d\sigma/d\varepsilon$ [36, 37]. $HfNb_{0.5}Ta_{0.5}TiZr$, $HfNbTa_{0.5}TiZr$, and $Hf_{0.5}NbTa_{0.5}TiZr$ have a descending order of necking strain, respectively. $HfNb_{0.5}Ta_{0.5}TiZr$ had a significant increase of work hardening rate from 4% strain until 8.5% strain, then decreased at a slower rate until it necked at 11% strain. $HfNbTa_{0.5}TiZr$ exhibited necking at approximately 3% strain, after which its work-hardening rate began to increase from 5% to 7.8% strain before decreasing again. Meanwhile, $Hf_{0.5}NbTa_{0.5}TiZr$ showed only a slower decrease in the work-hardening rate after necking began at approximately 2.5% strain, followed by a more pronounced decrease at higher strain.

Figure 26(b) shows the true stress versus true strain curves obtained from in situ diffraction measurements during compression loading overlayed with the corresponding work hardening rates. The in situ compression tests were stopped at approximately 5% strain to minimize safety risks associated with potential fragmentation or debris release

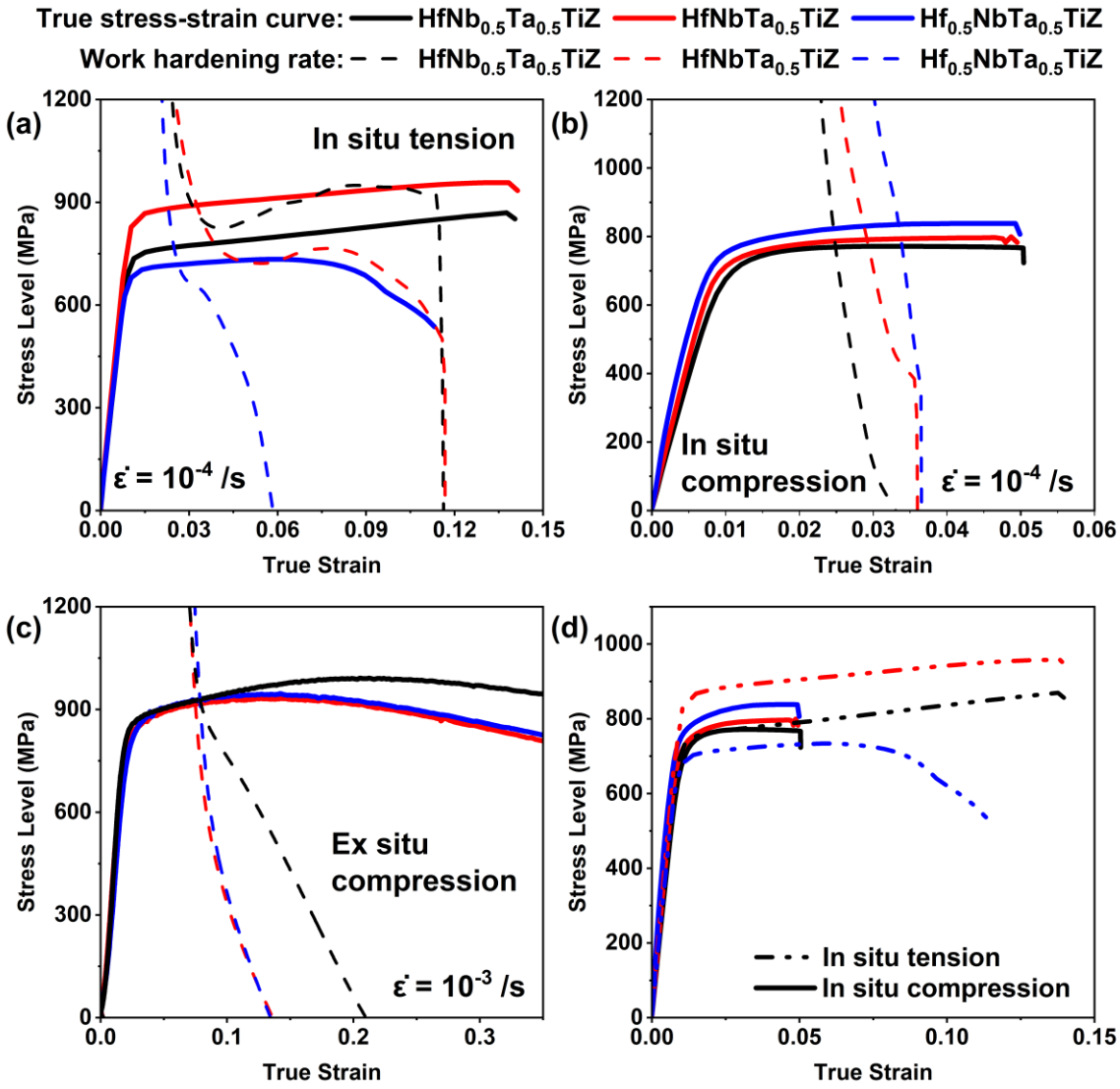


Figure 26. True stress versus true strain, overlapping with the corresponding work hardening rate, of (a) in situ tension tests, (b) in situ compression tests, and (c) ex situ compression tests. (d) True stress versus strain curves of in situ tension tests overlayed with in situ compression tests.

from neutron-irradiated specimens. $Hf_{0.5}NbTa_{0.5}TiZr$ has the highest yield strength, while $HfNb_{0.5}Ta_{0.5}TiZr$ has the lowest strength during in situ compression. $HfNb_{0.5}Ta_{0.5}TiZr$, $HfNbTa_{0.5}TiZr$, and $Hf_{0.5}NbTa_{0.5}TiZr$ have an increasing trend in necking strain, respectively. All three compositions did not show any additional hardening during this measurement.

Figure 26(c) shows the true stress versus true strain curves obtained from ex situ compression test overlayed with the corresponding work hardening rates. Although all three compositions did not fracture, the ex situ compression tests were terminated upon reaching 35% strain. All three compositions had similar yield strength and necking strain. $HfNb_{0.5}Ta_{0.5}TiZr$ shows larger hardening after necking compared to the other two compositions. The work hardening rate during in situ and ex situ measurement may seem contradictory, however the discrepancies could be explained from the different strain rates used. Furthermore, the hardening behavior that is observed in the ex situ test only start after around 7.8%, which the in situ measurement did not reach.

Figure 26(d) shows the true stress versus true strain from in situ diffraction measurement of all three compositions during tension and compression. $HfNb_{0.5}Ta_{0.5}TiZr$ with $\Delta G_{BCC-HCP}$ of -246 J/mol has similar yield strength in tension and compression. $Hf_{0.5}NbTa_{0.5}TiZr$ with $\Delta G_{BCC-HCP}$ of 2148 J/mol have higher yield strength in compression, while $HfNbTa_{0.5}TiZr$ with $\Delta G_{BCC-HCP}$ of 1008 J/mol have higher yield strength in tension. This trend suggests that variations in BCC phase stability may alter the deformation behavior and lead to distinct tension–compression asymmetry responses.

The elastic constants, C_{11}, C_{12}, and C_{44} were extracted from the in situ measurement during tension and compression and from there some derived elastic properties (Table 5) could be obtained [38-41]. There is a fairly large difference of C_{11} and C_{12} values between the data obtained from tension and compression tests, but there is no big difference in the C_{44} value. The elastic constants are fitted parameters from Kröner's self-consistent model rather than direct single-crystal elastic constants, therefore the large difference in the values obtained from tension and compression should be interpreted as evidence of anomalous tensile lattice-strain response rather than a true change in intrinsic elastic stiffness. Gnäupel-Herold et al. [42] suggests that diffraction-derived elastic constants are model-dependent effective quantities and abnormal results may indicate the measured lattice-strain response is affected by real microstructural or deformation physics beyond ideal elastic Kröner behavior.

Since there are discrepancies in elastic constants obtained from tension and compression, they should not be interpreted as intrinsic single-crystal elastic constants of the alloy. In principle, the elastic constants of a material should be independent of loading direction within the linear elastic regime. Therefore, the following discussion treats these values as apparent diffraction-derived elastic constants, reflecting the effective lattice-strain response measured under each loading condition. For these compositions, the anisotropy factor, A, also shows moderate elastic anisotropy, between A value of 1.3 to 1.5. Although the C_{11} and C_{12} values show fairly large differences, the average shear modulus, G_{Hill}, does not show large differences among different compositions and loading directions. This suggests all three compositions have similar resistance to shape change.

Table 5. Elastic constants, derived elastic properties, and mechanical properties. (Elastic constants, C_{11}, C_{11}, C_{11}; Zener anisotropy constant, A; bulk modulus, B; Tetragonal shear moduli G'; Hull shear modulus, G_H; Poisson's ratio, v; Pugh's ratio, P)

	Tension			Compression		
	$HfNb_{0.5}Ta_{0.5}TiZr$	$HfNbTa_{0.5}TiZr$	$Hf_{0.5}NbTa_{0.5}TiZr$	$HfNb_{0.5}Ta_{0.5}TiZr$	$HfNbTa_{0.5}TiZr$	$Hf_{0.5}NbTa_{0.5}TiZr$
C_{11}	206.28	225.07	173.25	188.08	143.59	138.59
C_{12}	159.32	171.59	123.02	140.49	88.61	84.36
C_{44}	35.51	38.24	36.27	34.13	37.02	35.85
A	1.512	1.430	1.443	1.434	1.346	1.322
v	0.418	0.417	0.395	0.411	0.360	0.358
B	174.97	189.42	139.76	156.35	106.94	102.44
G'	23.47	26.74	25.11	23.80	27.48	27.11
G_H	30.08	33.13	31.30	29.54	32.86	32.05
Ultimate strength	871	955	738	777	800	838
Yield strength	734	835	680	751	762	786
Elongation to failure	13	13	10	-	-	-
Necking strain	11	3	2.5	2.5	2.9	3.3

Meanwhile the bulk modulus, B, is higher in tension than compression for all three compositions. However, the bulk modulus is higher for $HfNb_{0.5}Ta_{0.5}TiZr$ and $HfNbTa_{0.5}TiZr$ in tension and the bulk modulus for $HfNb_{0.5}Ta_{0.5}TiZr$ is higher in compression while the other two compositions have similar value. This suggests that there is different variation of tension-compression asymmetry.

Lattice strain evolution

Generally, the lattice strain increases linearly with the true stress and true strain during elastic deformation regime then deviates from linearity upon reaching plastic deformation, from here on we will call this hkl-specific yield. The first grain orientation to reach hkl-specific yield can be considered the softer orientation because it requires less energy to activate [44]. The decreasing of lattice strain with applied stress or strain could be interpreted as slip in that orientation being activated while the increasing lattice strain with applied stress or strain could be interpreted as that orientation remain deforming elastically, bearing more load [45]. The variation in the slope of lattice strain below the elastic limit shown in Figure 27(a-f) is due to elastic anisotropy [46, 47].

Figure 27 is arranged to show possible correlation between $\Delta G_{BCC-HCP}$ and the lattice strain evolution. Figures 4(g), (h), and (i) present the evolution of lattice strain versus true strain of $HfNb_{0.5}Ta_{0.5}TiZr$, $HfNbTa_{0.5}TiZr$, and $Hf_{0.5}NbTa_{0.5}TiZr$, respectively during in situ neutron diffraction measurement in tension and compression. An overlap of lattice strain response in all grain orientations, except $\{110\}$ and $\{220\}$, during tension and compression loading could be observed from $HfNb_{0.5}Ta_{0.5}TiZr$. As $\Delta G_{BCC-HCP}$ increases, the overlap in lattice strain response collapses. In $HfNbTa_{0.5}TiZr$ only the lattice strain of

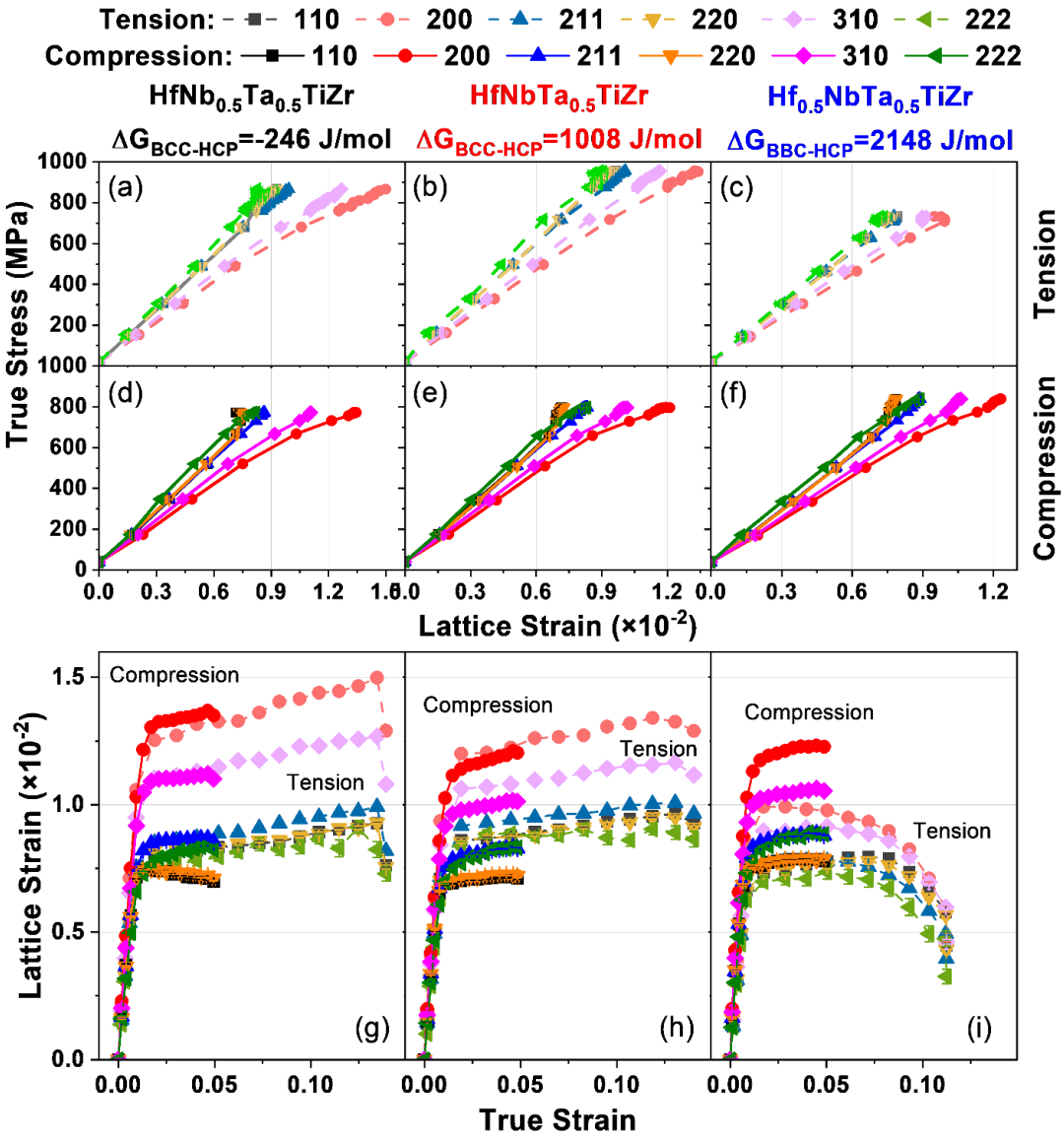


Figure 27. Lattice strain versus true strain of $HfNb_{0.5}Ta_{0.5}TiZr$, $HfNbTa_{0.5}TiZr$, and $Hf_{0.5}NbTa_{0.5}TiZr$ from in situ tension and compression neutron diffraction measurements. The negative values from the compression tests have been converted into positive values.

{200} overlaps during tension and compression loading. The other orientations of $HfNbTa_{0.5}TiZr$ need a higher load to trigger hkl-specific yield in tensile loading. Meanwhile, only the lattice strain of {110} overlaps during tension and compression loading in $Hf_{0.5}NbTa_{0.5}TiZr$, while the other orientations need a lower load to trigger hkl-specific yield during tension loading. This difference in hkl-specific yield response in $HfNb_{0.5}Ta_{0.5}TiZr$, $HfNbTa_{0.5}TiZr$, and $Hf_{0.5}NbTa_{0.5}TiZr$ suggests the macroscopic tension-compression asymmetry could be observed from the lattice strain response. In summary, the tension-compression asymmetry increases as $\Delta G_{BCC-HCP}$ increases.

Discussion

Non-Schmid effect

In this work, the non-Schmid contribution was approximated using the resolved normal stress on the candidate slip plane, following prior studies showing that dislocation nucleation or glide resistance can depend on stress components other than the conventional resolved shear stress [48]. This simplified normal-stress term captures the first-order effect of non-Schmid sensitivity on the orientation-dependent yield response, although full BCC non-Schmid behavior may also involve additional non-glide shear components and screw-core effects [49].

Figure 28 (a-c) and 29 (a-c) presents the calculated inverse pole figure of hkl-specific yield strain map with Schmid effect only in compression and tension, respectively. With the Schmid effect only, loading direction does not change hkl-specific yield sequence. In contrast, the inverse pole figure presented in Figure 28 (d-f) and Figure 29 (d-f) show changes in hkl-specific yield sequences due to the non-Schmid effect contribution. Figure

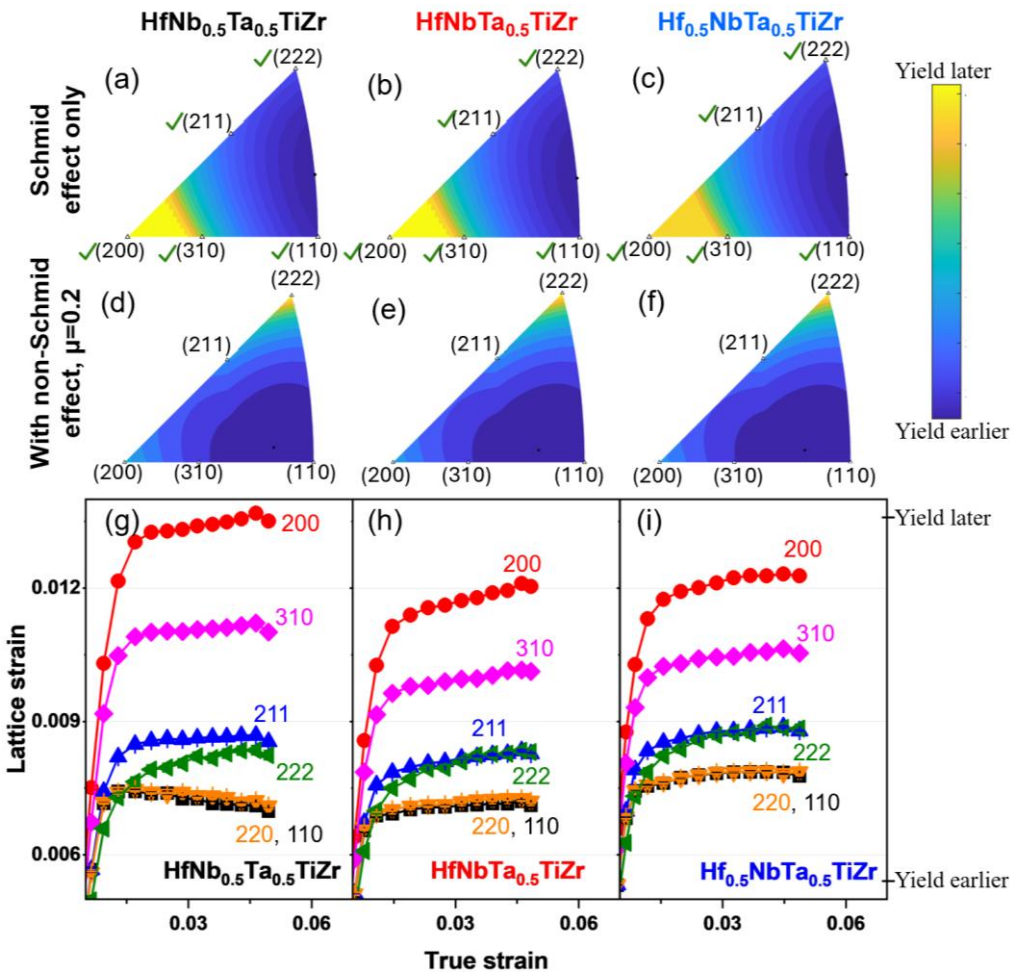


Figure 28. (a-c) Calculated Schmid effect and (d-f) calculated non-Schmid effect evaluation on the (g-i) hkl-specific yield strain sequence during compression loading for $HfNb_{0.5}Ta_{0.5}TiZr$, $HfNbTa_{0.5}TiZr$, and $Hf_{0.5}NbTa_{0.5}TiZr$.

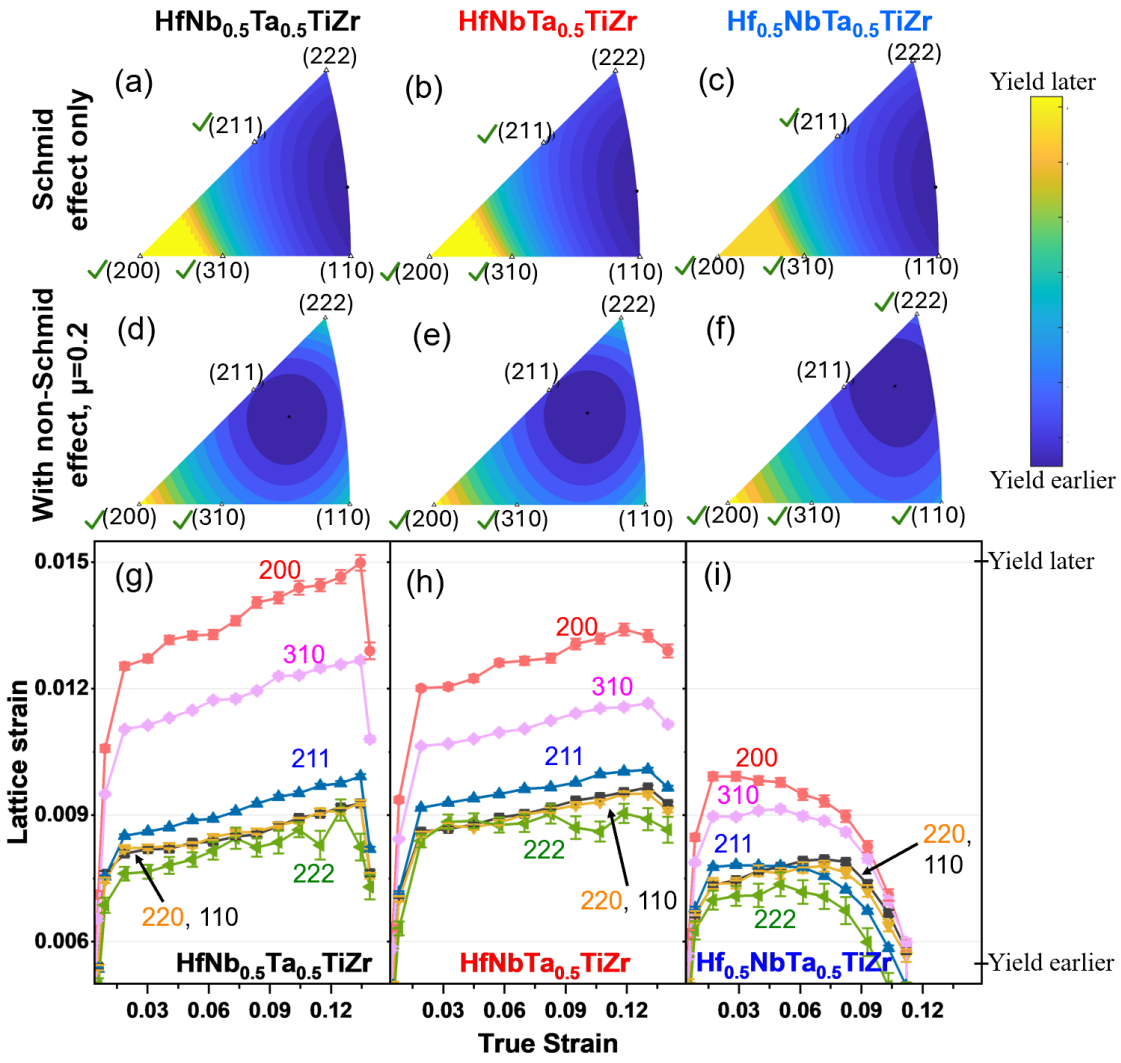


Figure 29. (a-c) Calculated Schmid effect and (d-f) calculated non-Schmid effect evaluation on the (g-i) hkl-specific yield strain sequence during tension loading for $HfNb_{0.5}Ta_{0.5}TiZr$, $HfNbTa_{0.5}TiZr$, and $Hf_{0.5}NbTa_{0.5}TiZr$.

28 and 29 (a-c) shows the hkl-specific yield sequence based only on Schmid's plasticity from yielding later to earlier to be {200}, {310}, {211}, {222}, and {110}. Figures 28 (g-i) show that the hkl-specific yield sequence for all three compositions during compression follow Schmid's plasticity.

The calculated hkl-specific yield sequence with non-Schmid effect presented in inverse pole figures in Figure 29 (d and e) during tension for $HfNb_{0.5}Ta_{0.5}TiZr$ and $HfNbTa_{0.5}TiZr$ has the sequence from later to earlier of {200}, {310}, followed by {110} and {222} yielding at the same strain level, and followed by {211}. For $Hf_{0.5}NbTa_{0.5}TiZr$, the calculated hkl-specific yield sequence with non-Schmid effect has the sequence from later to earlier of {200}, {310}, {110}, {211}, and {222}. The hkl-specific yield sequence in tension for $HfNb_{0.5}Ta_{0.5}TiZr$ during tension from yielding later to earlier is {200}, {310}, {211}, {110}, and {222}, which follows closer to Schmid's plasticity. For $HfNbTa_{0.5}TiZr$ during tension from yielding later to earlier is {200}, {310}, {211}, followed by {110} and {222} which yield at the same strain level. This yielding sequence of $HfNbTa_{0.5}TiZr$ in tension does not seem to follow either Schmid's plasticity or with non-Schmid effect. Meanwhile, the hkl-specific yield sequence of $Hf_{0.5}NbTa_{0.5}TiZr$ from yielding later to earlier is {200}, {310}, {211}, {110}, and {222}, which follows closer to non-Schmid's effect.

From Figure 28 (a-c), after yielding, the lattice strain of {110} and {220} decreases, plateau, and increased for $HfNb_{0.5}Ta_{0.5}TiZr$, $HfNbTa_{0.5}TiZr$, and $Hf_{0.5}NbTa_{0.5}TiZr$, respectively. The easiest slip system to activate in BCC is the {110} [50]. The increase of lattice strain indicates the increase of elastic strain and the load bearing capacity of the

grain family. This indicates that the load bearing capacity of {110} increased with increasing BCC stability in compression. During tension loading in $Hf_{0.5}NbTa_{0.5}TiZr$, the {200} orientation decreased in lattice strain immediately after hkl-specific yield which is a different lattice strain response compared to the other two materials where their {200} orientation increased after hkl-specific yield and performed load bearing. This response is also different from the {200} orientation response of $Hf_{0.5}NbTa_{0.5}TiZr$ in compression where this orientation performs load bearing. During tension loading, {222} has the lowest lattice strain for all three compositions. This is different from the lowest lattice strain during compression loading, which is the {110}. This different response suggests that more non-Schmid effect contribution is activated during tension. Moreover, the difference in load-bearing response in $Hf_{0.5}NbTa_{0.5}TiZr$ suggests this composition activated a different slip system in tension and performed worse compared to the other composition.

Although the $HfNb_{0.5}Ta_{0.5}TiZr$ is not the strongest in either tension or compression, it is notable that its maximum lattice strain is the highest in both. Meanwhile, both $HfNbTa_{0.5}TiZr$, and $Hf_{0.5}NbTa_{0.5}TiZr$ have the maximum lattice strain levels that somewhat follows the microscopic mechanical behavior. For example, the lattice strains of $Hf_{0.5}NbTa_{0.5}TiZr$ overall are slightly higher than $HfNbTa_{0.5}TiZr$, and $Hf_{0.5}NbTa_{0.5}TiZr$ in compression and the opposite is true in tension, which follows the macroscopic stress strain curve in Figure 26. This trend of maximum lattice strain following the higher macroscopic stress has been reported for many different materials [51, 52]. This indicates that there are other mechanisms that delay plastic relaxation in either loading direction. However, since the macroscopic strength is not increased by this delayed plastic relaxation, the bulk plastic

flow is likely controlled by other softer grain populations or other deformation mechanisms that are not represented by the lattice strain evolution.

Defect evolution

Figure 30 presents the diffraction pattern evolution during tension and compression obtained from loading direction detector for the three compositions. There are no additional peaks emerging during loading, indicating no phase transformation occurring. Some additional peaks were identified as the extensometer blade peak during tension loading for $Hf_{0.5}NbTa_{0.5}TiZr$. The peak broadening evolution is presented in Figures 31 and 32, showing the peak broadening evolution in loading direction (B1), transverse direction (B2), and high angle detector direction (B4). The peak broadening in B2 and B4 were examined in greater detail because their measurement geometry is less sensitive to position-dependent time-of-flight effects so instrumental artifact could be reduced [53]. Figure 31 and 32 both show $HfNb_{0.5}Ta_{0.5}TiZr$ has the highest overall peak broadening increase, then $HfNbTa_{0.5}TiZr$ has the second highest overall peak broadening increase, and $Hf_{0.5}NbTa_{0.5}TiZr$ has the least overall peak broadening increase.

The neutron-diffraction-derived dislocation density is presented in Figure 33. The dislocation density is calculated for three types of dislocations, namely Edge$\langle 111\rangle\{110\}$, Edge$\langle 111\rangle\{211\}$, and Screw$\langle 111\rangle$ dislocations. All types of dislocations from both in situ tension and compression measurement shows $Hf_{0.5}NbTa_{0.5}TiZr$ having the highest dislocation density while $HfNb_{0.5}Ta_{0.5}TiZr$ has the lowest dislocation density among this set of alloys. The dislocation density of $HfNbTa_{0.5}TiZr$ in tension is closer to $Hf_{0.5}NbTa_{0.5}TiZr$, while it is closer to $HfNb_{0.5}Ta_{0.5}TiZr$ in compression. The goodness of

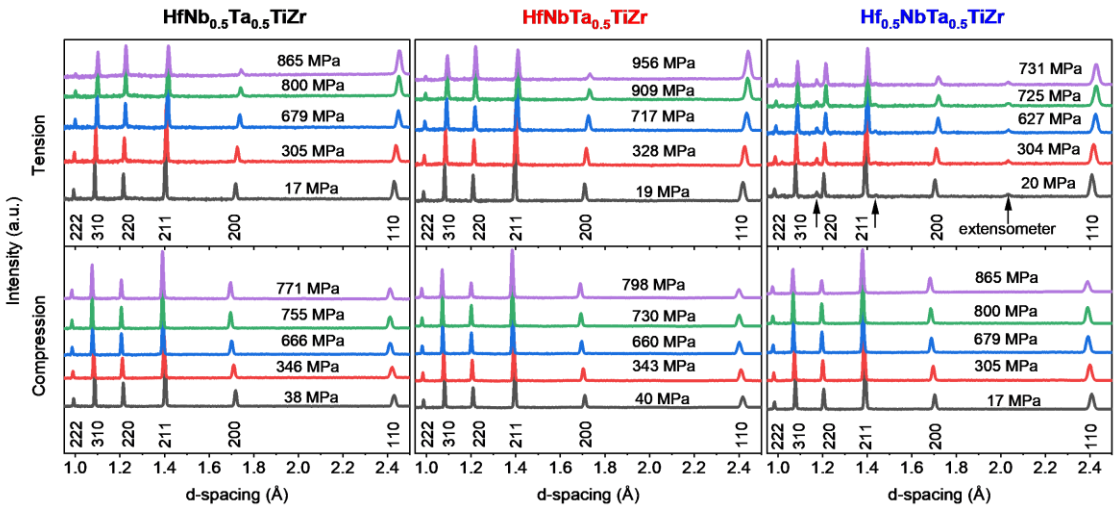


Figure 30. Diffraction patterns evolution of $HfNb_{0.5}Ta_{0.5}TiZr$, $HfNbTa_{0.5}TiZr$, and $Hf_{0.5}NbTa_{0.5}TiZr$ during tension and compression load, obtained from loading direction.

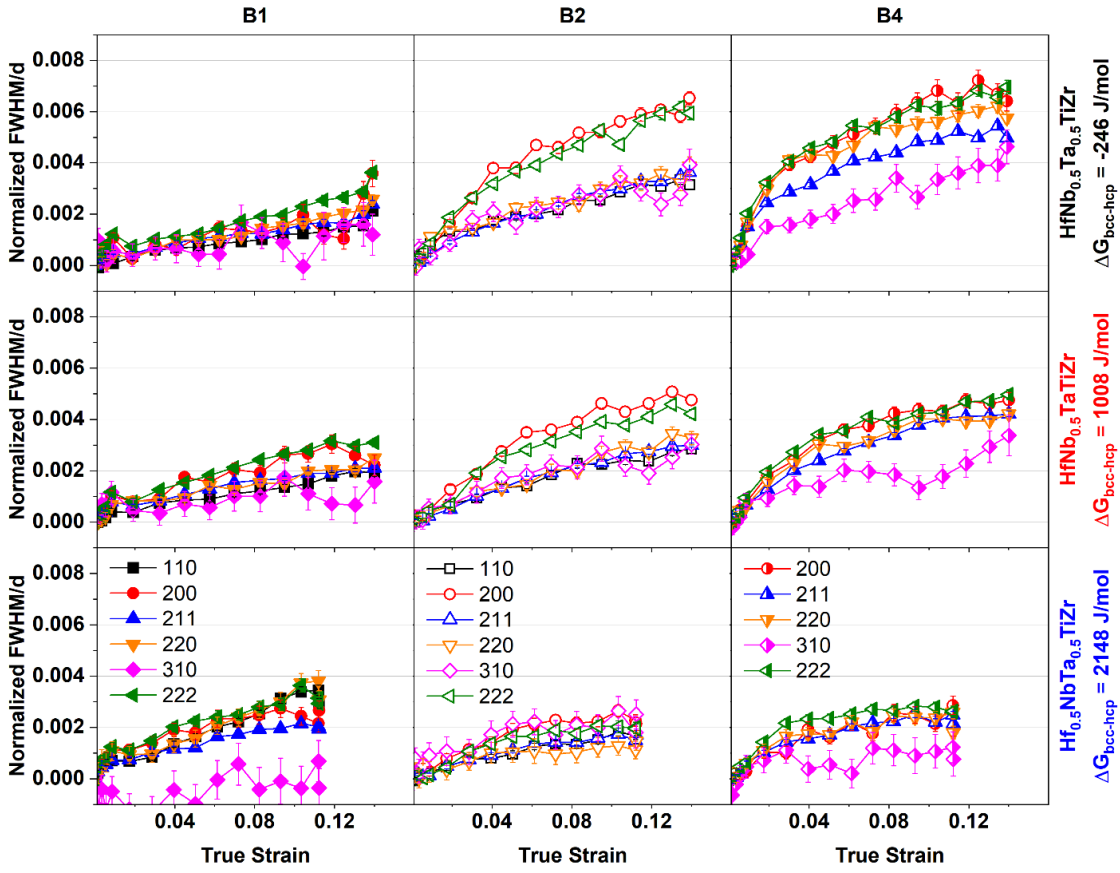


Figure 31. Normalized FWHM/d of $HfNb_{0.5}Ta_{0.5}TiZr$, $HfNbTa_{0.5}TiZr$, and $Hf_{0.5}NbTa_{0.5}TiZr$ during tensile loading

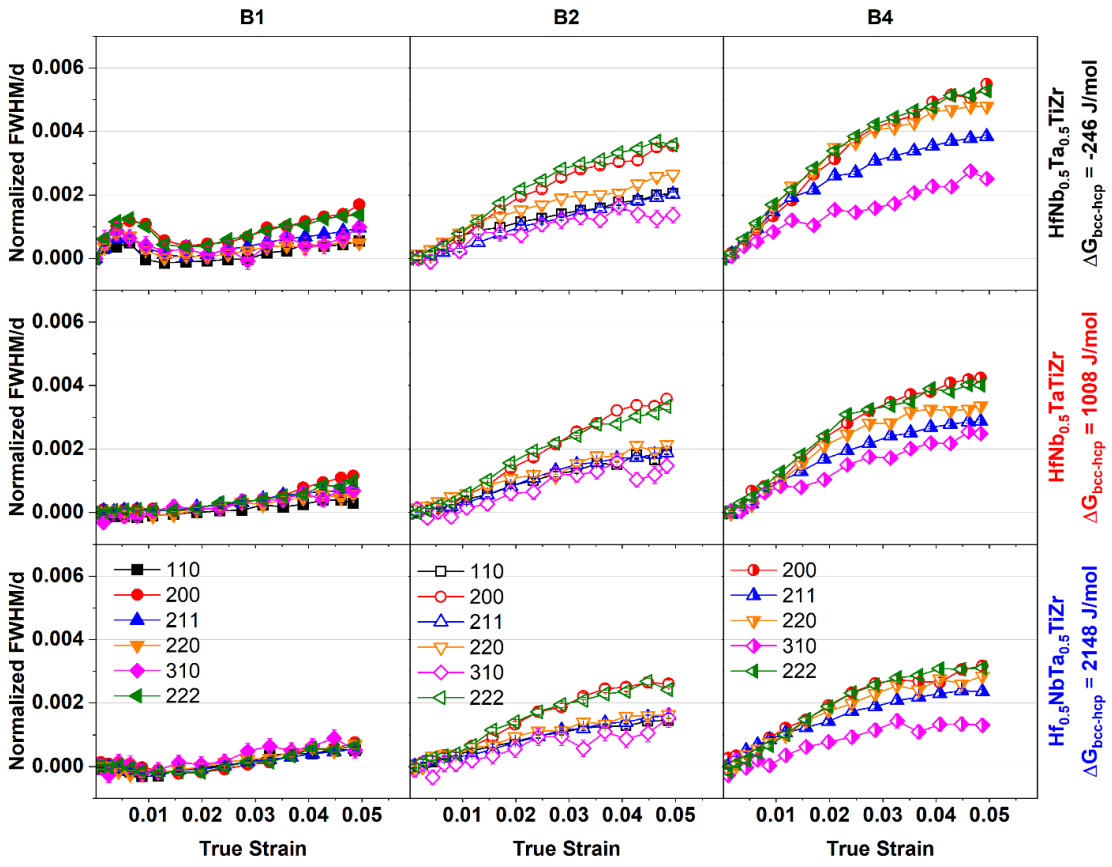


Figure 32. Normalized FWHM/d of $HfNb_{0.5}Ta_{0.5}TiZr$, $HfNbTa_{0.5}TiZr$, and $Hf_{0.5}NbTa_{0.5}TiZr$ during compression loading

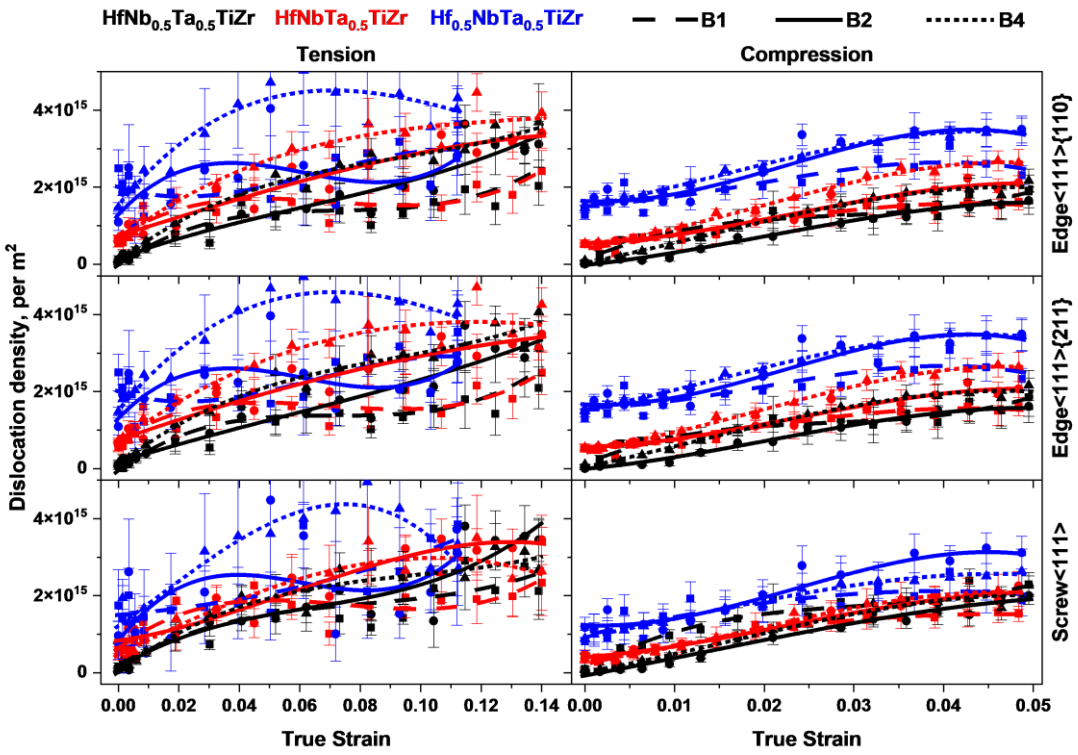


Figure 33. Dislocation density evolution of Edge⟨111⟩{110}-, Edge⟨111⟩{211}-, and Screw ⟨111⟩-type dislocations during in situ tension and compression measurements of $HfNb_{0.5}Ta_{0.5}TiZr$, $HfNbTa_{0.5}TiZr$, and $Hf_{0.5}NbTa_{0.5}TiZr$ extracted from B1, B2, and B4 and calculated using Modified Williamson-Hall model.

fit to obtain the dislocation density is presented in Figure 34. The goodness of fit presents how well the broadening data to the assumed dislocation type model. For $HfNb_{0.5}Ta_{0.5}TiZr$, $HfNbTa_{0.5}TiZr$, and $Hf_{0.5}NbTa_{0.5}TiZr$ screw, mix of screw and edge, and edge dislocation, respectively has a larger goodness of fit. This information does not mean that there are only either type of dislocation in the system, rather the dislocation type with better goodness of fit is more dominant. Nevertheless, this suggests that there is transition of which dislocation types is more dominant during the deformation with increasing BCC phase stability.

The peak broadening increasing with decreasing BCC phase stability and opposite trend observed in dislocation density in both tension and compression suggests that the peak broadening in the alloy with lowest $\Delta G_{BCC-HCP}$ is not dominated by conventional dislocation accumulation. Meanwhile the alloy with the more stable BCC phase, that is with the highest $\Delta G_{BCC-HCP}$ appears to accommodate deformation through conventional dislocation accumulation. The peak broadening appears to act as a broader indicator of deformation-induced lattice heterogeneity while the extracted dislocation density reflects only the portion of broadening that can be associated with dislocation storage within the BCC phase [57, 58]. It is likely that the BCC phase becomes less stable relative to the HCP phase and deformation could be accommodated by phase transformation, twinning, local strain heterogeneity, or intergranular strain partitioning. Mamun et al., [59] studied the tension-compression asymmetry of RHEAs and the influence of lattice distortion and short range ordering with molecular dynamics (MD) and hybrid MD/Monte Carlo simulations. It was found that all the alloy systems that were studied show higher yield stress in compression, lattice distortion strengthened the tension-compression asymmetry, and

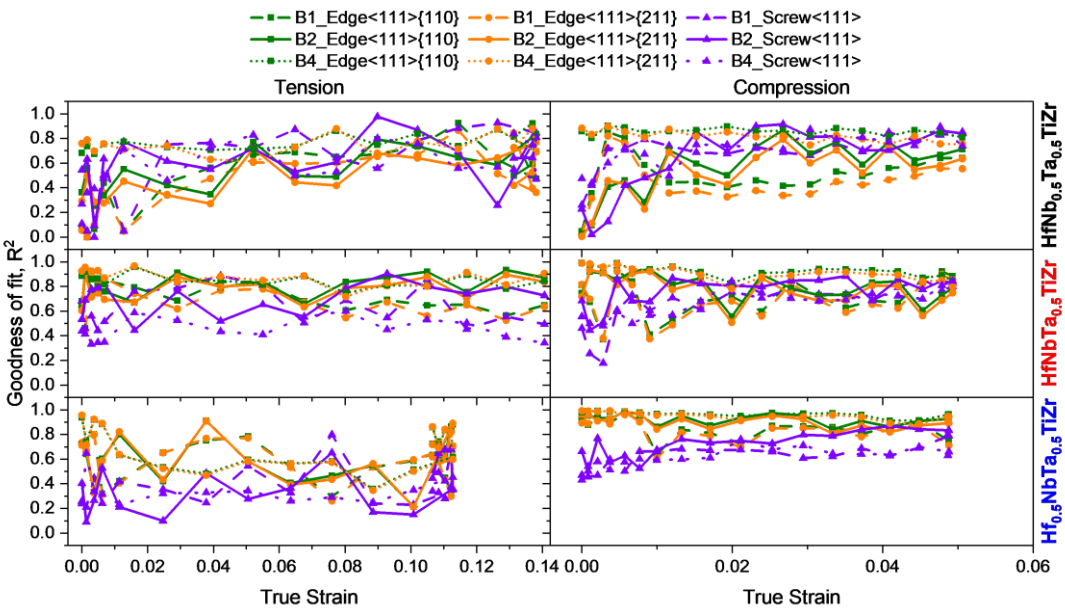


Figure 34. Modified Williamson-Hall plot's goodness of fit

short-range order decreased the tension-compression asymmetry. The short range ordering reduced the tension-compression asymmetry by changing the local atomic environment [59]. The relationship between BCC phase stability and deformation behavior is summarized in Table 6. The composition with lowest BCC phase stability showed minimum tension-compression asymmetry, has the highest work hardening response and peak broadening evolution, but the lowest dislocation density. This discrepancy could be due to deformation induced heterogeneity beyond dislocation density. The dominant dislocation type is screw dislocation. Qualitative comparison with Schmid-only and non-Schmid deformation conditions shows this alloy is closer to the Schmid-only conditions in both tension and compression. Therefore, $HfNb_{0.5}Ta_{0.5}TiZr$ deformed by Schmid's plasticity with formation of deformation induced heterogeneity beyond dislocation density. The composition with the intermediate BCC phase stability shows the reverse tension-compression asymmetry where the yield strength in tension is higher than in compression. The work hardening rate, peak broadening evolution, and dislocation density values fall in between the other two compositions. Dominant dislocation is identified to be a mix of screw and edge dislocations. Neither Schmid nor non-Schmid plasticity fits the hkl-specific yield sequence obtained from in situ neutron diffraction during tension loading. Therefore, it is suggested that other deformation mechanisms are activated during tensile loading such as phase transformation or short range order. Lastly, the system with the highest BCC phase stability shows typical tension-compression asymmetry with minimum work hardening response. The dislocation is dominated with edge dislocation which contradicts the LSR

Table 6. Summary of phase stability, deformation features, and tension–compression asymmetry in Hf–Nb–Ta–Ti–Zr RHEAs

Composition		$HfNb_{0.5}Ta_{0.5}TiZr$	$HfNbTa_{0.5}TiZr$	$Hf_{0.5}NbTa_{0.5}TiZr$
$\Delta G_{BCC-HCP}$ (J/mol)		-246	1008	2148
TCA		T≈C	T>C	C>T
Work hardening response		High	Medium	Low
Normalized FWHM/d		High	Medium	Low
Dislocation density		Low	Medium	High
Dislocation type		Screw	Mix	Edge
Schmid/Non-Schmid Effect	C	Schmid plasticity	Schmid plasticity	Schmid plasticity
	T	Schmid plasticity	Neither	Non-Schmid effect
Suggested deformation behavior		Weak TCA; Schmid plasticity = neutron diffraction	Reverse TCA; not Schmid nor Non-Schmid plasticity ≠ neutron diffraction	Typical TCA; Non-Schmid plasticity = neutron diffraction
Expected Deformation features		Dislocation + small scale phase transformation	Dislocation + small scale phase transformation + local lattice heterogeneity	Dislocation dominated

value, but still within the error of calculation. This alloy system shows a deformation behavior closer to the non-Schmid deformation conditions and is strengthened by edge dislocation strengthening [57].

Conclusions

Hf-Nb-Ta-Ti-Zr RHEAs with varying degrees of BCC phase stability were studied using in situ neutron diffraction measurements to probe the influence of compositional changes on the tension-compression asymmetry and transition between Schmid and non-Schmid deformation behavior. Varying degrees of tension-compression asymmetry were observed from macroscopic mechanical behavior and derived elastic properties. An increased work hardening rate was observed in the RHEA with the least BCC phase stability in the studied alloys in both tension and compression mode, suggesting an extra hardening mechanism might be activated. Peak broadening evolution suggests more lattice heterogeneity is developed in the alloy with less stable BCC phase. Furthermore, dislocation density calculation suggests that the increased peak broadening might not come solely from the accumulated dislocation in the system. Other deformation mechanisms such as phase transformation, twinning, or other heterogeneity might be activated instead. With more BCC phase stability, edge dislocation became the more dominant dislocation type, suggesting edge dislocation strengthening becoming more prevalent. Non-Schmid effect qualitative evaluation shows more non-Schmid effect in the alloy with the more stable BCC phase. The lattice strain evolution shows the tension-compression asymmetry increases with decreasing BCC phase stability, supporting the non-Schmid effect qualitative evaluation. The most severe asymmetry and non-Schmid effect were observed

in the alloy with the most stable BCC phase within the studied alloys, showing a good correlation between BCC phase stability with tension-compression asymmetry and transition from a Schmid to non-Schmid deformation mechanism.

References

1. Senkov, O., J. Scott, S. Senkova, F. Meisenkothen, D. Miracle, and C. Woodward, *Microstructure and elevated temperature properties of a refractory TaNbHfZrTi alloy.* Journal of Materials Science, 2012. **47**(9): p. 4062-4074.
2. Senkov, O.N., G. Wilks, D. Miracle, C. Chuang, and P. Liaw, *Refractory high-entropy alloys.* Intermetallics, 2010. **18**(9): p. 1758-1765.
3. Senkov, O.N., D.B. Miracle, and S.I. Rao, *Correlations to improve room temperature ductility of refractory complex concentrated alloys.* Materials Science and Engineering: A, 2021. **820**: p. 141512.
4. Kumar, P., X. Gou, D.H. Cook, M.I. Payne, N.J. Morrison, W. Wang, M. Zhang, M. Asta, A.M. Minor, R. Cao, Y. Li, and R.O. Ritchie, *Degradation of the mechanical properties of NbMoTaW refractory high-entropy alloy in tension.* Acta Materialia, 2024. **279**: p. 120297.
5. Senkov, O.N., D.B. Miracle, K.J. Chaput, and J.-P. Couzinie, *Development and exploration of refractory high entropy alloys—A review.* Journal of Materials Research, 2018. **33**(19): p. 3092-3128.
6. Dirras, G., L. Lilensten, P. Djemia, M. Laurent-Brocq, D. Tingaud, J.-P. Couzinié, L. Perrière, T. Chauveau, and I. Guillot, *Elastic and plastic properties of as-cast equimolar TiHfZrTaNb high-entropy alloy.* Materials Science and Engineering: A, 2016. **654**: p. 30-38.
7. Chen, H., T. Hanemann, S. Seils, D. Schliephake, A.S. Tirunilai, M. Heilmaier, K.-P. Weiss, and A. Kauffmann, *Influence of Temperature and Plastic Strain on*

Deformation Mechanisms and Kink Band Formation in Homogenized HfNbTaTiZr. Crystals, 2021. **11**(2): p. 81.

8. Senkov, O. and S. Semiatin, *Microstructure and properties of a refractory high-entropy alloy after cold working.* Journal of Alloys and Compounds, 2015. **649**: p. 1110-1123.
9. Okamoto, H., M.E. Schlesinger, and E.M. Mueller, *Alloy phase diagrams*. 2016: Asm International.
10. Zýka, J., J. Málek, J. Veselý, F. Lukáč, J. Čížek, J. Kuriplach, and O. Melikhova, *Microstructure and Room Temperature Mechanical Properties of Different 3 and 4 Element Medium Entropy Alloys from HfNbTaTiZr System.* Entropy, 2019. **21**(2): p. 114.
11. Sheikh, S., S. Shafeie, Q. Hu, J. Ahlström, C. Persson, J. Veselý, J. Zýka, U. Klement, and S. Guo, *Alloy design for intrinsically ductile refractory high-entropy alloys.* Journal of Applied Physics, 2016. **120**(16).
12. Lilensten, L., J.-P. Couzinié, J. Bourgon, L. Perrière, G. Dirras, F. Prima, and I. Guillot, *Design and tensile properties of a bcc Ti-rich high-entropy alloy with transformation-induced plasticity.* Materials Research Letters, 2017. **5**(2): p. 110-116.
13. Carpenter, W.J., Y. Yang, B. Gludovatz, W.A. Curtin, and E.P. George, *Effects of HCP/BCC element ratios on the room-temperature tensile properties of Ti-Zr-Hf-Nb-Ta refractory high-entropy alloys.* Intermetallics, 2025. **185**: p. 108923.

14. Anderson, P.M., J.P. Hirth, and J. Lothe, *Theory of dislocations*. 2017: Cambridge University Press.

15. Duesbery, M., V. Vitek, and D.K. Bowen, *The effect of shear stress on the screw dislocation core structure in body-centred cubic lattices.* Proceedings of the Royal Society of London. A. Mathematical and Physical Sciences, 1973. **332**(1588): p. 85-111.

16. Yang, L.H., P. Söderlind, and J.A. Moriarty, *Accurate atomistic simulation of (a/2)〈111〉 screw dislocations and other defects in bcc tantalum.* Philosophical Magazine A, 2001. **81**(5): p. 1355-1385.

17. Wang, Z. and I. Beyerlein, *An atomistically-informed dislocation dynamics model for the plastic anisotropy and tension–compression asymmetry of BCC metals.* International Journal of Plasticity, 2011. **27**(10): p. 1471-1484.

18. Kraych, A., E. Clouet, L. Dezerald, L. Ventelon, F. Willaime, and D. Rodney, *Non-glide effects and dislocation core fields in BCC metals.* npj Computational Materials, 2019. **5**(1): p. 109.

19. Pan, Y., T. Fu, M. Duan, C. Li, H. Hu, and X. Peng, *Tension–Compression Asymmetry of BCC NbMoTaW in High Entropy Alloy Nanowires.* ACS Applied Nano Materials, 2024. **7**(7): p. 8121-8129.

20. Bai, Y., K. Zhang, T. Chen, Z. Liu, Y. Wang, and B. Wei, *Alterable tension-compression asymmetry in work hardening of an additively manufactured dual-phase high-entropy alloy.* International Journal of Plasticity, 2022. **158**: p. 103432.

21. Huang, H., Y. Wu, J. He, H. Wang, X. Liu, K. An, W. Wu, and Z. Lu, *Phase-transformation ductilization of brittle high-entropy alloys via metastability engineering.* Advanced Materials, 2017. **29**(30): p. 1701678.

22. Tsuru, T., S. Han, S. Matsuura, Z. Chen, K. Kishida, I. Iobzenko, S.I. Rao, C. Woodward, E.P. George, and H. Inui, *Intrinsic factors responsible for brittle versus ductile nature of refractory high-entropy alloys.* Nature Communications, 2024. **15**(1): p. 1706.

23. Huang, S., W. Li, E. Holmström, and L. Vitos, *Phase-transition assisted mechanical behavior of TiZrHfTa x high-entropy alloys.* Scientific Reports, 2018. **8**(1): p. 12576.

24. An, K., Y. Chen, and A.D. Stoica, *VULCAN: A "hammer" for high-temperature materials research.* Mrs Bulletin, 2019. **44**(11): p. 878-885.

25. An, K., H.D. Skorpenske, A.D. Stoica, D. Ma, X.-L. Wang, and E. Cakmak, *First in situ lattice strains measurements under load at VULCAN.* Metallurgical and Materials Transactions A, 2011. **42**: p. 95-99.

26. Xu, S., W.-R. Jian, and I.J. Beyerlein, *Ideal simple shear strengths of two HfNbTaTi-based quinary refractory multi-principal element alloys.* APL Materials, 2022. **10**(11).

27. Thompson, A.P., H.M. Aktulga, R. Berger, D.S. Bolintineanu, W.M. Brown, P.S. Crozier, P.J. in 't Veld, A. Kohlmeyer, S.G. Moore, T.D. Nguyen, R. Shan, M.J. Stevens, J. Tranchida, C. Trott, and S.J. Plimpton, *LAMMPS - a flexible simulation*

tool for particle-based materials modeling at the atomic, meso, and continuum scales. Computer Physics Communications, 2022. **271**: p. 108171.

28. Hirel, P., *Atomsk: A tool for manipulating and converting atomic data files.* Computer Physics Communications, 2015. **197**: p. 212-219.
29. Stukowski, A., *Visualization and analysis of atomistic simulation data with OVITO–the Open Visualization Tool.* Modelling and Simulation in Materials Science and Engineering, 2010. **18**(1): p. 015012.
30. Li, L., Z. Chen, S. Hu, D. Zhu, L. Li, W. Yang, H. Quan, and D. Liu, *Synergistic regulation of the TRIP effect and phase stability on the microstructural evolution and mechanical behavior of metastable TiZrHfNb alloys.* Journal of Alloys and Compounds, 2026. **1057**: p. 186669.
31. Huang, H., Y. Sun, P. Cao, Y. Wu, X. Liu, S. Jiang, H. Wang, and Z. Lu, *On cooling rates dependence of microstructure and mechanical properties of refractory high-entropy alloys HfTaTiZr and HfNbTiZr.* Scripta Materialia, 2022. **211**: p. 114506.
32. Nguyen, V.T., M. Qian, Z. Shi, T. Song, L. Huang, and J. Zou, *Compositional design of strong and ductile (tensile) Ti-Zr-Nb-Ta medium entropy alloys (MEAs) using the atomic mismatch approach.* Materials Science and Engineering: A, 2019. **742**: p. 762-772.
33. Jung, Y., K. Lee, S.J. Hong, J.K. Lee, J. Han, K.B. Kim, P.K. Liaw, C. Lee, and G. Song, *Investigation of phase-transformation path in TiZrHf(VNbTa)x refractory high-entropy alloys and its effect on mechanical property.* Journal of Alloys and Compounds, 2021. **886**: p. 161187.

34. Abdel-Hady, M., K. Hinoshita, and M. Morinaga, *General approach to phase stability and elastic properties of β-type Ti-alloys using electronic parameters.* Scripta Materialia, 2006. **55**(5): p. 477-480.

35. Wei, S., S.J. Kim, J. Kang, Y. Zhang, Y. Zhang, T. Furuhara, E.S. Park, and C.C. Tasan, *Natural-mixing guided design of refractory high-entropy alloys with as-cast tensile ductility.* Nature Materials, 2020. **19**(11): p. 1175-1181.

36. Considère, M., *Mémoire sur l'emploi du fer et de l'acier dans les constructions.* (No Title), 1885.

37. Havner, K.S., *On the onset of necking in the tensile test.* International Journal of Plasticity, 2004. **20**(4): p. 965-978.

38. Hill, R., *The elastic behaviour of a crystalline aggregate.* Proceedings of the Physical Society. Section A, 1952. **65**(5): p. 349-354.

39. Pugh, S., *XCII. Relations between the elastic moduli and the plastic properties of polycrystalline pure metals.* The London, Edinburgh, and Dublin Philosophical Magazine and Journal of Science, 1954. **45**(367): p. 823-843.

40. Nye, J.F., *Physical properties of crystals: their representation by tensors and matrices*. 1985: Oxford university press.

41. Pettifor, D.G. and M. Aoki, *Bonding and structure of intermetallics: a new bond order potential.* Philosophical Transactions of the Royal Society of London. Series A: Physical and Engineering Sciences, 1991. **334**(1635): p. 439-449.

42. Gnäupel-Herold, T., A.A. Creuziger, and M. Iadicola, *A model for calculating diffraction elastic constants.* Applied Crystallography, 2012. **45**(2): p. 197-206.

43. Wu, Z., X.-J. Chen, V.V. Struzhkin, and R.E. Cohen, *Trends in elasticity and electronic structure of transition-metal nitrides and carbides from first principles.* Physical Review B, 2005. **71**(21): p. 214103.

44. Zhou, X., C. Ha, S. Yi, J. Bohlen, N. Schell, Y. Chi, M. Zheng, and H.-G. Brokmeier, *Texture and Lattice Strain Evolution during Tensile Loading of Mg–Zn Alloys Measured by Synchrotron Diffraction.* Metals, 2020. **10**(1): p. 124.

45. Clausen, B., T. Lorentzen, M.A. Bourke, and M.R. Daymond, *Lattice strain evolution during uniaxial tensile loading of stainless steel.* Materials Science and Engineering: A, 1999. **259**(1): p. 17-24.

46. Daymond, M.R., C.N. Tomé, and M.A.M. Bourke, *Measured and predicted intergranular strains in textured austenitic steel.* Acta Materialia, 2000. **48**(2): p. 553-564.

47. Lee, C., G. Kim, Y. Chou, B.L. Musicó, M.C. Gao, K. An, G. Song, Y.-C. Chou, V. Keppens, W. Chen, and P.K. Liaw, *Temperature dependence of elastic and plastic deformation behavior of a refractory high-entropy alloy.* Science Advances. **6**(37): p. eaaz4748.

48. Tschopp, M., D. Spearot, and D. McDowell, *Atomistic simulations of homogeneous dislocation nucleation in single crystal copper.* Modelling and Simulation in Materials Science and Engineering, 2007. **15**(7): p. 693-709.

49. Knezevic, M., I.J. Beyerlein, M.L. Lovato, C.N. Tomé, A.W. Richards, and R.J. McCabe, *A strain-rate and temperature dependent constitutive model for BCC*

metals incorporating non-Schmid effects: Application to tantalum–tungsten alloys. International Journal of Plasticity, 2014. **62**: p. 93-104.

50. Huang, S., D.W. Brown, B. Clausen, Z. Teng, Y. Gao, and P.K. Liaw, *In Situ Neutron-Diffraction Studies on the Creep Behavior of a Ferritic Superalloy.* Metallurgical and Materials Transactions A, 2012. **43**(5): p. 1497-1508.

51. Brown, D.W., D.P. Adams, L. Balogh, J.S. Carpenter, B. Clausen, G. King, B. Reedlunn, T.A. Palmer, M.C. Maguire, and S.C. Vogel, *In Situ Neutron Diffraction Study of the Influence of Microstructure on the Mechanical Response of Additively Manufactured 304L Stainless Steel.* Metallurgical and Materials Transactions A, 2017. **48**(12): p. 6055-6069.

52. Jeong, J.S., W. Woo, K.H. Oh, S.K. Kwon, and Y.M. Koo, *In situ neutron diffraction study of the microstructure and tensile deformation behavior in Al-added high manganese austenitic steels.* Acta Materialia, 2012. **60**(5): p. 2290-2299.

53. Chen, Y., D. Yu, and K. An, *Position-Dependent Neutron Time-of-Flight Deviation at VULCAN Diffractometer*. 2025, Oak Ridge National Laboratory (ORNL), Oak Ridge, TN (United States).

54. Ribárik, G., B. Jóni, and T. Ungár, *Global optimum of microstructure parameters in the CMWP line-profile-analysis method by combining Marquardt-Levenberg and Monte-Carlo procedures.* Journal of Materials Science & Technology, 2019. **35**(7): p. 1508-1514.

55. Simm, T.H., *Peak broadening anisotropy and the contrast factor in metal alloys.* Crystals, 2018. **8**(5): p. 212.

56. Mamun, A.A., X.-G. Li, S. Xu, and Y. Su, *Anisotropic Deformation in Refractory Multi-principal Element Alloys: Insights from Atomistic Simulations and Machine Learning.* High Entropy Alloys & Materials, 2025. **3**(1): p. 153-164.

57. Lee, C., F. Maresca, R. Feng, Y. Chou, T. Ungar, M. Widom, K. An, J.D. Poplawsky, Y.-C. Chou, and P.K. Liaw, *Strength can be controlled by edge dislocations in refractory high-entropy alloys.* Nature communications, 2021. **12**(1): p. 5474.

CHAPTER V

SUMMARY AND FUTURE SUGGESTIONS

Summary

The summary of the overall work is as follows:

1. Tangent modulus method to quantify real-time hardening mechanisms in nanoprecipitation-strengthened $(FeCoNi)_{86}Al_7Ti_7$ has successfully been developed from in situ neutron diffraction, where successive hardening mechanism was revealed.
2. Little compositional change led to a plethora of microstructural and mechanistic change was observed with in situ neutron diffraction while microscopic stress-strain behavior was not changed drastically.
3. Tension compression asymmetry was probed using lattice strain analysis and Non-Schmid effect contribution.

Future Suggestions

Suggestions for future work based on this work are as follows:

1. Integration of deformation mechanisms, advanced characterization, and neutron diffraction points out the missing link (e.g., what is needed to study reverse-TCA in RHEAs).
2. CMWP analysis to obtain more definitive dislocation characters from the diffraction pattern.
3. "Tangent modulus approach" has the potential of becoming an engineering toolbox (capturing the depth while avoiding unnecessary simulation work) for many other projects

VITA

Lia Amalia was born in Samarinda, Indonesia. She moved to Surabaya, Indonesia to obtain an undergraduate degree in Mechanical Engineering at Institut Teknologi Sepuluh Nopember. She moved to Hsinchu Taiwan to continue her master's degree in Materials Science and Engineering. She was advised by Peter K. Liaw and Yanfei Gao during her Ph. D studies and mentored by Ke An on in situ neutron diffraction techniques during her internship at Oak Ridge National Laboratory.